UC San Diego
UC San Diego Electronic Theses and Dissertations

Title

Subantarctic Mode Water formation : air-sea fluxes and cross-frontal exchange

Permalink

Author

Holte, James

Publication Date

2010

Peer reviewed|Thesis/dissertation

UNIVERSITY OF CALIFORNIA, SAN DIEGO

Subantarctic Mode Water formation: air-sea fluxes and cross-frontal exchange

A dissertation submitted in partial satisfaction of the
requirements for the degree
Doctor of Philosophy

in

Oceanography

by

James Holte

Committee in charge:

        Lynne Talley, Chair
        Teresa Chereskin
        Sarah Gille
        Dean Roemmich
        Sutanu Sarkar

2010

The dissertation of James Holte is approved, and it is acceptable in quality and form for publication on microfilm and electronically:

_____

_____

_____

_____

_____
Chair

University of California, San Diego

2010

DEDICATION

To my family.

TABLE OF CONTENTS

LIST OF FIGURES

LIST OF TABLES

ACKNOWLEDGEMENTS

This dissertation would not have come to fruition without the support and guidance of many people. Lynne Talley provided valuable perspective on research, let me explore an immense data set, and fortuitously took a sabbatical to WHOI at the same time that I moved to Boston. The freedom to follow my own research interests, while at times a slow process, greatly contributed to my development as a scientist. Lynne was an excellent mentor, with whom I enjoyed catching up on news of the twins as much as talking about science. My committee members Teresa Chereskin, Sarah Gille, Dean Roemmich, and Sutanu Sarkar, as well as Bernadette Sloyan, helped me hone my wide-ranging qualifying proposal into a manageable thesis.

I cannot express enough thanks to my family, Meka, Kathy, Hal, and Dave. Their love and support were a great help in graduate school, as in all things.

I found a great group of colleagues when I started at Scripps. D-rock Mansbach, Marissa Yates, Aurelien Ponte, Ashley Van Beusekom, and Dave Clark will always be good friends, as will Chinarita and Cheff, with whom I shared many excellent travels. Thanks also to the many amiable students who shared time with me at Scripps, quite a few over 7+ years, and always made lunch so enjoyable.

I also owe thanks to a wide-ranging group of people who made graduate school much simpler than it would have been otherwise. Thanks to Tomomi Ushii for keeping my hall such a cheery place, among her many other duties. Thanks to Phil Moses for keeping my computer running in tip-top shape. Thanks also to Sharon Escher for cleaning up my MATLAB code on occasion. Thanks to Aurelien, Dian Putrasahan, and Caroline Papadopoulos for helping me get started with ROMS, and even teaching me to run it in parallel. I thoroughly enjoyed my classwork six long years ago, a testament to the many excellent professors at Scripps. It was also a pleasure working with scientists from SIO's Ocean Data Facility and the crew of the R/V Knorr on my two cruises.

Chapter 2 in its entirety is a reprint with no modifications to content of the article "A New Algorithm for Finding Mixed Layer Depths with Applications to Argo Data and Subantarctic Mode Water Formation" that appeared in Journal of Atmospheric and Oceanic Technology, 2009, 26, 1920-1939 (Copyright of the American Meteorological Society 2009). The dissertation author was the first author and primary researcher of this material, with contributions from the second author, Lynne Talley.

Chapter 3, in full, is a reprint with minor modifications of the article "The role of

air-sea fluxes in Subantarctic Mode Water formation," to be submitted for publication. The dissertation author was the first author and primary researcher of this material, with contributions from co-authors Lynne Talley, Teresa Chereskin, and Bernadette Sloyan.

Chapter 4, in full, is a reprint with minor modifications of the article "Optimum multiparameter analysis of cross-frontal exchange at the Subantarctic Front," to be submitted for publication. The dissertation author was the first author and primary researcher of this material, with contributions from co-authors Lynne Talley, Teresa Chereskin, and Bernadette Sloyan.

VITA

2003	A.B. in Mathematics and Physics, Bowdoin College
2010	Ph.D. in Oceanography, Scripps Institution of Oceanography, University of California, San Diego

PUBLICATIONS

Holte, J. and L. Talley, "A New Method for Finding Mixed Layer Depths with Applications to Subantarctic Mode Water and Argo," *Journal of Atmospheric and Oceanic Technology*, 26 (9), 1920-1939, 2009.

Sloyan, B., L. Talley, T. Chereskin, R. Fine, and J. Holte, "Antarctic Intermediate Water and Subantarctic Mode Water Formation in the Southeast Pacific: the Role of Turbulent Mixing," *Journal of Physical Oceanography*, 40, 1558-1574, 2010.

Holte, J., L. Talley, T. Chereskin, and B. Sloyan, "The role of air-sea fluxes in Subantarctic Mode Water formation," in preparation.

Holte, J., L. Talley, T. Chereskin, and B. Sloyan, "Optimum multiparameter analysis of cross-frontal exchange at the Subantarctic Front," in preparation.

Holte, J., J. Gilson, L. Talley, and D. Roemmich, "An Argo mixed layer depth climatology," in preparation.

ABSTRACT OF THE DISSERTATION

Subantarctic Mode Water formation: air-sea fluxes and cross-frontal exchange

by

James Holte

Doctor of Philosophy in Oceanography

University of California, San Diego, 2010

Lynne Talley, Chair

This dissertation focuses on Subantarctic Mode Water (SAMW) formation.

A new hybrid method for finding the mixed layer depth (MLD) is developed that models the general shape of each profile, searches for physical features in the profile, and calculates threshold and gradient MLDs to assemble a suite of possible MLD values. It then analyzes the patterns in the suite to select a final MLD estimate. The algorithm is applied to Argo profiles from the southeast Pacific Ocean, a SAMW formation region. In general, threshold methods find deeper MLDs than the new algorithm and gradient methods produce more anomalous MLDs than the new algorithm. The deepest MLDs in the region typically occur in August and September, routinely reach 500 m, and are found immediately north of the mean Subantarctic Front (SAF).

Two hydrographic surveys in the southeast Pacific Ocean and a one-dimensional mixed layer model are used to assess the role of air-sea fluxes in forming the deep SAMW mixed layers. The simulated winter mixed layers generated by five forcing products resemble Argo observations of SAMW. Mixing driven by buoyancy loss and wind forcing is strong enough to deepen the SAMW layers. Wind-driven mixing is central to SAMW formation, as model runs forced with buoyancy forcing alone produce very shallow mixed layers. Air-sea fluxes indirectly influence winter SAMW properties by controlling how deeply the profiles mix. The stratification and heat content of the initial profiles are important in determining the properties of the SAMW and the likelihood of deep mixing.

An optimum multiparameter (OMP) analysis is used to estimate the cumulative effect of the cross-frontal exchange, revealing an along-front increase in Polar Frontal Zone (PFZ) water fractional content in the region north of the SAF between the 27.0 and 27.3 kg m^{-3} isopycnals. The fractional content of PFZ water north of the SAF increases by approximately 0.1 for every 15° of longitude in the southeast Pacific. A simple bulk calculation reveals that this magnitude of cross-frontal exchange could cause the downstream evolution of SAMW mixed layer properties.

Chapter 1

Introduction

Typical ocean observations reveal a well-mixed surface layer in which temperature, salinity, and density are nearly vertically uniform. This mixed layer is a highly temporally and spatially variable feature in the surface ocean, yet it contributes to the large-scale ocean circulation and structure. Wind forcing acts through the mixed layer to drive ocean circulation. In areas where deep convection occurs, winter mixed layer conditions set the properties of the deep and intermediate water masses of the ocean's interior.

The deepest mixed layers in the Southern Ocean form north of the Subantarctic Front (SAF), the northernmost front of the Antarctic Circumpolar Current (ACC). McCartney (1977) labeled these deep winter mixed layers Subantarctic Mode Water (SAMW). SAMW forms along large portions of the ACC path, becoming progressively colder, fresher, and denser as it nears Drake Passage from the west (McCartney, 1977; England et al., 1993; Talley, 1996; Hanawa and Talley, 2001).

SAMW is important to many global-scale processes. It forms part of the upper limb of the global overturning circulation (Sloyan and Rintoul, 2001), renewing the lower thermocline in the southern hemisphere's subtropical gyres (McCartney, 1982). The heat, freshwater, and carbon transports associated with SAMW's global-scale circulation make it relevant to the Earth's climate and to the ocean's global overturning circulation (Keeling and Stephens, 2001; Pahnke and Zahn, 2005).

This thesis examines SAMW formation in the southeast Pacific Ocean, a formation site of some of the deepest and the densest SAMW mixed layers. The second chapter details the development of a new algorithm for finding the mixed layer depth (MLD) of

Argo profiles and its application to profiles from the southeast Pacific Ocean. In 2005 and 2006, two research cruises in the southeast Pacific Ocean set out to study SAMW and Antarctic Intermediate Water formation. Many processes contribute to SAMW formation, including: gyre inflow; cross-frontal advection in the form of Ekman transport, eddies, and intrusions; heat and freshwater fluxes at the air-sea interface and at the base of the mixed layer; and mixing. The third and fourth chapters use data from the two cruises to assess the role of air-sea fluxes and cross-frontal exchange in forming the deep SAMW mixed layers observed north of the SAF.

SAMW formation is difficult to observe; it occurs in geographically remote areas under stormy, winter conditions, making it ideal for observation by Argo. Chapter 2, as a prelude to the two cruises, details the development of a new algorithm for finding the MLD and its application to Argo profiles from the southeast Pacific Ocean. The new algorithm avoids many of the pitfalls of threshold and gradient methods, which are limited by their dependence on the surface reference value and the chosen threshold value. Threshold methods, especially those based solely on temperature, inherently overestimate the MLD. This is particularly true for winter profiles, where the mixed layer gradually blends into the deeper waters. Lukas and Lindstrom (1991) found that a density criterion is more reliable for finding the MLD than a temperature criterion, yet there is an order of magnitude fewer density profiles than temperature profiles (Lorbacher et al., 2006). Threshold methods using density falter in density compensating layers, and those using temperature falter in the presence of salinity barrier layers (Lukas and Lindstrom, 1991; Sprintall and Tomczak, 1992). These traits motivated the development of the new algorithm, which was designed to reliably identify MLDs with only temperature profiles. The algorithm models the general shape of each profile, searches for physical features in the profile, and calculates threshold and gradient MLDs to assemble a suite of possible MLD values. It then analyzes the patterns in the suite to select a final MLD estimate. The algorithm MLDs are extensively compared to threshold MLDs calculated using de Boyer Montégut et al. (2004)'s criteria, and to gradient method MLDs. The algorithm is then used to examine SAMW formation, providing the location, time of year, and temperature, salinity, and density characteristics of this oceanic process that has historically proven difficult to observe.

SAMW differs from other mode waters in that it lacks a neighboring continental land mass to power large heat fluxes; Subtropical Mode Water, which forms near the

Gulf Stream in the Atlantic Ocean, experiences winter heat fluxes in excess of -1000 W m^{-2} (Joyce et al., 2009). The largest fluxes observed during our 2005 austral winter cruise reached -200 W m^{-2}. Many recent studies have found that air-sea fluxes cannot account for the observed temporal variability of SAMW (Speer et al., 2000; Sloyan and Rintoul, 2001). Others have shown that turbulent mixing driven by buoyancy loss (Wang and Matear, 2001) and wind forcing (Sloyan et al., 2010) are important to the formation of deep SAMW mixed layers. Chapter 3 seeks to clarify the importance of air-sea fluxes to SAMW formation using observations from two cruises in the Southeast Pacific Ocean. It first characterizes the SAMW mixed layers and their proximity to the SAF. It then focuses on the relationship between the deep SAMW mixed layers and the air-sea fluxes. Cruise meteorological measurements are used to calculate latent and sensible heat fluxes with the COARE algorithm and to explore the meteorological conditions that produced the deep SAMW mixed layers. The fluxes from both cruises are used to evaluate a number of heat flux products, including NCEP, ECMWF, OAFlux, and Ofuro. The multitude of heat flux products, along with precipitation, are used to evolve profiles from the 2006 austral summer cruise in a one-dimensional KPP mixed layer model. We neglect any advective mechanisms, and focus on how air-sea forcing, initial profile stratification, and mixing determine the SAMW mixed layers' depths, properties, area extent, relationship to the SAF, and downstream variation.

Chapter 4 examines the importance of cross-frontal exchange to SAMW formation. It addresses whether the ACC acts as "barrier or blender," that is, whether the ACC limits lateral exchange or drives increased mixing. This question was first addressed for the Gulf Stream by Bower et al. (1985), and later for the Agulhas by Beal et al. (2006). Studies of the ACC have shown that eddies are likely to be significant in maintaining local heat budgets in the SAMW formation region north of the SAF, and so influence SAMW property variability (Ansorge et al., 2006; Sallée et al., 2008; Herraiz-Borreguero and Rintoul, 2010). Others have demonstrated that Ekman transport dominates the temporal variability of SAMW properties (Speer et al., 2000; Sloyan and Rintoul, 2001; Rintoul and England, 2002a). In this chapter, cross-frontal exchange is considered as a possible mechanism for the along-front freshening and cooling of profiles north of the SAF between the 27.0 and 27.3 kg m^{-3} isopycnals. This isopycnal range is generally below the mixed layer, and so is not locally forced by air-sea fluxes or wind-driven mixing. Profiles from the two cruises are examined for evidence of cross-frontal exchange,

yielding numerous eddies and intrusions. An optimum multiparameter (OMP) analysis is used to estimate the cumulative cross-frontal exchange. A simple bulk calculation reveals that the cross-frontal exchange diagnosed by the OMP analysis is consistent with the downstream evolution of SAMW mixed layer properties.

Chapter 2

A new method for finding mixed layer depths with applications to Argo and Subantarctic Mode Water formation

2.1 Introduction

The surface layer of the ocean records past winter mixing events, the subsequent onset of spring re-stratification, as well as the traces of all physical processes occurring above the ocean's permanent thermocline. Typical ocean observations reveal a well-mixed layer, in which temperature, salinity, and density are nearly vertically uniform, embedded in the surface layer. Turbulent mixing processes powered by wind stress and heat exchange at the air-sea interface create this neutrally buoyant and thoroughly mixed column in the upper ocean. This turbulently mixed layer is highly variable. In the summer, mixed layer depths can reach tens of meters or even be absent. In the winter, deep convection driven by surface heat loss can mix the water column to two thousand meters in select locations (Marshall and Schott, 1999). Coupled with the intense seasonal and spatial variation of the mixed layer is a complexity of structures in the ocean surface layer that can often obscure the depth of the turbulently mixed layer (Sprintall and Roemmich, 1999; Dong et al., 2008).

The mixed layer is important to a variety of ocean processes. The mixed layer

responds to atmospheric fluxes and transmits those fluxes to the ocean interior. Wind forcing acts through the mixed layer to drive ocean circulation (Chereskin and Roemmich, 1991). The depth of the mixed layer establishes the volume of water over which the surface heat flux is distributed (Chen et al., 1994; Ohlmann et al., 1996). In areas where deep convection occurs, winter mixed layer conditions set the properties of the deep and intermediate water masses of the ocean's interior (Talley, 1999).

Widespread interest in the processes at work in the mixed layer has spawned numerous arbitrary definitions of the mixed layer as well as a corresponding number of schemes for finding its depth. Due to the paucity of ocean turbulence and mixing measurements, these schemes use temperature and density profiles to find the mixed layer. In these schemes and in this paper, mixed layer depth (MLD) refers to the depth of the uniform surface layer that is assumed to owe its homogeneity to turbulent mixing.

The most widely favored and simplest scheme for finding the MLD is the threshold method. Threshold methods search for the depth at which the temperature or density profiles change by a predefined amount relative to a surface reference value. Kara et al. (2000) and de Boyer Montégut et al. (2004) examined various threshold criteria used in the literature and determined their own optimal global threshold definitions of the MLD. In deciding upon their own criteria, de Boyer Montégut et al. (2004) determined that the larger threshold values commonly used with averaged profiles, such as the 0.5°C threshold value used by Monterey and Levitus (1997) and the 0.8°C used by Kara et al. (2000), overestimated the MLD of individual profiles. Likewise, smaller critera of 0.1°C underestimated the MLD. After examining numerous profiles, de Boyer Montégut et al. (2004) concluded that 0.2°C was the optimal temperature threshold. They similarly determined an optimal density threshold value of 0.03 kg m^{-3}. To avoid diurnal heating in the surface layer, de Boyer Montégut et al. (2004) chose a surface reference level of 10 m. These values were recently employed by Oka et al. (2006) in examining the seasonality of the MLD in the North Pacific and by Dong et al. (2008) in examining the mixed layer of the entire Southern Ocean.

Gradient methods, which are also widely used, work much like threshold methods; they assume that there is a strong gradient at the base of the mixed layer and therefore search for critical gradient values (Lukas and Lindstrom, 1991). Commonly used values range from 0.0005 to 0.05 kg m^{-4} for density gradients and 0.025°C m^{-1} for temperature gradients (Dong et al., 2008).

Threshold and gradient methods are limited by their dependence on the surface reference value and the chosen threshold value; it is difficult to decide on a single threshold value or gradient criterion for all ocean profiles. Threshold methods, especially those based solely on temperature, inherently overestimate the MLD. Threshold methods using density falter in density compensating layers, and those using temperature falter in the presence of salinity barrier layers (Lukas and Lindstrom, 1991; Sprintall and Tomczak, 1992). Lukas and Lindstrom (1991) found that a density criterion is more reliable for finding the MLD than a temperature criterion, yet there is an order of magnitude fewer density profiles than temperature profiles (Lorbacher et al., 2006).

A variety of more complex methods for finding the MLD have been developed. The "curvature method," proposed by Lorbacher et al. (2006), uses conditions for the second derivative and the gradient to identify the MLD. Thomson and Fine (2003) introduced the "split and merge" method, which fits a variable number of linear segments to a profile. They found that their method performed similar to threshold methods. Chu et al. (1999) created a geometric model to determine the MLD of Arctic profiles. Lavender et al. (2002) used the intersection between a straight line fit to the upper layer and an exponential plus second-order polynomial fit to the deep layer to estimate the MLD of individual temperature profiles in the Labrador Sea. This method apparently worked in the North Atlantic, but efforts to implement the method in the Southern Ocean did not produce realistic MLDs.

This paper introduces a new algorithm for finding the MLD of individual profiles. The algorithm builds on traditional threshold and gradient methods by tying its estimate of the MLD to physical features in the profile. It accomplishes this by first modeling the profile's general shape; it approximates the seasonal thermocline and the mixed layer with best-fit lines. It then assembles a suite of possible MLD values by calculating the threshold and gradient methods' MLDs, identifying the intersection of the thermocline and mixed layer fits, locating profile maxima or minima, and searching for intrusions at the base of the mixed layer. Finally, it looks for groupings and patterns within the possible MLDs to select the final MLD for each profile. Section 3 details how the algorithm calculates the possible MLDs and selects the final MLD estimate. The algorithm's selection criteria were developed through subjective analysis of individual temperature, salinity, and potential density profiles from all oceans, though the greatest emphasis was placed on the Southeast Pacific and Southwest Atlantic. The algorithm

initially produces a temperature MLD estimate (referred to as the temperature algorithm). If the profile also includes salinity, the algorithm subsequently determines the MLDs of the salinity and potential density profiles. The salinity MLD estimate mainly serves to verify the potential density MLD estimate (referred to as the density algorithm) if they are at the same depth. The complete algorithm is provided in online at http://mixedlayer.ucsd.edu.

Visual examination of the numerous profiles and the algorithm's MLDs confirms that the algorithm successfully identifies the MLD. The new algorithm avoids many of the pitfalls of threshold and gradient methods; the threshold methods overestimate the MLD relative to the other methods and the gradient methods find more anomalous MLDs than the other methods. Section 4 compares the algorithm's results to those of standard threshold and gradient methods. For the data set considered in this paper (introduced in Section 2), the temperature algorithm especially improves upon the temperature threshold and gradient methods. Assuming that density MLD estimates are more reliable than temperature MLD estimates (as found by Lukas and Lindstrom (1991)), the standard deviations of the differences between the density algorithm MLDs and the three temperature method MLDs can serve as a rough measure of each temperature method's accuracy. The temperature algorithm's MLDs nearly match the density algorithm's MLDs; the standard deviation of the difference between the temperature algorithm and density algorithm MLDs is 31 dbar, whereas for the temperature threshold and the temperature gradient methods, the standard deviation of the differences with the density algorithm MLDs are 62 dbar and 121 dbar, respectively. The density algorithm tends to find slightly shallower MLDs than the density threshold method. The density gradient method finds many anomalous MLDs and is less reliable than either of the other density methods. Preliminary results of applying the algorithms to a larger Southern Ocean data set, courtesy of Shenfu Dong, generally support the findings from the study region (Dong et al., 2008). The algorithm's greatest utility lies in its ability to find accurate MLDs using only temperature profiles. It can easily be adapted to work with XBT and other temperature-only profiles.

The new algorithm is used to examine Subantarctic Mode Water (SAMW) and Antarctic Intermediate Water (AAIW) formation using Argo data. SAMW is the name given to the waters encompassed by the deep mixed layers immediately north of the Antarctic Circumpolar Current (ACC). AAIW, a subset of SAMW, can be traced as a

relatively low salinity tongue throughout almost all of the Southern Hemisphere and the tropical oceans at about 1000 m depth (Deacon, 1937). AAIW is believed to form in the Southeast Pacific Ocean upstream of Drake Passage (McCartney, 1977; England et al., 1993; Talley, 1996). The AAIW formation region is a good place to test the algorithm because it features a strong seasonal thermocline in the summer and deep winter mixed layers rivaled only by the North Atlantic, and it is monitored by a collection of Argo floats. The region has been relatively unstudied during the winter. Sections 5 discusses the results of applying the algorithm to Argo data from the SAMW/AAIW formation region.

2.2   Data

This study uses temperature and salinity profiles from 277 profiling floats deployed in the Southeast Pacific and Southwest Atlantic Oceans as part of the Argo program (Roemmich et al., 2001). In addition, randomly-selected profiles from Argo floats in other oceans are used to test the algorithm. Argo is a global observing system of 3000 floats designed to give upper and middle layer fields for temperature and salinity for the world's oceans. Argo floats are designed to provide a temperature accuracy of 0.005 °C and a salinity accuracy of 0.01 PSU.

The region of interest for this study encompasses sections of the Southern Pacific and Atlantic Oceans from 40°S to 66°S and 110°W to 35°W (Figure 2.1). Within this region, Argo floats collected 15,037 profiles between October 2002 and November 2008 (available online at: http://www.usgodae.org/Argo/Argo.html). In 2002, Canada deployed 6 floats in the South Pacific and the United Kingdom deployed 4 floats in the South Atlantic. These floats were supplemented with larger deployments in March 2004 and April 2005. Since 2005, additional deployments and an influx of floats from the growing Argo array have vastly increased the number of profiles in this region. Argo floats typically profile to 2000 meters and measure temperature, salinity, and pressure at 70 depth levels. Sample spacing for most floats is less than 20 meters to depths of 400 meters, below which the spacing increases to 50 meters. Figure 2.2 shows the temperature, potential density, salinity, and sampling interval for a typical Argo profile. The longest float record contained 95 profiles, whereas the shortest contained only 1 profile. All of the profiles included both temperature and salinity data.

Profiles collected before November 2005 were manually examined to remove in-
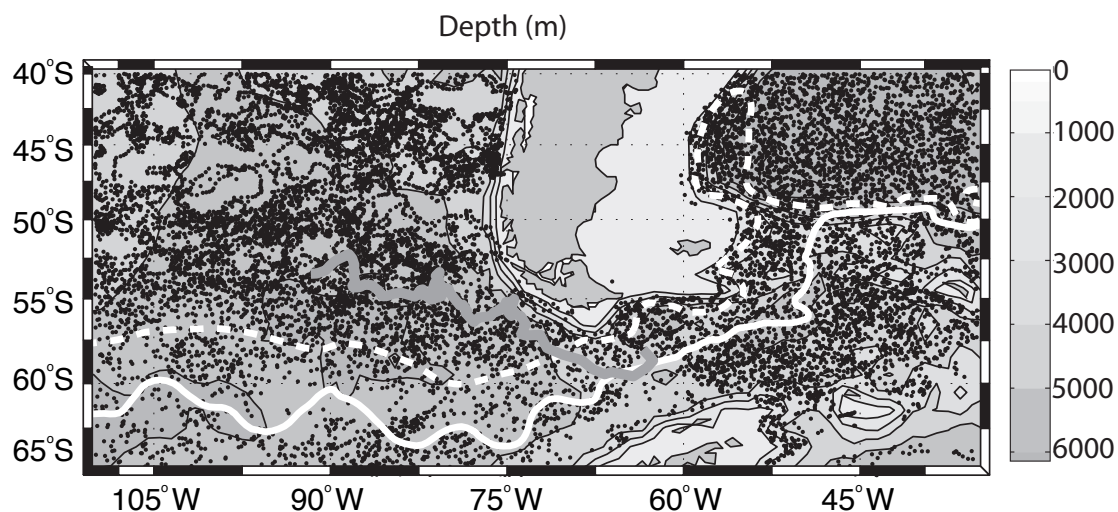
Figure 2.1: Profile locations of 277 Argo floats in the South Pacific and Atlantic Oceans. The profiling floats collected 13601 temperature and salinity profiles between February 2002 and November 2008. The time separation between each float's subsequent profiles is 10 days. The study region extends from 40°S to 66°S and 110°W to 35°W. The climatological Subantarctic and Polar Fronts are represented by the white dashed and solid lines (Orsi et al., 1995). The track of float 3900082 is in grey. The bathymetry is contoured at 1000 meter intervals.
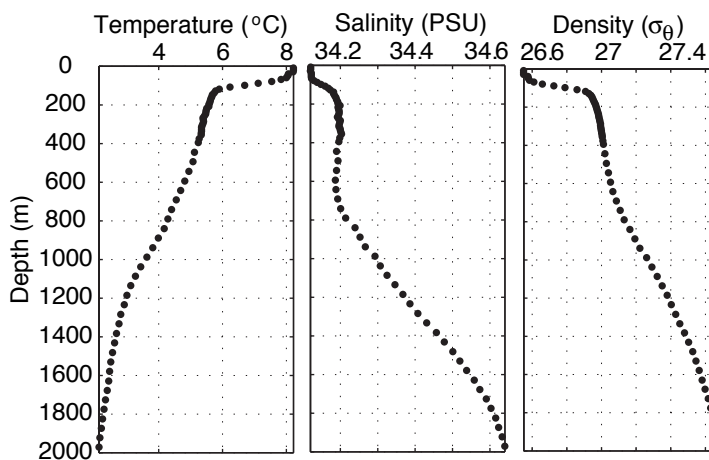
Figure 2.2: Example Argo profiles of temperature, potential density, and salinity to 2000 meters from float 3900082 on January 29, 2003 at 52.7°S and 89.7°W. To 400 meters the float's sampling interval is 10 meters, after which it increases to 50 meters. This profile is from a Canadian Argo float.

consistencies in temperature, salinity, and pressure. Most floats sampled at regular pressure levels, though the Canadian Argo floats often sampled at irregular pressures and required substantial editing. Float profiles that failed to meet basic quality controls or lacked locations or time stamps were eliminated. Temperature-Salinity (TS) plots allowed the comparison of float data to two World Ocean Circulation Experiment (WOCE) sections, P17E, along 50°S in the Southeastern Pacific, and P19C, along 88°W (Tsuchiya and Talley, 1998). Except for visually examining the float salinity profiles to confirm that they were largely consistent with the salinity observed during the WOCE cruises, no calibrations of the floats' salinities were performed. This quality control process trimmed the field to 13601 profiles. The locations of these profiles are shown in Figure 2.1. Potential density was calculated for each profile.

2.3   Methodology

This section outlines the algorithm's procedure for finding MLDs. In brief, the algorithm models the profile's general shape, calculates a suite of possible MLD values, and then looks for groupings and patterns within the possible MLDs to select the final MLD estimate for each profile. It does this separately for each temperature, salinity, and potential density profile to produce final MLD estimates for the temperature and potential density profiles. The temperature algorithm is detailed in this section because it offers a substantial improvement over its threshold and gradient counterparts. The salinity and potential density algorithms work in a similar fashion. The entire algorithm is supplied in online supplemental material. The following description of the temperature algorithm is divided into three parts. The first part describes how the algorithm calculates the five possible MLD values. The second part explains how the algorithm selects the final MLD estimate from the pool of possible MLDs. The third part presents an example.

2.3.1   Assembling the possible MLD values

Examples of typical summer and winter profiles are shown in Figure 2.3, as well as the five possible MLD values that the temperature algorithm calculates for each profile. For temperature profiles, the five possible MLD measures are: the intersection between the mixed layer and thermocline fits (MLTFIT), the temperature maximum (TM), the
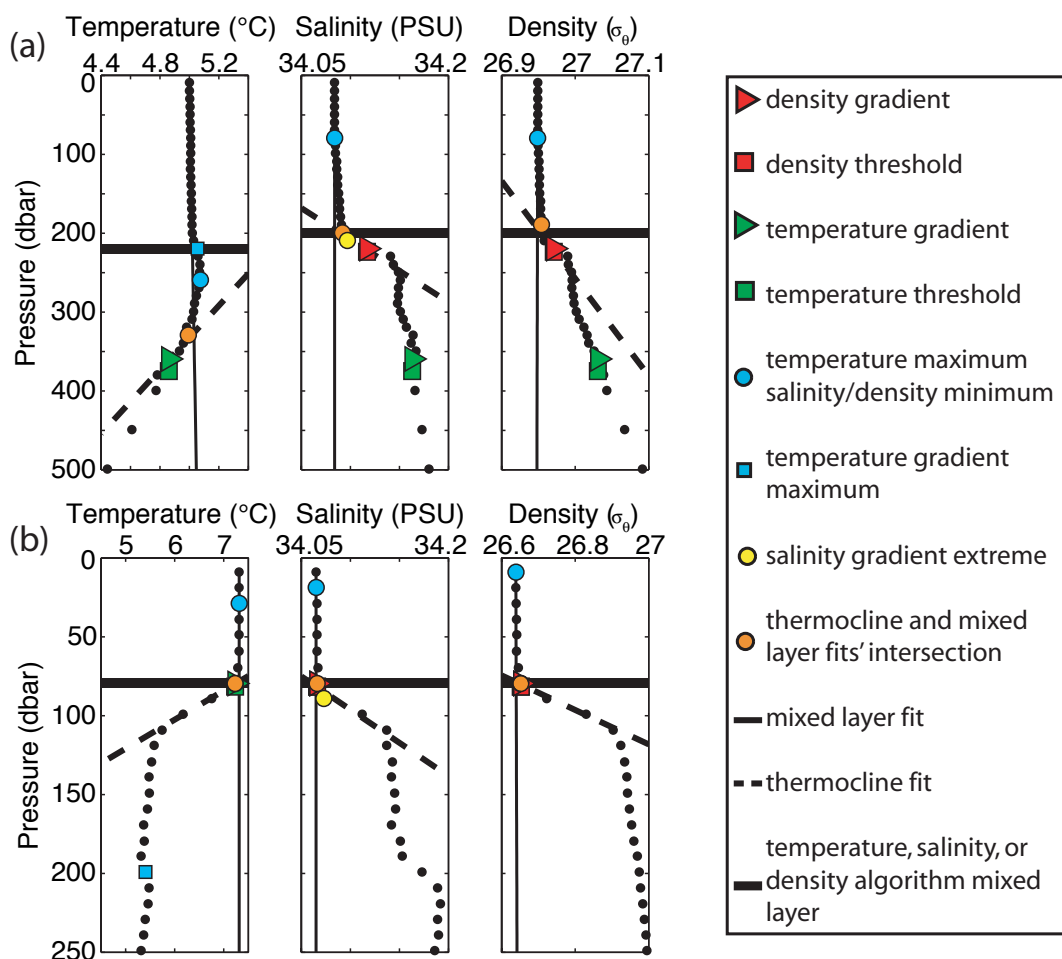
Figure 2.3: Temperature, salinity, and potential density profiles (black dots) collected by float 3900085 in (a) winter and (b) summer. The winter profile was collected on July 12, 2003 in the South Pacific Ocean at 54.3°S and 87.8°W. The summer profile was collected on February 12, 2003 at 52.6°S and 89.4°W. The algorithm identifies a unique MLD for each temperature, salinity, and density profile (horizontal bold solid lines). The temperature algorithm does not use the density threshold MLD. The algorithm's mixed layer (thin solid line) and thermocline (dashed line) fits are also plotted. The five mixed layer estimates used in the temperature algorithm's selection process are: the intersection of the mixed layer and thermocline fits (MLTFIT, orange circle), the temperature maximum (TM, light blue circle), the temperature gradient estimate (DTM, green triangle, criterion of 0.005°C dbar^{-1}), co-located temperature and temperature gradient maximum (TDTM, located at the temperature gradient maxima, light blue square), and the temperature threshold MLD (TTMLD, green square, de Boyer Montégut et al. (2004)'s threshold of 0.2°C). For the density and salinity profiles the threshold density MLD (red square, de Boyer Montégut et al. (2004)'s threshold of 0.03 kg m^{-3}) and the gradient density MLD (red triangle, criterion of 0.0005 kg m^{-3} dbar^{-1}) are plotted for each profile. The light blue circles correspond to profile minima and the yellow circle corresponds to the salinity gradient extreme.

Table 2.1: Acronyms for the temperature algorithm's five possible MLDs.

MLTFIT	Intersection of mixed layer and thermocline fits
TM	Temperature maximum
DTM	Temperature gradient MLD estimate
TDTM	Co-located temperature and temperature gradient maxima
TTMLD	Temperature threshold MLD estimate

temperature gradient MLD estimate (DTM), nearly co-located temperature and temperature gradient maxima (TDTM; this represents intrusions at the base of the mixed layer), and the threshold MLD estimate (TTMLD). For reference, the five possible MLD values for temperature are listed in Table 2.1. For salinity, the possible MLD values are the density threshold MLD estimate, the salinity minimum, the salinity gradient extreme, co-located salinity and salinity gradient minima (representing an intrusion at the base of the mixed layer, if one exists), the intersection of the salinity mixed layer and thermocline fits, and the final temperature algorithm MLD. For density, the algorithm uses the density threshold MLD estimate, the density gradient MLD estimate, the intersection of the density mixed layer and thermocline fits, as well as the temperature threshold MLD estimate, co-located temperature and temperature gradient maxima, the temperature maximum, and the final MLDs from the temperature and salinity algorithms.

The algorithm derives its five possible MLD values for temperature as follows:

1. The algorithm initially uses a simple threshold method to find the approximate MLDs of the temperature and potential density profiles. Starting at the surface, threshold methods search progressively deeper levels until they find a level where the temperature or potential density differs from the surface reference value by a specified threshold. To calculate the temperature threshold MLD (TTMLD), the algorithm looks for the minimum depth for which $|T(p) - T(p_o)| \geq \Delta T_t$, where T is the temperature, p is the pressure, p_o is the reference pressure, and ΔT_t is the temperature threshold. The algorithm linearly interpolates the temperature profile between Argo measurements to find the depth that exactly matches the threshold criterion. For potential density, the algorithm implements the same procedure but uses the potential density anomaly, σ_θ. Following de Boyer Montégut et al. (2004), 0.2°C and 0.03 kg m^{-3} are used as the

threshold difference criteria and the Argo measurement closest to 10 dbar as the surface reference value.

2. The algorithm then calculates the temperature, salinity, and potential density gradients using a difference formula. For calculating the temperature gradient, the algorithm uses

$$\frac{\partial T_i}{\partial p_i} = \frac{T_i - T_{i+1}}{p_i - p_{i+1}}, \tag{2.1}$$

where i is the depth measurement index from the surface ($i = 1$) to one level above the bottom of the profile ($i = n - 1$). The algorithm first uses the gradient to calculate gradient MLDs for temperature (DTM) and potential density; it finds the depth at which the temperature and potential density gradients exceed specified gradient criteria. Following Dong et al. (2008), the algorithm uses a potential density gradient criterion of 0.0005 kg m^{-3} dbar^{-1}. It uses a temperature gradient criterion of $0.005°$C dbar^{-1}. This criterion was found to better approximate the MLD than larger criteria. For temperature, the algorithm looks for the depth at which $|\partial T(p)/\partial p| \geq 0.005°$C dbar^{-1}. If these gradient criteria are not met, the algorithm takes the depth of the maximum of the gradient's absolute value as the gradient MLD. To aid in identifying persistent change in each of the variables (such as the thermocline, later identified in step 4), the algorithm then smoothes the gradient with a three-point running mean to eliminate small vertical-scale spikes and small-scale intrusions.

3. The algorithm fits a straight line to the mixed layers of the temperature, salinity, and potential density profiles. Starting at the surface, the algorithm uses the first two points of the profile to calculate a straight-line least-squares fit to the mixed layer. It increases the depth and the number of points used in the fit until it reaches the bottom of the profile. For each fit the algorithm calculates the error by summing the squared difference between the fit and the profile over the depth of the fit. For temperature, this is expressed as:

$$E_i = \sum_{j=1}^{i}(T(j) - T_{MLfit_i}(j))^2. \tag{2.2}$$

In this example, E_i is the error for the ith fit (extending to depth index i), T_{MLfit_i} is the straight-line temperature fit, and i indexes the depth of the fit and the fit itself. There is a different error and fit for each i. The algorithm only sums the error over the depth of the fit, so a straight line fit no longer accurately describes the profile as the depth of the fit increases past the mixed layer, and the error increases. The algorithm normalizes

the errors by dividing each E_i by the total sum of the errors. The normalized error, E_{i_n}, is given by:

$$E_{i_n} = \frac{E_i}{\sum_{i=2}^{n} E_i}. \tag{2.3}$$

Normalizing the error removes dependence on the magnitude of the seasonal thermocline and produces a unit-less error. The algorithm takes the deepest mixed layer fit that satisfies a specified error tolerance, $E_T = 10^{-10}$. This small error tolerance is used to ensure that the mixed layer fit closely matches the mixed layer and does not use any points in the seasonal thermocline; it consistently produces a straight line fit to the mixed layer and results in the average use of 3.5 Argo measurements per mixed layer fit. Varying the error tolerance has little effect on the MLDs found by the algorithm (Figure
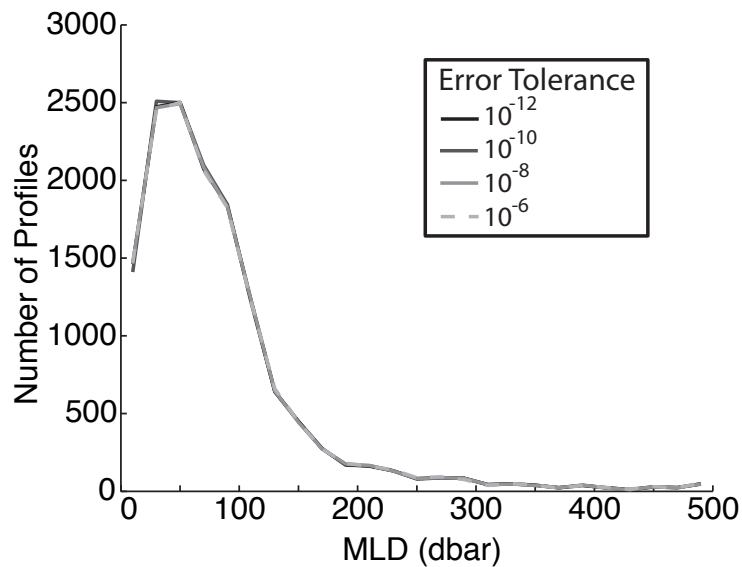
Figure 2.4: Distribution of MLDs for the temperature algorithm with varying error tolerances of 10^{-6} (dashed grey), 10^{-8} (light grey), 10^{-10} (dark grey), and 10^{-12} (black). An error tolerance of 10^{-10} was chosen for the algorithm.

2.4).

4. Straight lines are fit to the seasonal thermoclines of each temperature, salinity, and potential density profile. The algorithm later finds the intersection of the thermocline and mixed layer fits as one possible measure of the MLD. The algorithm identifies the center of the seasonal thermocline for each profile as the depth of the maximum of the absolute values of the smoothed temperature, salinity, and potential density gradients

(calculated in step 2). For temperature, this is expressed as:

$$i_{therm} = \left| \frac{\partial T_i}{\partial p_i} \right|_{max}, \tag{2.4}$$

where i_{therm} is the depth index of the thermocline. It is quite successful in the summer, when the seasonal thermocline is easily identifiable as a large spike in the dT/dp, dS/dp, and $d\sigma_\theta/dp$ profiles. The algorithm uses i_{therm} and the two neighboring points ($i_{therm} - 1$ and $i_{therm} + 1$) to fit a straight line to the seasonal thermocline. Because Argo floats record few data points in the thermocline, including more than three points in the fit skews the thermocline vertically.

5. The algorithm assembles the possible values of the MLD for each temperature, salinity, and potential density profile. The five possible MLD values for the temperature algorithm are given below in (a) through (e).

(a) The first possible MLD is from the temperature threshold calculation (TTMLD). This is represented as:

$$p(T = T_o \pm 0.2 \text{ °C}), \tag{2.5}$$

where T_o is the surface reference temperature. The salinity and density algorithms use the density threshold, $p(\sigma_\theta = \sigma_{\theta_o} + 0.03 \text{ kg m}^{-3})$, where σ_{θ_o} is the surface reference potential density.

(b) The second MLD value for temperature is the result of the gradient MLD calculation (DTM). This is represented as:

$$p\left(\left| \frac{\partial T}{\partial p} \right| > 0.005 \text{ °C dbar}^{-1} \right). \tag{2.6}$$

If the gradient criterion is not met, the algorithm takes the gradient extreme:

$$p\left(\left| \frac{\partial T}{\partial p} \right|_{max} \right). \tag{2.7}$$

The potential density gradient MLD is calculated in the same manner, using a criterion of 0.0005 kg m^{-3} dbar^{-1}. The salinity algorithm uses the salinity gradient extreme.

(c) The algorithm then finds the depth of the temperature maximum (TM) and the salinity and density minima. For temperature, this is represented as:

$$p(T_{max}). \tag{2.8}$$

(d) For the fourth possible MLD value, the algorithm searches for a specific feature in the profile. Surface cooling and intense wind events in the winter deepen the

mixed layer and erode the summer thermocline. This process often leaves subsurface anomalies of temperature or salinity at the base of the mixed layer. An example of this feature is shown in Figure 2.3 (a). The algorithm identifies these features in temperature profiles by searching for maxima of the smoothed temperature gradient profiles within a specified distance (the parameter ΔD) of subsurface temperature maxima (TM); the algorithm takes the shallowest of the two as the fourth possible MLD value (TDTM). This is represented as:

$$p\left(\left(\frac{\partial T}{\partial p}\right)_{max}, T_{max}\right)_{min} \text{ if } \left|p\left(\left(\frac{\partial T}{\partial p}\right)_{max}\right) - p(T_{max})\right| \leq \Delta D. \qquad (2.9)$$

The fourth possible MLD value is set to zero if the temperature and temperature gradient maxima are separated by more than ΔD:

$$0 \text{ if } \left|p\left(\left(\frac{\partial T}{\partial p}\right)_{max}\right) - p(T_{max})\right| > \Delta D. \qquad (2.10)$$

Figure 2.3 (a) provides an example of a subsurface temperature anomaly where TM and the temperature gradient maximum are separated by 50 dbar. Setting ΔD, the maximum allowable separation between TM and temperature gradient maxima, to 100 dbar allows the algorithm to identify temperature intrusions at the base of the mixed layer. As shown in Figure 2.5, this value of ΔD encompasses the profusion of deep MLDs scattered around 0.0 dbar of separation between TM and the temperature gradient maximum.

(e) The final possible MLD value represents another physical feature in the profile; the depth of the intersection point of the mixed layer fit and the seasonal thermocline fit (MLTFIT). This is designed to capture the MLD in profiles with homogenous mixed layers near the surface and strong seasonal thermoclines. For temperature, this is represented as:

$$p(T_{MLfit} = T_{Thermfit}), \qquad (2.11)$$

where T_{MLfit} is the mixed layer fit and $T_{Thermfit}$ is the seasonal thermocline fit. MLT-FIT is set to 0 if the fits do not intersect. The salinity and density algorithms use their respective fits. This MLD measure works especially well in the summer, when the algorithm can easily identify the seasonal thermocline, but occasionally falters in the winter, when the seasonal thermocline is weak.

2.3.2 Selecting the MLD estimate

The algorithm selection process is divided into two parts. In summary, the algorithm first determines whether the profile resembles a summer or winter profile.
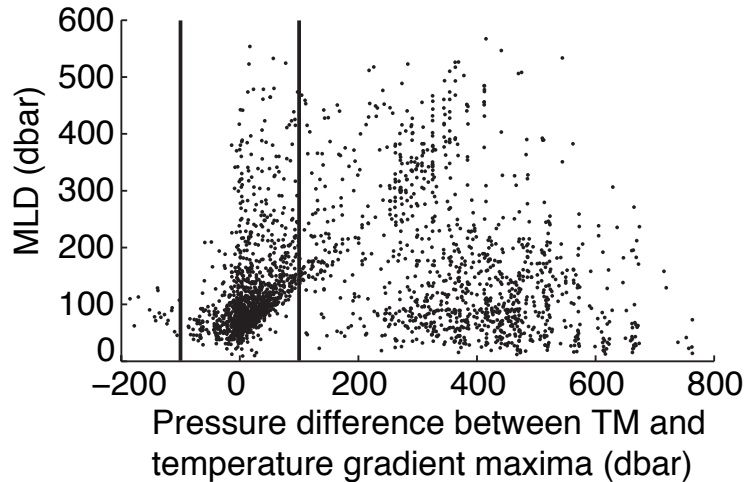
Figure 2.5: Pressure difference between the depth of the temperature maxima and the temperature gradient maxima $(p(TM) - p((\partial T/\partial p)_{max}))$ plotted against the MLD as determined by the density threshold method. Only values for subsurface temperature maxima or temperature gradient maxima are plotted. The vertical lines denote pressure differences of -100 and +100 dbar.

Simplistically, a summer profile generally consists of a homogenous mixed layer near the surface, a seasonal thermocline where the temperature, salinity, and density change abruptly with depth, and a deep water layer that is seasonally invariant. Winter profiles lack the strong summer thermocline; the mixed layer visually blends into the underlying waters. The algorithm's initial MLD selection is dependent on the "type" of profile. Then, over a series of steps, the algorithm examines the other possible MLD values, looks for clusters of possible MLD values, and either confirms or replaces the initial MLD selection. The algorithm selects MLDs for each temperature and potential density profile; the algorithm also selects a salinity MLD, but it only serves to verify the potential density MLD. The temperature algorithm's selection process is outlined in the following steps:

1. Before the algorithm can search for clusters of the possible MLDs, it must first define a depth range over which to search. The possible MLDs are rarely at the same Argo depth levels, but might be within 15 dbar of each other; this range parameter, r, allows the algorithm to identify clusters of possible MLDs separated by less than r and to accommodate Argo's sampling scheme. The algorithm also avoids selecting temperature maxima at the surface by checking whether they are deeper than r. The distribution of
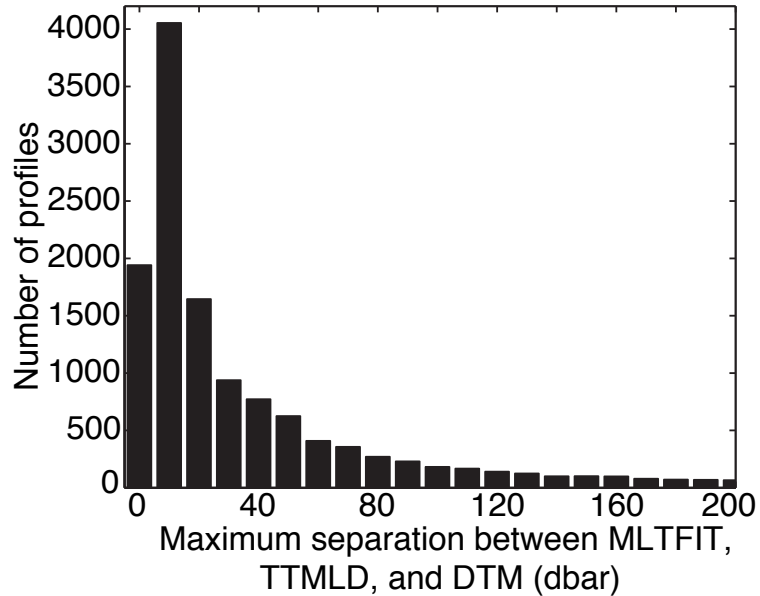
Figure 2.6: Distribution of the maximum separation between MLTFIT, TTMLD, and DTM $((|\text{TTMLD}-\text{DTM}|, |\text{MLTFIT}-\text{DTM}|, |\text{TTMLD}-\text{MLTFIT}|)_{max})$. The bin width is 10 dbar, so the first bin, centered at 0 dbar separation, includes all profiles where these MLD estimates are separated by a maximum of 5 dbar.

the maximum separation between MLTFIT, TTMLD, and DTM, plotted in Figure 2.6, determines the value of r. MLTFIT, TTMLD, and DTM are separated by a maximum of 5 dbar for 1941 profiles; 4054 profiles have maximum separations of 5 to 15 dbar and 1645 profiles have maximum separations of 15 to 25 dbar. Because there is a fall-off in the number of profiles with maximum separations greater than 25 dbar, r is set to 25 dbar, the approximate equivalent of two Argo depth bins.

2. The algorithm uses the temperature or potential density change across the thermocline (ΔT and $\Delta \sigma_\theta$) to estimate whether a profile is summer-like (strong thermocline beneath the mixed layer) or winter-like (weak thermocline beneath the mixed layer). The temperature change across the thermocline, in terms of Argo depth bins, is defined as $T(i_{MLTFIT}) - T(i_{MLTFIT} + 2)$, where i_{MLTFIT} is the Argo depth index of MLTFIT; the potential density change is calculated in the same manner. The algorithm compares this temperature change to a third parameter, ΔT_c, a temperature change cutoff, for information about the strength of the seasonal thermocline and to decide if a profile is summer-like or winter-like. Figure 2.7 plots the temperature and potential density changes across the thermocline against the MLD, as well as the temperature and
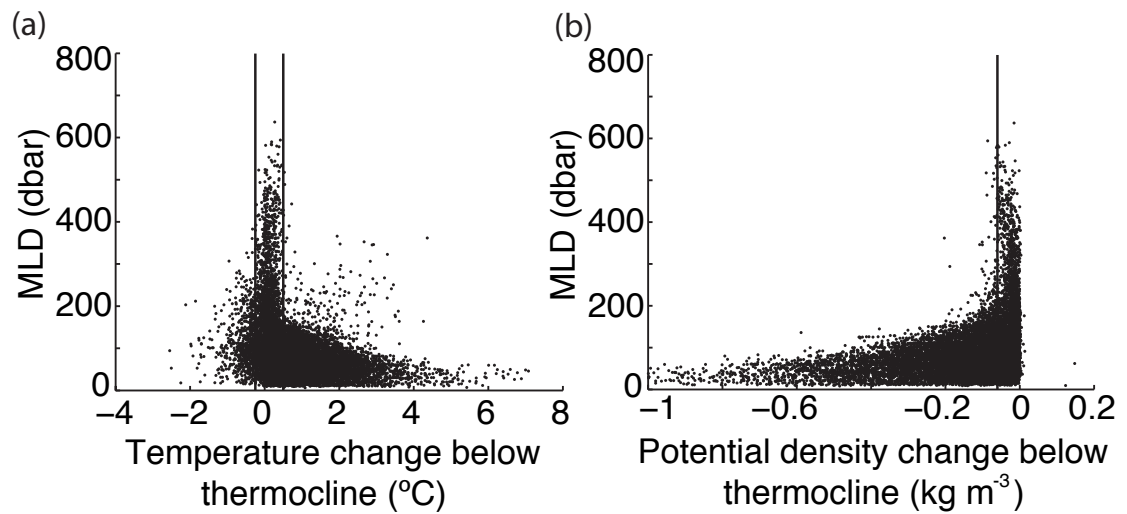
Figure 2.7: In (a), the temperature change across the thermocline, ΔT, is plotted against MLD; (b) is the same, but for potential density. In both cases the MLD was found using the density threshold method. The vertical lines correspond to the temperature and potential density change cutoffs. The temperature change cutoffs are 0.5°C and -0.25°C. The potential density change cutoff is -0.06 kg m^{-3}. Temperature changes within the temperature cutoffs and potential density changes greater than the potential density cutoff are treated as winter-like profiles by the algorithm.

potential density change cutoffs. If the temperature change is within the cutoff region
$(0.5°C > \Delta T > -0.25°C)$, then the algorithm initially assumes that the profile is winter-
like. The potential density change cutoff, σ_{θ_c}, is -0.06 kg m^{-3} ($\Delta\sigma_\theta > -0.06$ kg m^{-3} for
winter-like profiles). In the study region, 83% of profiles with MLDs deeper than 200
dbar are within the temperature change cutoff range; 90% of the profiles with MLDs
deeper than 200 dbar are within the potential density change cutoff.

3. If ΔT falls outside of the winter cutoff (ΔT_c), the algorithm initially as-
sumes that the profile features a strong thermocline. Figure 2.8 shows the temperature
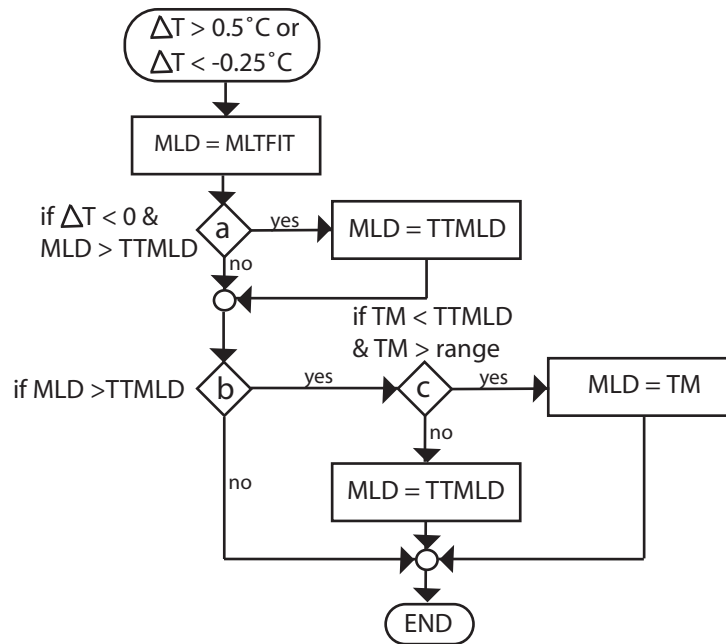
Figure 2.8: The temperature algorithm's summer flow diagram.

algorithm's flow path for these summer-like profiles. Because summer-like profiles are
assumed to feature strong thermoclines, the algorithm first assigns the intersection of the
mixed layer and thermocline fits, MLTFIT, to the final MLD. Steps 3.1 and 3.2 check
the other possible MLDs to ensure that this MLD assignment is reasonable; if not, the
MLD is re-assigned to one of the other possible MLDs as described.

3.1. Profiles with multiple temperature inversions, such as polar profiles, often
have shallow MLDs but lack identifiable seasonal thermoclines. These profiles can cause
the algorithm to mis-identify the thermocline and thus confound MLTFIT. To identify
these profiles, in Figure 2.8 (a) the algorithm searches for temperature increases beneath

the mixed layer (ΔT$<$ 0) and checks whether MLTFIT overestimated the MLD relative to the temperature threshold MLD, TTMLD. If so, the algorithm assigns the MLD to TTMLD.

3.2. This step treats TTMLD as an upper bound on the MLD to evaluate MLT-FIT and TM. The algorithm first tests the current MLD against TTMLD (Figure 2.8 (b)); the final MLD is assigned to the current MLD if it is shallower than TTMLD. If the current MLD is deeper than TTMLD, the algorithm subsequently examines the temperature maximum, TM. If TM is beneath the surface and shallower than TTMLD, then the algorithm assigns the MLD to TM; if not, then it assigns the MLD to TTMLD (Figure 2.8 (c)).

4. If ΔT is within the winter cutoff range, the temperature algorithm assumes that the profile is winter-like and follows the flow path shown in Figure 2.9. The selection
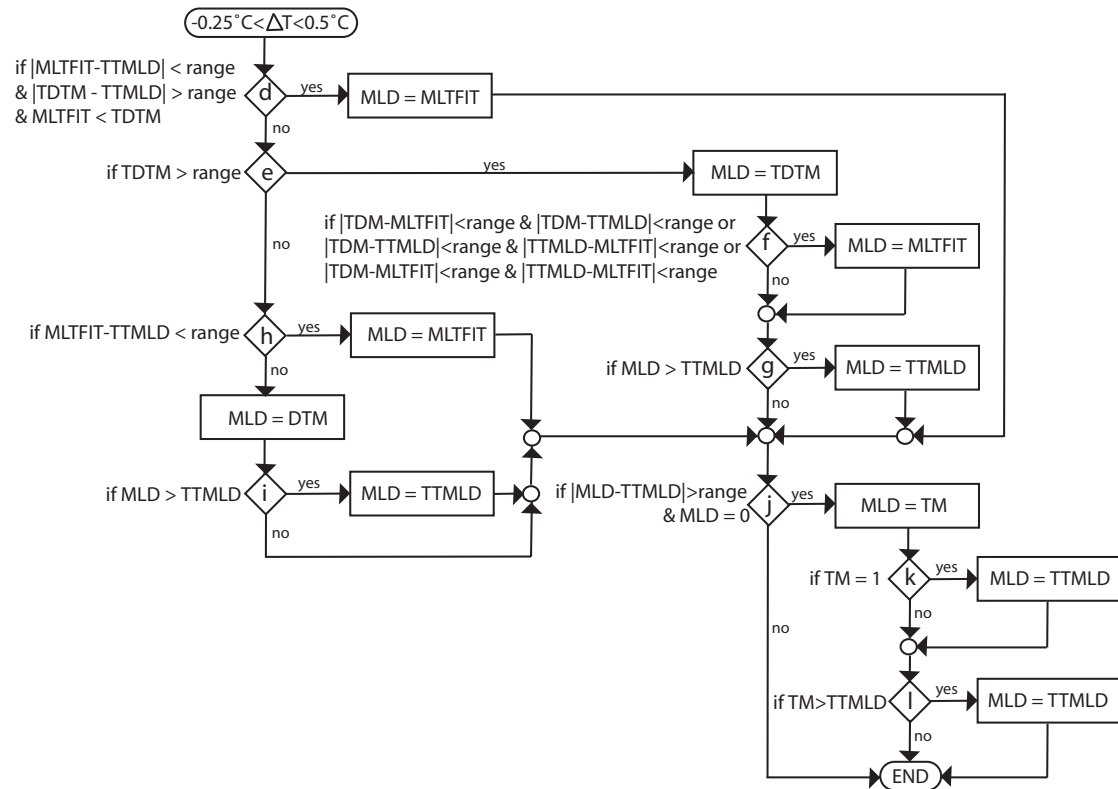
Figure 2.9: The temperature algorithm's winter flow diagram.

process is conducted in the following steps:

4.1 The algorithm first tests whether it identified a seasonal thermocline (and

therefore a meaningful MLD value for MLTFIT) by checking if MLTFIT and TTMLD are in close proximity ($|\text{MLTFIT}-\text{TTMLD}| < r$) and by comparing MLTFIT to TDTM. TDTM represents a subsurface temperature anomaly at the base of the mixed layer, if such an anomaly exists. When the algorithm fails to identify a seasonal thermocline, it often instead identifies the permanent thermocline, producing a very deep estimate for MLTFIT. Therefore, if MLTFIT is shallower than TDTM and if TDTM and TTMLD differ by more than r, the algorithm has most likely identified the seasonal thermocline, so the MLD is assigned to MLTFIT (Figure 2.9 (d)) and the algorithm proceeds to step 4.4.

4.2 If the algorithm did not capture the seasonal thermocline (the MLD was not assigned to MLTFIT), then the algorithm searches for temperature anomalies at the base of the mixed layer; if TDTM exists and is not at the surface, the algorithm assigns the MLD to TDTM (Figure 2.9 (e)). It then checks that TDTM does not greatly differ from the other possible MLDs (Figure 2.9 (f) and (g)). It accomplishes this by first searching for clusters of three other MLD estimates; it determines if any two sets of MLTFIT, TTMLD, and DTM ($|\text{MLTFIT}-\text{TTMLD}|$, $|\text{MLTFIT}-\text{DTM}|$, or $|\text{DTM}-\text{TTMLD}|$) are separated by less than r, as they often are for profiles with seasonal thermoclines. If so, the MLD is assigned to MLTFIT (Figure 2.9 (f)). As a final check, if the MLD is deeper than TTMLD, the MLD is reassigned to TTMLD in Figure 2.9 (g). The algorithm then proceeds to step 4.4.

4.3 Convective winter mixing does not necessarily produce temperature anomalies at the base of the mixed layer, so TDTM does not necessarily exist. Figure 2.9 (h) and (i) are evaluated if TDTM does not exist and if the algorithm did not assign the MLD to MLTFIT. The algorithm again considers MLTFIT by comparing MLTFIT to TTMLD; if MLTFIT is not more than r deeper than TTMLD ($\text{MLTFIT}-\text{TTMLD} < r$, in Figure 2.9 (h)), the MLD is assigned to MLTFIT. If MLTFIT is more than r deeper than TTMLD, the MLD is assigned to the gradient MLD estimate, DTM. To test DTM, the algorithm checks whether it is deeper than TTMLD (Figure 2.9 (i)). If DTM is deeper than TTMLD, the MLD is reassigned to TTMLD.

4.4 The algorithm checks for poor thermocline fits by testing whether the final MLD estimate has been assigned to the surface and whether this near surface MLD differs from TTMLD ($|\text{MLD}-\text{TTMLD}| < r$), If these conditions are met, the MLD is most likely shallow and the algorithm assigns the MLD to TM (Figure 2.9 (j)). In two

final checks, the algorithm assigns the MLD to TTMLD if TM is at the surface or if it is deeper than TTMLD (Figure 2.9 (k) and (l)).

2.3.3   Example selection processes

Figure 2.3 (a) provides an example of the temperature algorithm's selection process. The algorithm first compares the temperature change below MLTFIT to the temperature change cutoff, ΔT_c. For this profile, ΔT is 0.06^{o}C, so the algorithm considers this a winter-like profile and follows the path in Figure 2.9. MLTFIT is deeper than TDTM (Figure 2.9 (d)), so the algorithm looks for a subsurface temperature maximum at the base of the mixed layer (Figure 2.9 (e)); TDTM is greater than r, so the algorithm assigns the MLD to TDTM. In Figure 2.9 (f), the algorithm checks whether there might be a thermocline, but MLTFIT is 100 dbar shallower than TTMLD. TDTM is also much shallower than TTMLD (Figure 2.9 (g)), so the final MLD is assigned to TDTM. From visual inspection of the salinity and potential density profiles, it is clear that the temperature algorithm's MLD is closer to the actual MLD than the temperature threshold and temperature gradient MLDs.

Figure 2.3 (b) provides another example. This profile has a strong seasonal thermocline (ΔT of 1.4^{o}C), so the algorithm considers this a summer-like profile and initially assigns the MLD to MLTFIT. MLTFIT is at the same depth as TTMLD, so the MLD assignment does not change.

For the temperature profiles in this study, the algorithm uses the intersection of the mixed layer and thermocline fits as the MLD for 58% of the profiles in the study region. The threshold MLD is used for 22% of the profiles and the gradient MLD is used for 9%. Co-located temperature and temperature gradient maxima are used for 7% of the profiles and temperature maxima are used for 4%.

2.4   Comparison to other methods

The MLDs produced by six different methods are considered here to evaluate the algorithm. The six MLD estimates are: (1) the temperature algorithm's estimate, (2) the density algorithm's estimate, (3) a temperature threshold estimate (threshold of 0.2°C), (4) a density threshold estimate (threshold of 0.03 kg m^{-3}), (5) a temperature gradient estimate (criterion of of 0.005°C dbar^{-1}), and (6) a density gradient estimate (criterion of 0.0005 kg m^{-3} dbar^{-1}). The threshold estimates are from de Boyer Montégut et al.

(2004) and the gradient criteria are derived from Dong et al. (2008). We evaluate the six methods by first examining their MLDs for a single profile and then a single float record. For the float record, the exact MLD was determined by visually identifying the homogenous mixed layer and comparing it to the six methods' MLD estimates. The analysis is then expanded to the distribution of MLDs for all of the profiles in the Southeast Pacific and Southwest Atlantic. The algorithm and threshold MLD distributions for the entire Southern Ocean are briefly examined.

2.4.1 Individual profile comparison

The algorithm's MLDs are first compared to threshold and gradient MLDs for the two sets of temperature and potential density profiles in Figure 2.3. For the winter profile (Figure 2.3 (a)) the algorithm calculates MLDs of 220 dbar for temperature and 200 dbar for potential density. The temperature threshold (ΔT of 0.2°C) calculates a MLD of 375 dbar; the density threshold ($\Delta\sigma_\theta$ of 0.03 kg m^{-3}) calculates a MLD of 225 dbar. The temperature gradient method (criterion of of 0.005°C dbar^{-1}) identifies a MLD of 360 dbar and the density gradient method (criterion of 0.0005 kg m^{-3} dbar^{-1}) identifies a MLD of 220 dbar. The temperature algorithm seizes upon the close proximity of the temperature maximum and the temperature gradient maximum to identify the MLD (Equation (2.9) represents the MLD). The temperature threshold and temperature gradient methods both overestimate the MLD by nearly 150 dbar. In general, winter profiles, with no strong, sustained gradients in density or temperature below the mixed layer, prove difficult for the temperature threshold and gradient methods. The density threshold and gradient methods slightly overestimate the MLD compared to the density algorithm.

For the summer profile (Figure 2.3 (b)) the algorithm calculates MLDs of 80 dbar for both temperature and potential density using the intersection between the thermocline and mixed layer fits (represented by Equation (2.11)). All of the threshold and gradient methods find similar MLDs, though the threshold MLDs are slightly deeper. These MLDs are representative of typical results. In general, the algorithm, threshold, and gradient methods produce similar summer MLDs; the strong seasonal thermocline and pycnocline prohibit the threshold and gradient methods from advancing very far below the actual MLD and ensure that the algorithm identifies and fits the thermocline.

2.4.2 Individual float comparison
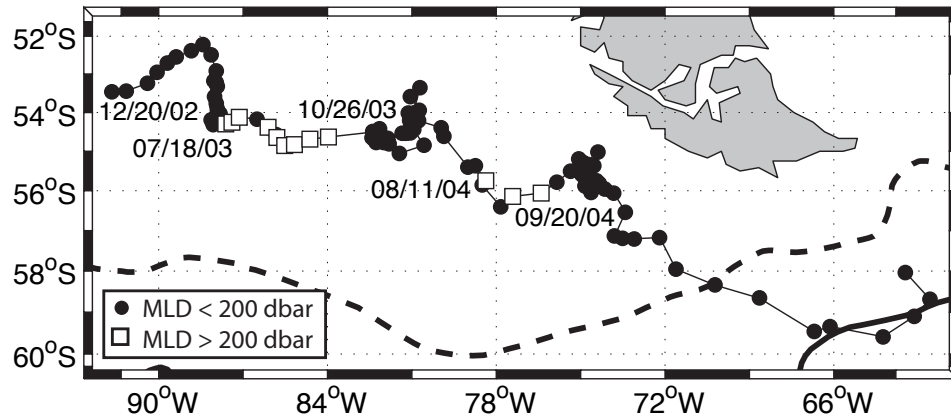
Figure 2.10: Track of Argo float 3900082. The float was deployed in the Pacific Ocean off Chile at 53.5°S and 91.7°W in December of 2002 and has since passed through Drake Passage. Profiles with mixed layers deeper than 200 dbar are represented by open squares (MLD calculated by the density algorithm). The first period of deep mixed layers lasted from July 18, 2003 to October 26, 2003; the second lasted from August 11, 2004 to September 20, 2004. The Subantarctic and Polar Fronts are represented by the dashed and solid lines (Orsi et al., 1995).

Having examined two profiles, the comparison between the algorithm, threshold, and gradient methods is expanded to an entire float record. Figure 2.10 presents the track of float 3900082. The float was deployed in December, 2002, off the coast of Chile in the Southeast Pacific Ocean. It collected 95 profiles before it ceased transmitting in August, 2005. Entwined in numerous eddies, it crossed the ACC and was carried through Drake Passage and into the polar ocean surrounding Antarctica. The potential density time-series of float 3900082 is plotted in Figure 2.11 (a), in addition to three MLD time-series. Figure 2.11 (b) is the temperature time series of the float, again with three MLD time-series.

The density algorithm, threshold, and gradient methods generally produce comparable MLDs in summer (Figures 2.3 (b) and 2.11 (a)). Subtle gradients in temperature, salinity, and density that blend mixed layers into deep waters, as well as a wide variety of subsurface features, such as salinity intrusions, often obscure the MLD of winter profiles. The density threshold's winter MLDs are generally deeper than the density algorithm's winter MLDs (Figure 2.11 (a)). As in Figure 2.3 (a), weak density gradients at the base of the mixed layer cause the density threshold method to slightly overestimate the MLD
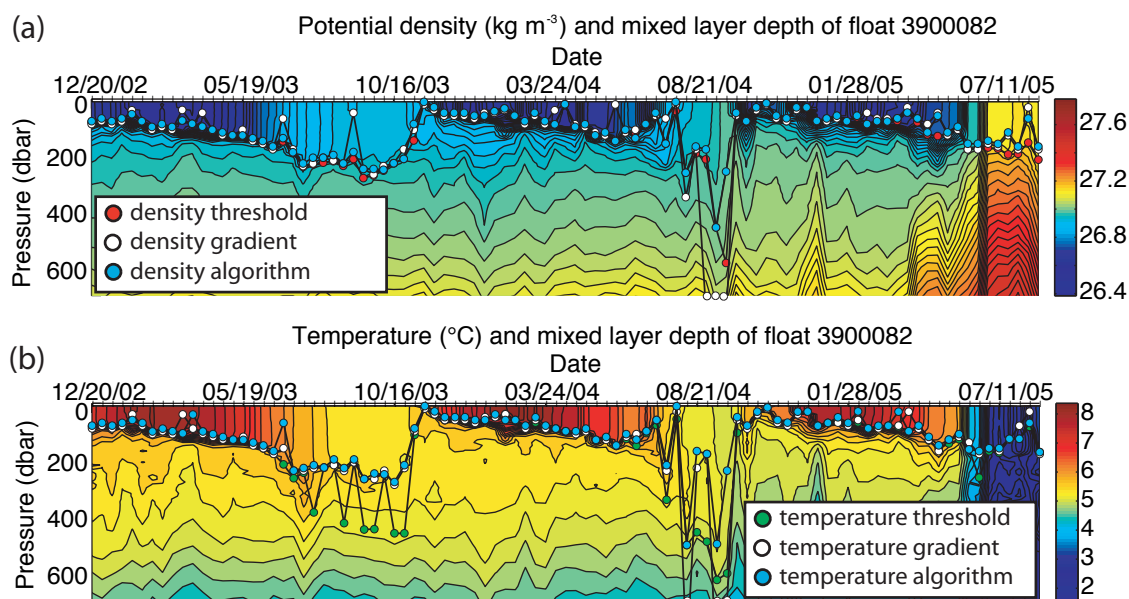
Figure 2.11: Time series of (a) potential density and (b) temperature for float 3900082. The profiles extend to 2000 dbar but are only shown to 700 dbar. The time series runs from December 2002 to August 2005; the tick marks along the time axis denote 10 day profile separation. In (a), the contour intervals are 0.02 kg m^{-3} and three MLD time series are plotted: the density threshold calculation, using de Boyer Montégut et al. (2004)'s criterion (red circle), the density gradient calculation (white circle), using a criterion of 0.0005 kg m^{-3} dbar^{-1}, and the density algorithm's result (light blue circle). Solid lines connect each MLD timeseries. In (b), the contour interval is 0.2°C, the temperature threshold is plotted in green (de Boyer Montégut et al. (2004)'s criterion), the temperature gradient result is plotted in white (criterion of 0.005°C dbar^{-1}), and the temperature algorithm result is plotted in light blue.

in winter. The density gradient is much more erratic than the other methods, as evidenced by its frequent jumps to both shallow and extraordinarily deep MLDs in Figure 2.11 (a). In winter 2004, the density gradient method estimates the MLD to be over 100 dbar deeper than the other methods. These anomalous density gradient MLDs do not fit with the exact MLD's general trend.

In summer the temperature algorithm, temperature threshold, and temperature gradient methods find similar MLDs. The MLD time-series in Figure 2.11 (b) closely follow each other in the summer because of the strong temperature gradient beneath the mixed layer. The temperature algorithm is generally much more successful at finding winter MLDs than the temperature threshold and gradient methods. Judging the actual MLD visually, the temperature threshold method overestimates many MLDs during the winter of 2003 by approximately 200 dbar (Figure 2.11 (b)). Likewise, the temperature gradient method overestimates many MLDs during the winter of 2004. An example of this is given in Figure 2.3 (a), where the temperature is nearly uniform to a depth of 300 dbar. The MLD and density of this set of profiles are determined by salinity; the MLD is clearly 200 dbar in the salinity and density profiles. The temperature threshold and gradient methods estimate the MLD to be 375 and 360 dbar, respectively. The temperature algorithm identifies a small temperature protrusion at the base of the mixed layer and estimates a MLD of 220 dbar. This estimate is tied to a physical feature of the profile and, compared to the temperature threshold and gradient MLDs, is much closer to the actual MLD. The temperature algorithm's continued success at finding such features is evident in its MLD's similarity to the density algorithm and density threshold MLDs (Figure 2.11 (a) and (b)).

2.4.3   Southeast Pacific and Southwest Atlantic comparison

An analysis of the six methods' MLDs from the Southeast Pacific and Southwest Atlantic Oceans confirms that the temperature algorithm improves on the temperature threshold and gradient methods and that the density algorithm offers a slight improvement over the other density methods. The MLD distributions of the six methods are plotted in Figure 2.12. The temperature threshold method consistently overestimates deep MLDs relative to the other methods; it finds more MLDs between 250 and 600 dbar than any other method. The temperature and density gradient methods find the deepest MLDs; the temperature gradient method finds nearly 250 MLDs deeper than 700 dbar,
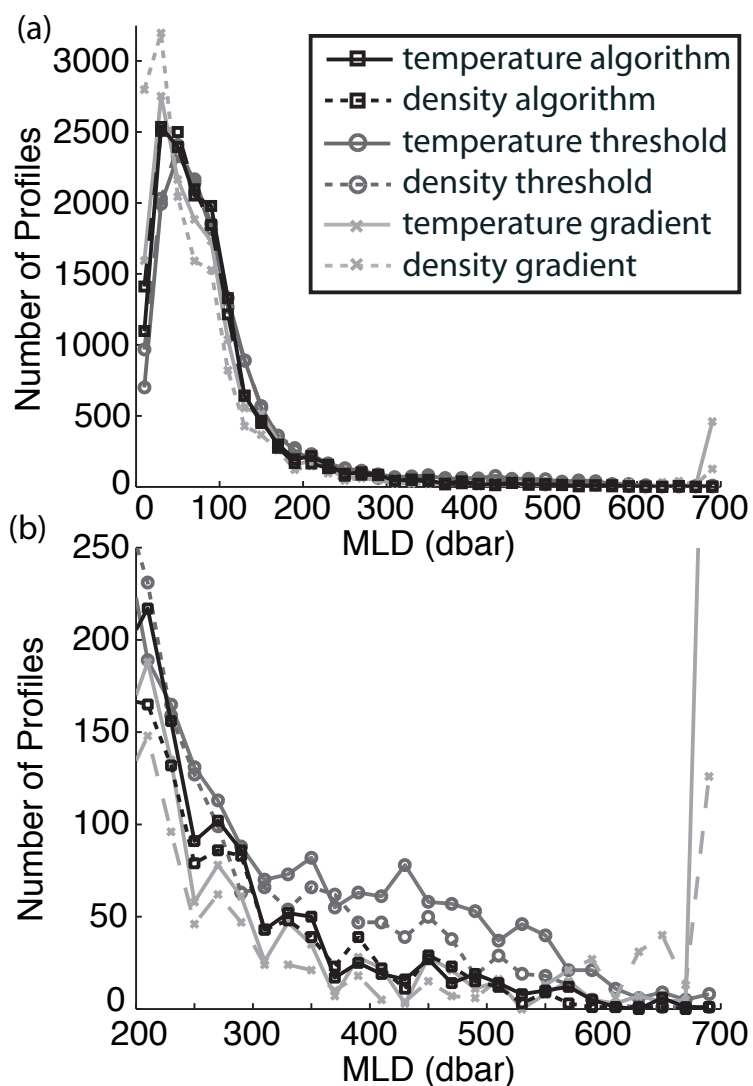
Figure 2.12: Distribution of MLDs found in the entire study region by six methods: temperature algorithm (solid black), density algorithm (dashed black), temperature threshold using de Boyer Montégut et al. (2004)'s criterion (solid dark grey), density threshold using de Boyer Montégut et al. (2004)'s criterion (dashed dark grey), temperature gradient (solid light grey, criterion of $0.005°$C dbar^{-1}) and density gradient (dashed light grey, criterion of 0.0005 kg m^{-3} dbar^{-1}); (a) is the distribution for all MLDs and (b) is the distribution for MLDs between 200 and 700 dbar. The sawtooth pattern of the distribution in (b) is due to the depth sampling scheme of the Argo floats.
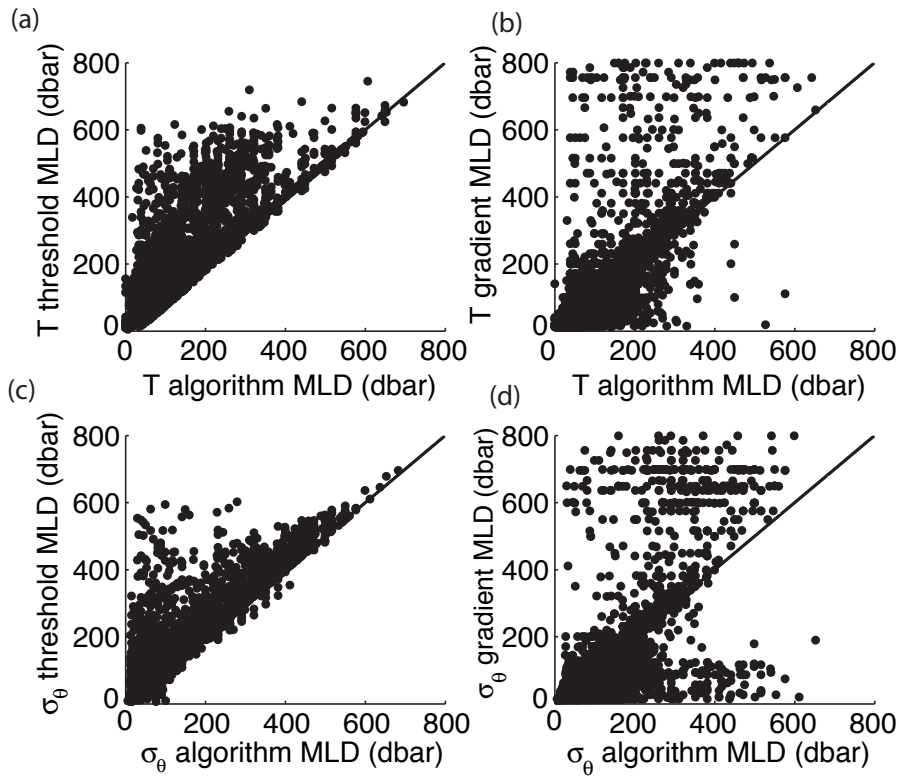
Figure 2.13: Comparison of algorithm, threshold, and gradient MLD estimates from the study region: (a) temperature algorithm and temperature threshold, (b) temperature algorithm and temperature gradient, (c) density algorithm and density threshold, and (d) density algorithm and density gradient. The thin black line has a slope of 1.

and the density gradient method finds 100 MLDs deeper than 700 dbar. None of the other methods find mixed layers this deep. Figure 2.11 (a) and (b) contain multiple examples of these deep gradient method MLDs. Both gradient methods, particularly density, are also prone to finding anomalously shallow MLDs; in Figure 2.12 (a), both gradient methods find many more shallow MLDs (50 dbar or less) than the other methods.

Figure 2.13, the scatter of temperature and density algorithm MLDs against the temperature and density threshold MLDs, shows that the temperature and density algorithms generally find shallower MLDs than their threshold counterparts. The temperature threshold method systematically overestimates many MLDs relative to the temperature algorithm, forming a cluster of MLDs highlighted in Figure 2.14 (a). Of these highlighted profiles, the temperature algorithm uses co-located temperature and
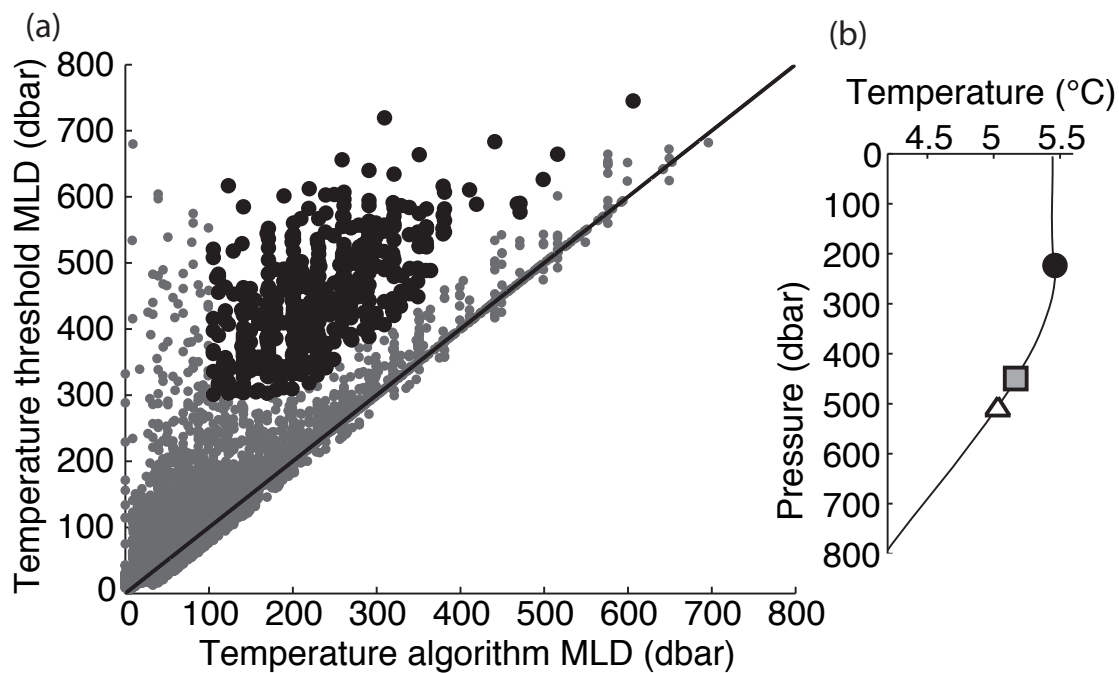
Figure 2.14: Comparison of (a) temperature threshold and temperature algorithm MLDs, with a subset of MLDs highlighted by black dots; (b) plots the average temperature profile for the subset of profiles. Three average MLD estimates are plotted in (b): the average temperature algorithm MLD (black circle), the average temperature gradient MLD (white triangle) and the average temperature threshold MLD (grey square). The thin black line in (a) has a slope of 1.
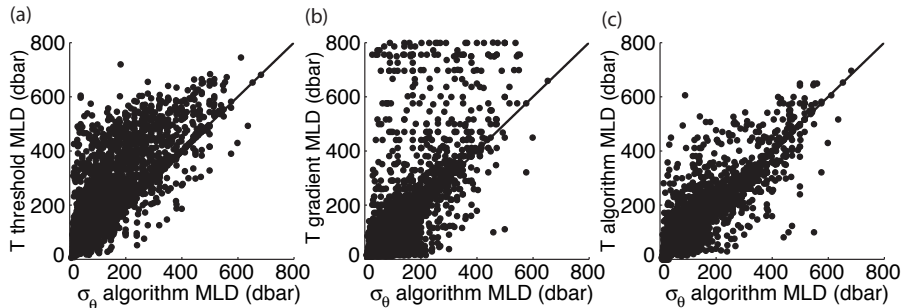
Figure 2.15: Comparison of (a) temperature threshold, (b) temperature gradient, and (c) temperature algorithm MLDs to the density algorithm MLD. The thin black line has a slope of 1.

temperature gradient maxima (Equation (2.9)) to find the MLD for 75% of the profiles. This results in an average temperature algorithm MLD that better approximates the actual MLD than the average temperature threshold method, which overestimates the MLD by nearly 200 dbar (Figure 2.14 (b)).

Numerous examples of anomalously shallow and deep MLDs found by the temperature and density gradient methods are shown in Figure 2.11 (a) and (b); Figure 2.13 (b) and (d) confirm the gradient methods' tendencies to find anomalous MLDs. The temperature gradient method finds more than 250 MLDs deeper than 700 dbar; these anomalously deep gradient MLDs correspond to temperature algorithm MLDs ranging from 25 to 600 dbar (Figure 2.13 (b)). The temperature gradient method's proclivity to overestimate the MLD in profiles with weak gradients beneath the mixed layer is also illustrated in Figure 2.14 (b); for the subset of profiles, the average temperature gradient MLD is 250 dbar deeper than the average temperature algorithm MLD. Figure 2.13 (d) illustrates the density gradient method's tendency to find anomalous MLDs; there is a large cluster of points corresponding to density gradient MLDs from 0 to 100 dbar and density algorithm MLDs varying from 0 to 600 dbar. Likewise, a similar cluster corresponds to density gradient MLDs deeper than 600 dbar and density algorithm MLDs between 25 and 600 dbar. Brainerd and Gregg (1995) found gradient methods to be less stable than threshold methods, a result mirrored in these distribution plots.

Figure 2.15 compares the density algorithm MLDs to the three temperature methods' MLDs. Table 2.2 lists the means and standard deviations of the six methods' MLDs, as well as the mean and standard deviation of the difference between the temperature methods' MLDs and the density algorithm MLD. Together, these provide a means to

Table 2.2: MLD means and standard deviations in dbar for the six methods: temperature algorithm (TA), temperature gradient (TG), temperature threshold (TT), density algorithm (DA), density gradient (DG), and density threshold (DT), as well as the means and standard deviations for the differences between DA and the three temperature methods.

	TA	TG	TT	DA	DG	DT	DA-TA	DA-TG	DA-TT
mean	90	110	109	86	81	99	-4	-24	-23
std	75	161	105	72	105	86	31	121	62

evaluate the temperature methods relative to the density algorithm.

The cluster of deep temperature threshold MLDs highlighted in Figure 2.14 (a) is reproduced in Figure 2.15 (a). There is no similar cluster in the scatter of density algorithm MLDs against the temperature algorithm MLDs (Figure 2.15 (c)). The temperature threshold method systematically overestimates deep MLDs, producing a mean MLD of 109 dbar. This mean MLD is 19 dbar deeper than the temperature algorithm's mean MLD and 23 dbar deeper than the density algorithm's mean MLD.

The temperature gradient method does not systematically overestimate the MLD relative to the density algorithm; rather, it identifies occasional anomalously deep MLDs compared to the density algorithm (Figure 2.15 (b)). These anomalously deep MLDs result in a mean temperature gradient MLD of 110 dbar (24 dbar deeper than the mean density algorithm MLD) and a MLD standard deviation that is much larger than any other method, 161 dbar.

The temperature algorithm more closely tracks the density algorithm than the other temperature methods. The standard deviation of the difference between the temperature algorithm and the density algorithm MLDs is much smaller than the standard deviation of the difference between the density algorithm and the other temperature methods (Table 2.2). The temperature gradient method produces many MLDs similar to the temperature algorithm but is hampered by its tendency to find anomalously deep MLDs. The temperature threshold method routinely overestimates the depth of deep mixed layers.
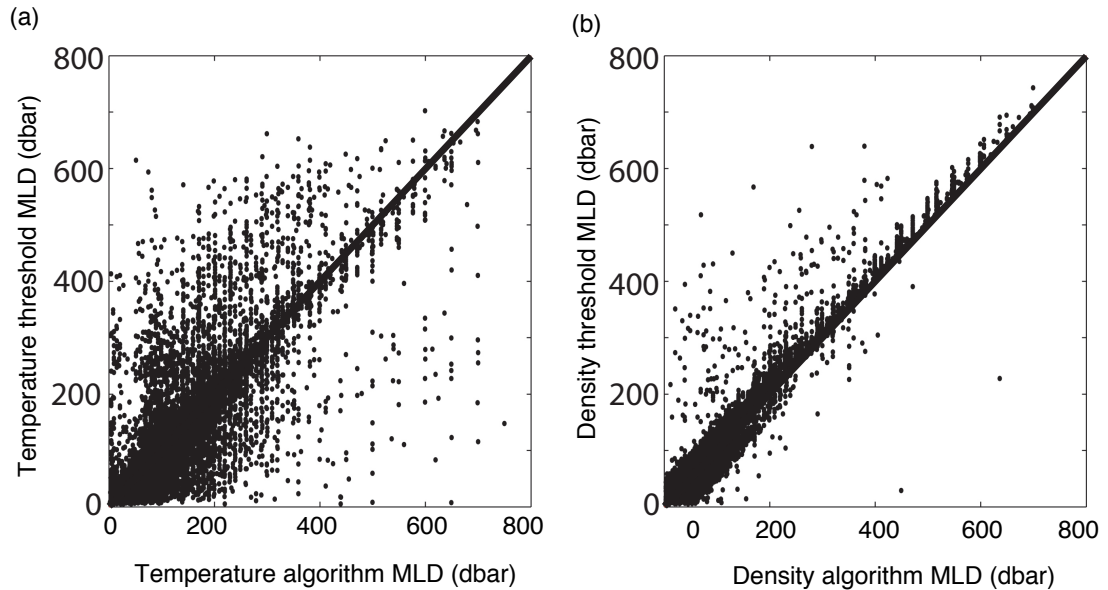
Figure 2.16: Algorithm and threshold MLD estimates for the entire Southern Ocean for (a) the temperature algorithm and temperature threshold and (b) the density algorithm and density threshold. The thin black line has a slope of 1. These plots were provided by Shenfu Dong.

2.4.4 Southern Ocean comparison

Expanding our analysis to algorithm and threshold MLD distributions for the entire Southern Ocean produces a more complex distribution of MLDs, though the general pattern is similar to the MLD distributions from the study region. Dong et al. (2008) produced a Southern Ocean MLD climatology from Argo float data and provided us with plots of the scatter of MLDs found by the temperature and density algorithms and threshold methods for the entire Southern Ocean (Figure 2.16). As in the study region, the density methods produce very similar MLDs, though the threshold method tends to overestimate deep MLDs relative to the algorithm. The temperature methods exhibit much more scatter than the density methods. In general, the temperature algorithm estimates shallower MLDs than the temperature threshold method; a cluster of MLDs similar to the cluster highlighted in Figure 2.14 (a) is also visible in the Southern Ocean distribution.

The algorithm's ability to identify physical features in the profiles allows it to track and identify the MLD more accurately than a traditional threshold method. Like-

wise, it is more stable than gradient methods. This accuracy makes the algorithm useful for identifying density-compensating layers and barrier layers. An accurate estimation of the mixed layer depth is important for ocean models that tune their turbulent mixing parameters to match observed ocean mixed layer depths (Noh et al., 2002). Because of its complexity, the algorithm is slower than threshold and gradient methods and it, like any MLD-finding method, is liable to be stumped by unusual profiles.

2.5   Application to SAMW mixed layers

One region of the ocean known for persistent deep winter mixed layers and water mass formation is immediately north of the ACC. The ACC encircles Antarctica as it flows eastward through the southern Pacific, Indian, and Atlantic Oceans. There are three fronts in the ACC associated with zonal jets in the current (Orsi et al., 1995). The deepest mixed layers in the Southern Ocean are associated with the northern side of the northernmost front, the Subantarctic Front (SAF). The waters defined and enclosed by these deep mixed layers were termed SAMW by McCartney (1977). AAIW, characterized by relatively low salinity, high oxygen, and low potential vorticity, is the densest, deepest, and freshest SAMW and is thought to form in the Southeast Pacific just before the ACC enters the Drake Passage (McCartney, 1977; England et al., 1993; Talley, 1996; Hanawa and Talley, 2001).

AAIW can be traced as a relatively low salinity (34.4 psu) tongue throughout almost all of the southern hemisphere and the tropical oceans at about 1000 m depth (Deacon, 1937). The global-scale heat and freshwater transports associated with AAIW's movement into the world's oceans reflect its relevance to studies of the Earth's climate and of the ocean's global overturning circulation (Keeling and Stephens, 2001; Pahnke and Zahn, 2005). The SAMW and AAIW formation region is an ideal location to test methods for finding MLDs. The mixed layer exhibits great variability; in winter, the mixed layers north of the SAF can reach depths of 500 meters and blend into deeper waters and remnant mixed layers. This makes determining the exact mixed layer difficult for many MLD-finding methods. Likewise, polar waters and summer stratification test methods' abilities to detect shallow mixed layers.

The algorithm identifies deep mixed layers, providing the locations, time of year, and temperature, salinity, and density characteristics of this oceanic process that has historically proven difficult to observe. The locations of SAMW formation, identified by
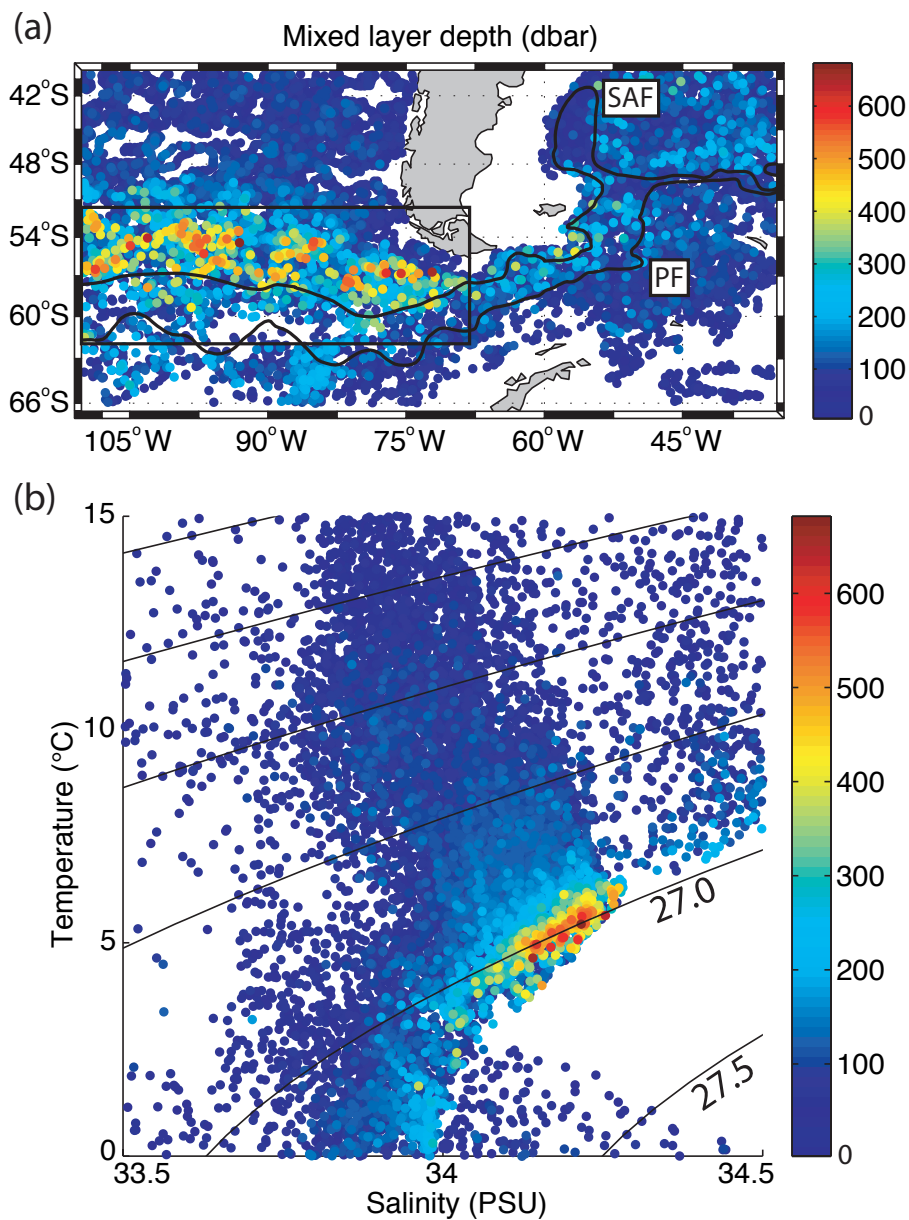
Figure 2.17: The (a) MLD map and (b) mixed layer T-S diagram for the MLDs calculated by the density algorithm. The MLDs range from 0 dbar (blue) to 650 dbar (red). In (a), the Subantarctic and Polar Fronts are represented by the solid lines (Orsi et al., 1995). Profiles from the boxed region (50°S to 62°S and 110°W to 68°W) are used in the MLD time series in Figure 2.18 and the zonally-averaged salinity section in Figure 2.19. Each mixed layer's average temperature and salinity are plotted in (b); the color of each point corresponds to the MLD.

deep mixed layers, are found by mapping all of the MLDs found by the density algorithm (Figure 2.17 (a)). The deepest mixed layers are found in the Southeast Pacific Ocean, immediately north of Orsi et al. (1995)'s climatological Subantarctic Front. The deepest MLDs are about 650 dbar, with numerous MLDs reaching 500 dbar. No regions of similarly deep mixed layers are found in the South Atlantic.

The density algorithm's MLD map (Figure 2.17 (a)) generally features a broader region of deep mixed layers compared to four MLD climatologies (not shown). The 95% oxygen saturation depth has been used by Talley (1999) as a proxy for the MLD. Using 2005 World Ocean Atlas 95% oxygen saturation depth as a MLD proxy produces MLDs of roughly the same depth range as the algorithm, but the climatology's region of deep MLDs is more localized and centered at 92°W and 53°S (Antonov et al., 2006). Levitus and Boyer (1994)'s MLD climatology shows MLDs of 1000 meters, far deeper than anything found by Argo in the study region. Their deepest MLDs are also localized and centered at 87°W and 52°S. The deepest MLDs of de Boyer Montégut et al. (2004)'s climatology reach 450 m at 90°W and do not extend farther west. Kara et al. (2003) used 1994 World Ocean Atlas density in constructing their climatology. The spatial distribution of their MLDs is similar to the density algorithm's, but their MLDs reach 800 m, considerably deeper than any mixed layers found by the density algorithm.

The temperature, salinity, and potential density characteristics of the deep mixed layers are identified with a T-S diagram (Figure 2.17(b)). The deepest mixed layers have average potential densities of approximately 27 kg m^{-3}, salinities of 34.1-34.2 psu, and temperatures of 4-5°C.

Figure 2.18 plots the MLD time series of the floats in the area of the Pacific with deep mixed layers. This region, from 50°S to 62°S and 110°W to 68°W, is boxed in Figure 2.17 (a). The deepest MLDs occur in August and September. The temporal extent of the deep MLDs was greater for the 2003 winter than for any other. The mixed layers gradually deepen over the course of six months leading up to August and September, after which they quickly restratify. The average MLD reached in winter is approximately 300 dbar, though individual floats record MLDs exceeding 650 dbar. As shown in Section 4, the threshold methods overestimate the MLD relative to the algorithms. In particular, the temperature threshold method produces winter periods of deep mixed layers that are of earlier onset, greater duration, and greater depth than the temperature algorithm (Figure 2.18 (a)).
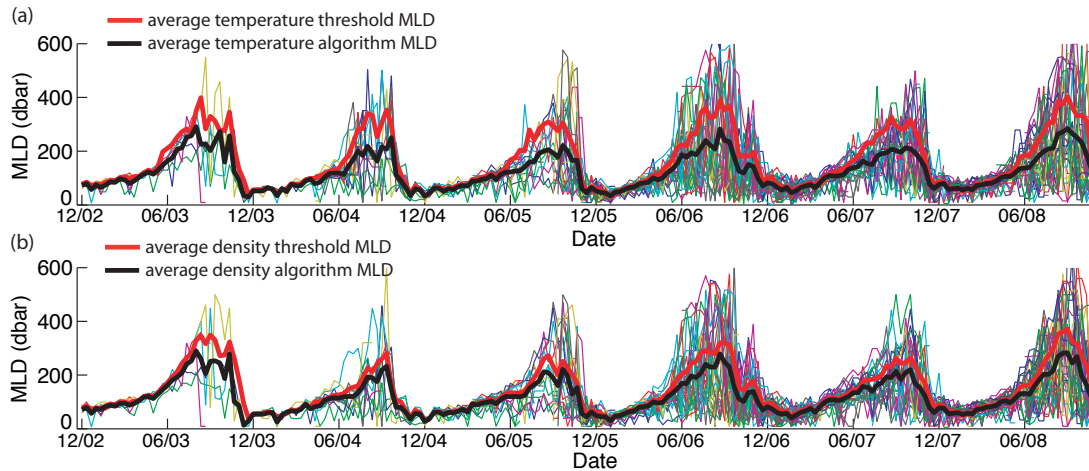
Figure 2.18: Time series of MLDs (thin colored lines) derived by the (a) temperature algorithm and (b) density algorithm for floats within the region of deep mixed layers in the Southeastern Pacific (50°S to 62°S and 110°W to 68°W). In (a), the average temperature algorithm MLD is plotted in black and the average temperature threshold MLD is in red; (b) plots the average potential density algorithm MLD in black and the average potential density threshold MLD in red.

To examine how the deep mixed layers relate to AAIW, the zonal average salinity for the Pacific study region during winter is plotted in Figure 2.19. From this average section the low-salinity water mass at mid-depth (500 to 600 decibars in Figure 2.19, between the 27.0 and 27.1 kg m^{-3} isopycnals) can be traced to a surface density out-cropping between 58°S and 60°S. The region of deep mixed layers corresponds to a sea surface salinity maximum between 54°S and 57°S. On average, these deep winter mixed layers in the Southeast Pacific Ocean appear to penetrate into the low-salinity layer at 56°S and inject low-salinity water of the correct salinity, density class, and depth as AAIW into the ocean interior.

2.6 Summary

A new algorithm was developed to find the MLD of individual Argo ocean pro-files. The algorithm fits straight lines to the mixed layer and thermocline, searches for subsurface property anomalies, and incorporates threshold and gradient methods to find the MLD. The temperature and density algorithms tend to find shallower MLDs than their threshold counterparts. The temperature algorithm MLD nearly matches the den-
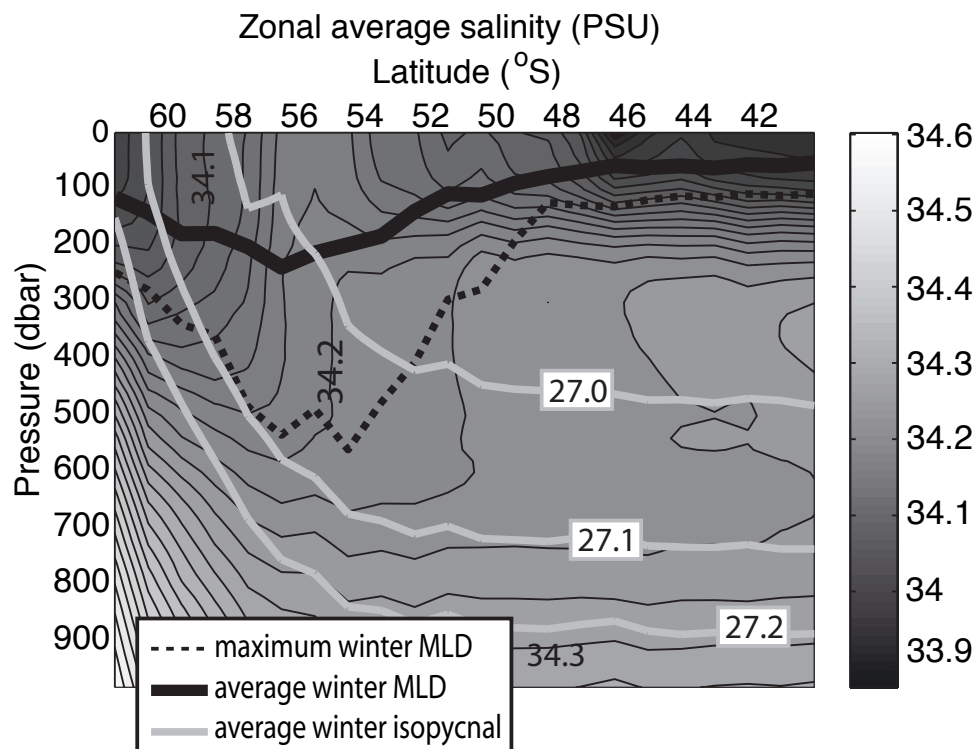
Figure 2.19: Zonally-averaged salinity of all profiles collected in the Southeastern Pacific region (Figure 2.17) during winter. The study period covers six winters, identified as intervals of deep mixed layers running from mid-June to early November for the years 2003 through 2008. An Akima spline was used to interpolate each profile to uniform vertical spacing, at which point they were averaged into one degree latitude bins. The salinity is contoured at 0.025 PSU intervals. The bold black line is the average winter MLD based on the density algorithm MLD of each profile. The dashed thin black line, representing the maximum winter MLD in the one degree bin, is the average of the five deepest MLDs, again determined by the density algorithm. Three potential density contours ($\sigma_\theta = 27.0$, 27.1, and 27.2 kg m^{-3}) are plotted in grey.

sity algorithm MLD. In the study region, the temperature algorithm offers a marked improvement over a temperature threshold method using the criterion of de Boyer Montégut et al. (2004); the temperature threshold method frequently overestimates winter MLDs by nearly 200 dbar for profiles in which the temperature algorithm successfully identifies temperature anomalies at the base of the mixed layer. The temperature algorithm is preferred over the temperature gradient method because of the gradient method's tendency to find anomalously deep MLDs. The density gradient method also produces many anomalous MLDs. The algorithm was used to investigate the formation of SAMW and AAIW in the Southeast Pacific and Southwest Atlantic Oceans. We find that the deepest MLDs routinely reach 500 dbar and occur north of the Orsi et al. (1995) mean SAF in the Southeastern Pacific Ocean. Within the Pacific study region, the deepest winter mixed layers occur in August and September at 57°S and are concurrent with the subsurface salinity minimum, a signature of AAIW.

ACKNOWLEDGEMENTS

Chapter 2 in its entirety is a reprint with no modifications to content of the article "A New Algorithm for Finding Mixed Layer Depths with Applications to Argo Data and Subantarctic Mode Water Formation" that appeared in Journal of Atmospheric and Oceanic Technology, 2009, 26, 1920-1939 (Copyright of the American Meteorological Society 2009). The dissertation author was the first author and primary researcher with contributions from the second author, Lynne Talley.

Chapter 3

The role of air-sea fluxes in Subantarctic Mode Water formation

3.1 Introduction

The deepest mixed layers in the Southern Ocean are found equatorward of the Subantarctic Front (SAF), the northernmost front of the Antarctic Circumpolar Current (ACC). Termed Subantarctic Mode Water (SAMW) by McCartney (1977), the waters enclosed in the deeply-mixed region are characterized by a potential vorticity minimum and an oxygen maximum. The warmest SAMW is found in the South Atlantic and western Indian Oceans. The densest, coolest, and freshest SAMW is formed in the southeast Pacific Ocean just before the ACC enters Drake Passage (McCartney, 1977; England et al., 1993; Talley, 1996; Hanawa and Talley, 2001). McCartney (1977) attributed the observed eastward freshening and cooling of SAMW from south of Africa to Drake Passage to the cumulative effects of air-sea fluxes of heat and precipitation.

SAMW is important to many global-scale processes. The formation of thick mode and intermediate water masses is a primary mechanism for sequestering anthropogenic CO_2 in the ocean interior (Sabine et al., 2002). SAMW forms the upper limb of the global overturning circulation (Sloyan and Rintoul, 2001) and renews the waters of the lower thermocline in the subtropical gyres (McCartney, 1982). The heat, freshwater, and carbon transports associated with SAMW's global-scale circulation confirm its relevance

to studies of the Earth's climate and of the ocean's global overturning circulation (Keeling and Stephens, 2001; Pahnke and Zahn, 2005).

Because of its importance to climate, many recent studies have investigated SAMW variability. The Southern Ocean's mid-depth warming is well documented, especially near the ACC (Gille, 2002). In the Pacific sector of the Southern Ocean, SAMW has warmed and freshened (Wong et al., 2001; Bryden et al., 2003), and this observed freshening may be attributed to anthropogenic climate change (Banks et al., 2000). Naveira Garabato et al. (2009) examined the interdecadal variability of SAMW in Drake Passage and determined that the variability was primarily due to modes of Southern Hemisphere climate variability, such as the Southern Annular Mode and El Niño-Southern Oscillation. As noted in Rintoul and England (2002a), the implications of observed freshening of SAMW are difficult to deduce without knowledge of the formation mechanisms.

Many processes contribute to SAMW formation: gyre inflow, cross-frontal advection in the form of Ekman transport, eddies, and intrusions; heat and freshwater fluxes at the air-sea interface and at the base of the mixed layer; and mixing. Many papers have focused on the importance of Ekman transport, which transports polar waters across the SAF into the SAMW formation region, citing that air-sea fluxes alone cannot account for the observed temporal variability of SAMW (Speer et al., 2000; Sloyan and Rintoul, 2001). Eddies have been shown to modify Ekman transport and air-sea fluxes (Sallée et al., 2008) and to influence SAMW property variability (Herraiz-Borreguero and Rintoul, 2010). Wind energy input to the ocean drives considerable mixing at and below the base of the mixed layer in the SAMW formation region (Sloyan et al., 2010). Chereskin et al. (2010) have shown that SAF meanders are quasi-stationary, and therefore the deep mixed layer regions maintain their position relative to the front on seasonal time scales, such as during the winter formation of SAMW.

Two recent hydrographic cruises in the southeast Pacific Ocean were designed to study formation of the densest variety of SAMW and its subsequent restratification and subduction. The first cruise, in austral winter (August 23 to October 5, 2005) observed the deep winter mixed layers. The 135 CTD/Rosette/LADCP stations, 371 XCTDs, and underway ADCP, surface ocean, and meteorological data provide a high resolution view of the SAMW mixed layers and the frontal and eddy structure. The second cruise, in austral summer (January 30 to March 14, 2006), observed the subsequent restratifi-

cation. The summer cruise followed the same track as the winter cruise, occupying 105 CTD/Rosette/LADCP stations and deploying 352 XCTDs.

These near-synoptic surveys are used to assess the role of air-sea fluxes in forming the deep SAMW mixed layers north of the SAF. In this study, we consider SAMW formation as a one-dimensional process, neglecting any advective mechanisms, and focus on how air-sea forcing, initial profile stratification, and mixing determine the SAMW mixed layers' depths, properties, area extent, relationship to the SAF, and downstream variation. In a companion study (Chapter 4) we evaluate how cross-frontal exchange affects SAMW formation in this region.

Section 2 describes the data collected during the two cruises. Section 3 summarizes the 2005 austral winter cruise SAMW mixed layer observations. The cruise heat flux measurements are outlined in section 4 and used to evaluate various model and observation-derived heat flux products in section 5. The flux products are then used to force a one-dimensional mixed layer model to test how air-sea fluxes contribute to the deep mixed layers. The model runs are initialized with profiles from the 2006 austral summer cruise and evolved with the flux products for one year beginning at their collection time. The simulated winter mixed layers, taken as the August mean of each model run, are compared to profiles from the 2005 austral winter cruise and Argo. Section 6 contains the mixed layer modeling results and analysis. Section 7 discusses the results of three model runs with altered NCEP forcing. Section 8 examines the importance of initial profiles in SAMW formation. Section 9 summarizes the results.

3.2   Data

Two hydrographic surveys conducted on R/V Knorr in the southeast Pacific Ocean provide high quality, synoptic observations of the SAMW formation region during winter and summer (Figure 3.1). The first cruise, from August 23 to October 5, 2005, observed the deep winter mixed layers. The second, from January 30 to March 14, 2006, observed the subsequent restratification. Both cruises departed from Punta Arenas, followed a sawtooth path out to 103°W, and concluded near Puerto Montt, crossing the SAF six times. CTD station spacing was approximately 50 km. Each cruise included two diamond-patterned intensive surveys, one in the SAMW region and another at the SAF; the location of these surveys varied by cruise depending on the position of the SAF.
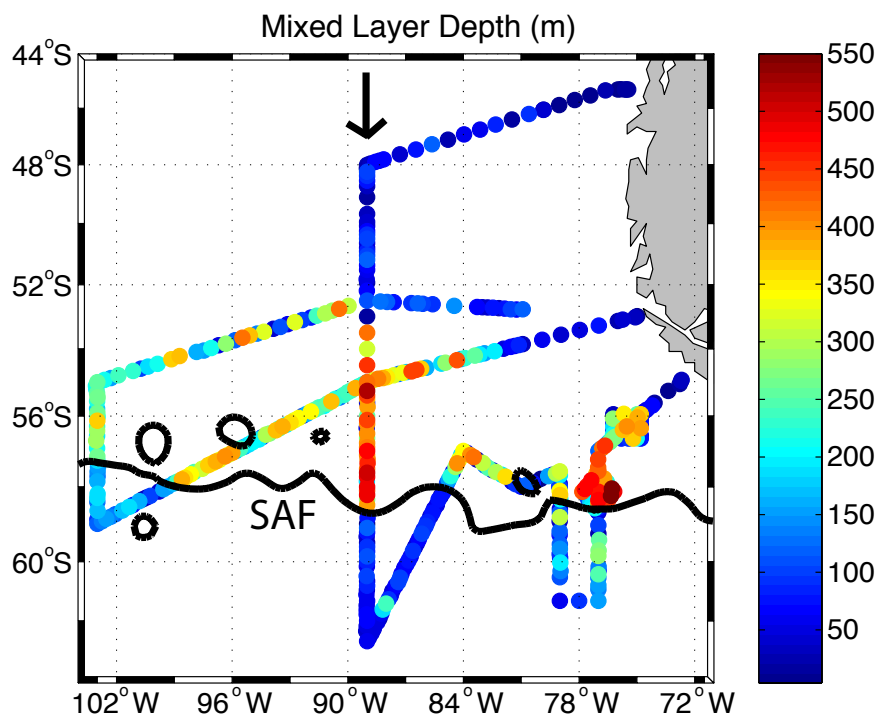
Figure 3.1: Mixed layer depth at CTD and XCTD stations for the 2005 austral winter cruise extend from 0 m (blue) to 550 m (red). The mean AVISO dynamic topography contour that most closely matched the SAF location in hydrography and ADCP data is also plotted (black line). The mean dynamic topography was calculated over the cruise period, August 23 to October 5, 2005. The three sections plotted in Figure 2 were taken along 103°W, 89°W and 77°W.

The 135 CTD/rosette stations from the 2005 austral winter cruise and 105 stations from the 2006 austral summer cruise provided full depth profiles of temperature, salinity, and oxygen in the SAMW and AAIW formation region. Bottle samples (from a 24 bottle rosette in winter and a 36 bottle rosette in summer) were analyzed for dissolved oxygen, salinity, and nutrients. These data were acquired and processed by Scripps Institution of Oceanography's Ocean Data Facility. Carbon parameters and chlorofluorocarbons were also collected during the winter cruise (Hartin et al., 2010).

Intensive XCTD sampling complemented the CTD stations by providing higher vertical and horizontal resolution observations of the mixed layer and frontal and eddy structure, but profiled to only 1100 meters. 371 XCTDs were deployed during the 2005 austral winter cruise and 352 were deployed during the 2006 austral summer cruise. Generally, three XCTDs were deployed by hand launcher from the rear of the ship between CTD stations, resulting in typical XCTD spacing of 15 km. The XCTDs were TSK probes from Sippican. Many XCTDs failed during the 2005 austral winter cruise because of a grounding problem with the ship's data acquisition computer. Scripps Institution of Oceanography provided a data acquisition computer for the 2006 austral summer cruise, and XCTD failure rates were greatly reduced.

A quality control process following Albérola et al. (1996) was implemented to offset XCTD profiles that deviated greatly from neighboring CTD profiles. This method uses a linear regression in θ-salinity space to calculate salinity offsets for XCTDs. It presumes that neighboring CTD and XCTD profiles should have the same θ-salinity relationship at depth; this is not always the case in highly variable frontal regions. Applying the method reduced XCTD salinity variance at depth. XCTDs that greatly differed from nearby CTD stations were discarded. Due to the response of the conductivity sensor, many profiles exhibit spurious salinity values near the surface, usually in the form of unrealistically high salinity tails that gradually blend into the mixed layer. These profiles were trimmed as deeply as necessary to remove the spurious data. Only profiles deeper than 400 m were used in this study. These quality controls reduced the number of available profiles to 303 for the 2005 austral winter cruise and 342 for the 2006 austral summer cruise. To eliminate high frequency noise in the XCTD salinity profiles, the XCTD temperature and salinity profiles were smoothed with a 5 m running-mean filter.

The underway and lowered acoustic Doppler current profiler data sets (SADCP

and LADCP, respectively) are described in Chereskin et al. (2010). The SADCP unit, a RD Instruments 75 kHz Ocean Surveyor, was averaged into 10 m depth bins centered from 50 m to 810 m. The SADCP data was binned into 5 minute average profiles. The LADCP, a 150 kHz RD Instruments Phase 3 broadband ADCP, sampled full depth profiles from 60 m interpolated to a 20 m sampling interval.

Both cruises collected underway temperature, salinity, and dissolved oxygen data, providing a record of the surface layer at very high resolution. Similarly, the Improved METeorological (IMET) sensors mounted on R/V Knorr measured air temperature, wind strength and direction, sea level pressure, shortwave radiation, humidity, and precipitation. The underway and IMET data were reported at 30 second intervals. Latent and sensible heat fluxes were computed by feeding raw IMET data and underway temperature into the COARE bulk algorithm (Fairall et al., 2003). These instantaneous fluxes were averaged into one-hour bins. National Centers for Environmental Prediction (NCEP) Reanalysis 1 longwave fluxes were interpolated to the one-hour bins to calculate net heat fluxes.

Thirteen Argo floats were deployed during the 2005 winter cruise. Argo has continuously sampled the cruise region since 2003, providing greater temporal coverage but reduced horizontal and vertical resolution relative to the cruise. The mixed layer depths and properties from 8703 Argo profiles collected in the cruise region between January 2003 and February 2010 were calculated using the algorithm developed by Holte and Talley (2009). Argo data are available online (Table 3.1).

Remote sensing observations are used to identify the large-scale conditions in the SAMW formation region. QuikSCAT winds provide the overall wind field and show the passage of storms. AMSR-E supplies microwave sea surface temperature (SST) observations. QuikSCAT and AMSR-E provide daily fields with 0.25 degree resolution. AVISO merged satellite topography, available weekly at 0.25 degree resolution, is used to identify eddies, map the geostrophic flow, and determine the relationship of the SAMW mixed layers to the SAF. These products are all available online (Table 3.1).

3.3   Mixed layer observations

Observations from the 2005 austral winter cruise reveal a band of deep mixed layers extending north from the SAF (Figure 3.1). Forty-two profiles with mixed layers deeper than 400 m were observed. The latitudinal extent of the band of deep mixed

Table 3.1: Online data sources.

data source	spatial resolution	temporal resolution	url
Argo	NA	NA	http://www.usgodae.org/argo/argo.html
AMSR-E	0.25°	24 hr	http://www.ssmi.com/sst/microwave_oi_sst_browse.html
QuikSCAT	0.25°	24 hr	http://cersat.ifremer.fr/data/discovery/by_product_type/gridded_products/mwf_quikscat
AVISO	0.25°	168 hr	http://www.aviso.oceanobs.com/index.php?id=1272
NCEP	1.875°	6 hr	http://www.esrl.noaa.gov/psd/data/reanalysis/reanalysis.shtml
ECMWF	1.5°	12 hr	http://data-portal.ecmwf.int/data/d/interim_daily/
J-OFURO	1°	24 hr	http://dtsv.scc.u-tokai.ac.jp/j-ofuro/
OAFlux	1°	24 hr	http://oaflux.whoi.edu/data.html

layers decreases eastward; along 89°W the band's latitudinal extent is 6°, whereas just upstream of Drake Passage the latitudinal extent is 3°. The deepest mixed layers, to 550 m, are found just upstream of Drake Passage. Along the western section at 103°W the MLDs are between 200 and 300 m. The SAMW mixed layers are influenced by the meanders and eddies of the SAF, which forms the southern boundary of the SAMW formation region. The cruise track crossed two cold core eddies in the SAMW formation region at approximately 96°W and 57°S and 80°W and 58°S. These eddies modulated the MLD, decreasing it by more than 200 m compared to the nearby SAMW mixed layers (Figure 3.1). South of the SAF, profiles are characterized by interleaving temperature-salinity layers and decreased mixed layer temperature, salinity, and depth relative to the deep SAMW mixed layers north of the SAF (Figures 3.1 and 3.2). Within this region south of the SAF, several locally unusual deep mixed layers of nearly 300 m were observed along 77°W. At the SAMW formation region's northern boundary, the SAMW was capped by shallower, fresher, and warmer mixed layers.

The vertical and horizontal structure of the SAMW mixed layers in austral winter 2005 is evident in the three long SAF crossings (Figure 3.2). The SAMW is identifiable in each section as a large, uniform mass of water extending north from the SAF. In all sections the deepest SAMW mixed layers occurred immediately north of the SAF, usually within 100 km of the front. In the westernmost section at 103°W, the SAMW had a density range of 26.95 to 27.0 kg m^{-3}. Along 89°W the SAMW had potential densities between 27.0 and 27.02 kg m^{-3}. At the section closest to Drake Passage, along 77°W, the SAMW had potential densities between 27.02 and 27.04 kg m^{-3}. The SAMW in each section was not completely uniform. Along 89°W, the SAMW within 2° of the SAF was approximately 0.4°C colder and 0.05 psu fresher than the SAMW farther north along the same section (Figure 3.2); it also had a lower oxygen fractional saturation.

The SAMW mixed layers are characterized by higher salinities relative to neighboring waters (Figure 3.3). The deep SAMW mixed layers form a cluster in temperature-salinity space and have salinities ranging from approximately 34.075 to 34.2 psu. Outside of the cluster of deep SAMW mixed layers, the mixed layers have lower salinities between approximately 33.95 and 34.075 psu. This pattern persists throughout the year; the highest salinities observed during the 2006 austral summer cruise were found in the SAMW formation region (not shown). The cluster of SAMW is organized spatially into two groups (Figure 3.3). One group is composed of mixed layers from the western por-
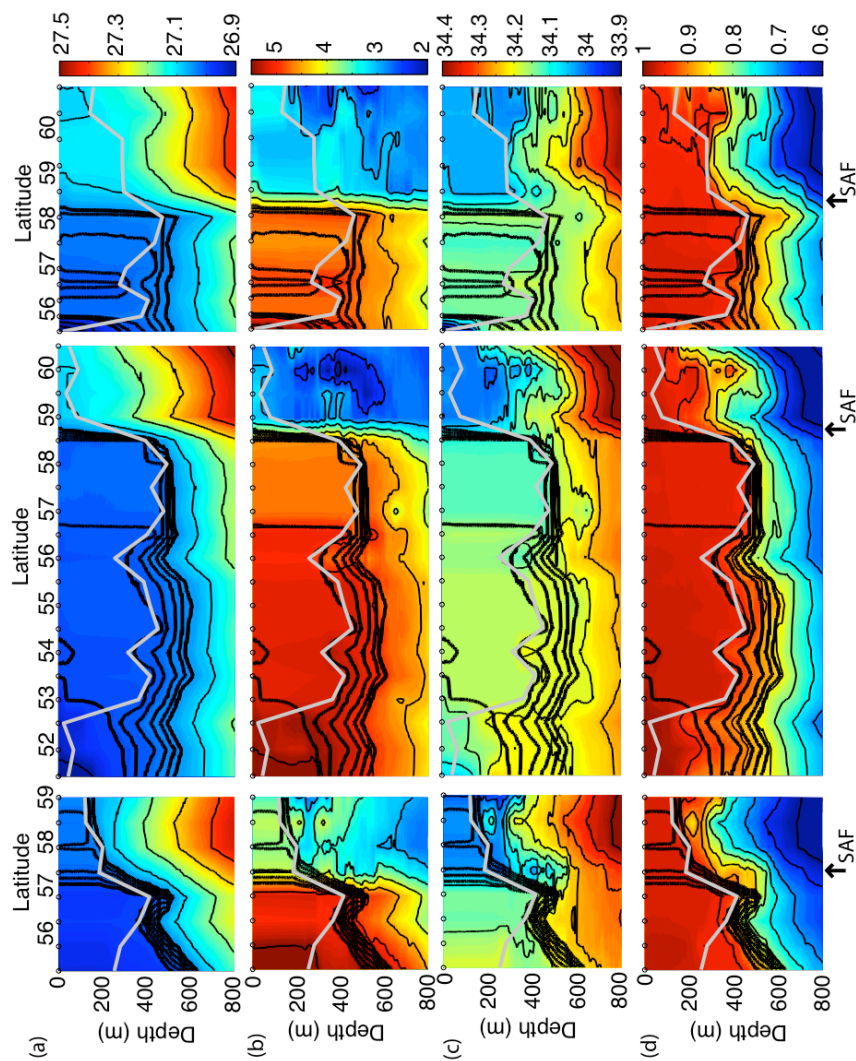
Figure 3.2: Sections of (a) potential density (kg m^{-3}), (b) temperature (°C), (c) salinity (psu), and (d) oxygen fractional saturation along 103°W (left column), 89°W (middle column) and 77°W (right column) from the 2005 austral winter cruise. The CTD profile locations are denoted by circles at the surface. The 27, 27.01, 27.02, 27.03, 27.04, and 27.05 kg m^{-3} isopycnals are contoured by bold black lines. The grey line is the mixed layer depth. For each section, the location of the SAF is identified by a rapid shallowing of isopycnals and is marked by arrows.
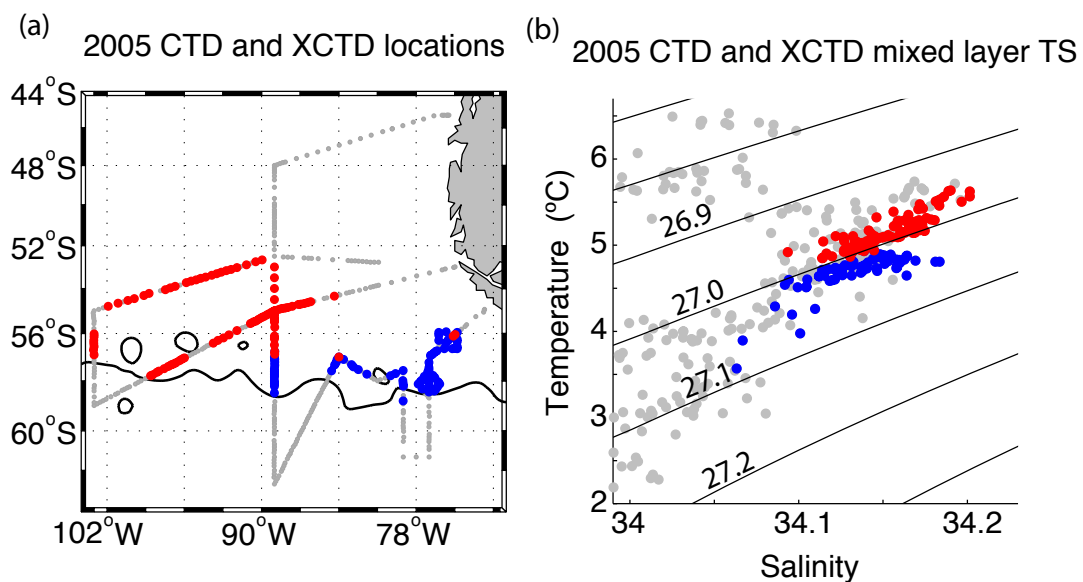
Figure 3.3: The (a) location and (b) temperature-salinity diagram of mixed layers deeper than 200 meters from the 2005 austral winter cruise, using all CTD and XCTD profiles. Mixed layers with densities greater than 27.0 kg m^{-3} are plotted in blue; those with densities less than 27.0 kg m^{-3} are plotted in red. Grey dots denote the remainder of the CTD and XCTD profiles. The geographical distribution of these two mixed layer density classes is shown in (b). Potential density (black lines) is contoured at 0.1 kg m^{-3} intervals.

tion of the cruise with potential densities less than 27.0 kg m^{-3}; the other is composed of mixed layers from the cruise's eastern sections upstream of Drake Passage with potential densities greater than 27.0 kg m^{-3}. In terms of potential density, these spatial groups correspond to an along-front variation in mixed layer potential density of 0.05 kg m^{-3} over a distance of 1500 km. In Argo, this downstream change in SAMW is continuous; the distinct grouping is the result of the cruise spatial sampling.

3.4   Air-sea forcing: cruise observations

In this study, we neglect advective mechanisms and evaluate the extent to which SAMW formation can be considered a one-dimensional process. Taking this simplified view, where SAMW formation is driven by buoyancy loss at the surface and by wind stress, allows us to focus on one aspect of SAMW formation and to examine a number of forcing scenarios. The buoyancy flux has two components, a thermal component due to heat fluxes and a saline component due to evaporation and precipitation. The equation for the buoyancy flux is:

$$B = \frac{g\alpha}{c_p}(Q_{sh} + Q_{lh} + Q_{lw} + Q_{sw}) + gS\beta(P - E) \tag{3.1}$$

where $\alpha = \rho^{-1}\partial\rho/\partial T$ and $\beta = \rho^{-1}\partial\rho/\partial S$ are the thermal and saline expansion coefficients of seawater (which depend on the surface temperature and salinity, T and S), c_p is the specific heat capacity of water, g is the acceleration due to gravity, Q_{sh} is the sensible heat flux, Q_{lh} is the latent heat flux, Q_{lw} is the net longwave radiation, and Q_{sw} is the incoming solar radiation at the sea surface. These heat flux terms determine the thermal component of the air-sea buoyancy flux. During winter, ocean heat loss to the atmosphere, in the form of latent, sensible, and longwave heat fluxes, destabilizes the water column; the surface density increases, resulting in convective overturning. Short-wave heat fluxes stabilize the surface layer. The saline buoyancy component depends on the surface salinity and the difference between precipitation, P, and evaporation, E. Evaporation is calculated as $E = Q_l/L_v$, where L_v is the latent heat of vaporization (Sathiyamoorthy and Moore, 2002). Evaporation increases the surface density, whereas precipitation freshens the surface water, decreasing the density and stabilizing the surface layer. We use the convention that a negative heat flux corresponds to ocean heat and buoyancy loss.

During the 2005 austral winter cruise the regions of oceanic heat loss generally
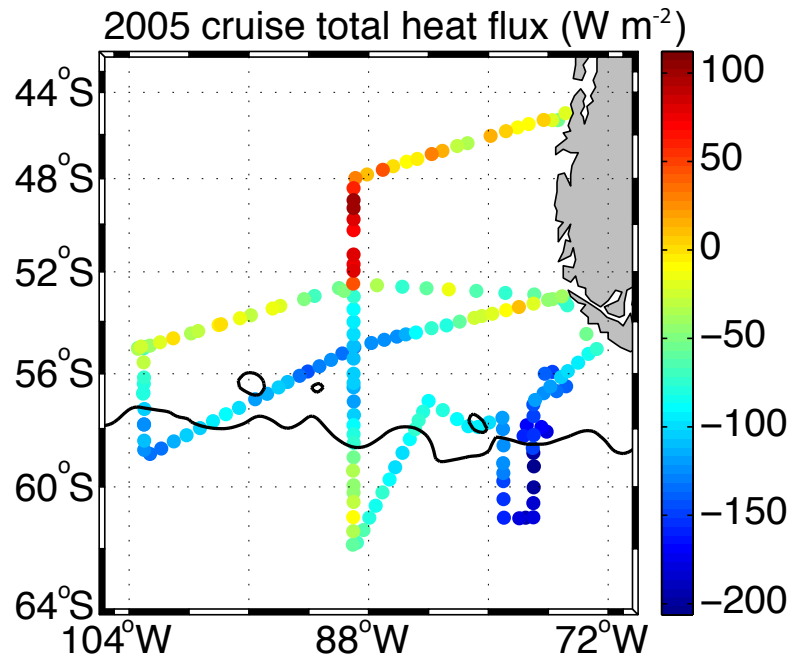
Figure 3.4: Total synoptic heat fluxes along the 2005 cruise track ranged from 100 W m^{-2} (red, ocean heat gain) to -200 W m^{-2} (blue, ocean heat loss). The instantaneous latent and sensible heat fluxes were calculated using the COARE algorithm from cruise IMET data. Shortwave fluxes were measured by the IMET system. Longwave fluxes are from NCEP reanalysis. The fluxes are six-hour averages smoothed with a 2 day running mean to soften daily peaks in the shortwave radiation and plotted every six hours. The mean AVISO dynamic topography contour that most closely matched the SAF location in hydrography and ADCP data is also plotted (black line).
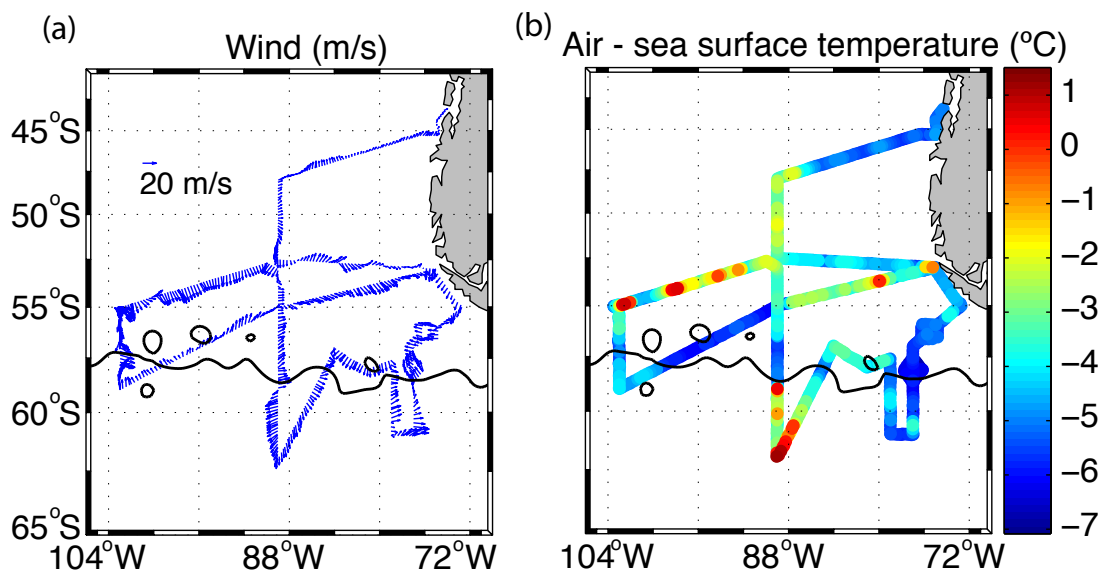
Figure 3.5: Maps of (a) vector wind (m/s) and (b) air-sea temperature difference (°C) along the 2005 cruise track. The mean AVISO dynamic topography contour that most closely matched the SAF location in hydrography and ADCP data is also plotted (black line).

corresponded to regions with deep SAMW mixed layers (Figures 3.1 and 3.4). The largest heat fluxes, nearly -200 W m^{-2}, were observed along 77°W. These fluxes are small compared to the fluxes of nearly -1000 W m^{-2} that are associated with the formation of Subtropical Mode Waters near the Gulf Stream and Kuroshio (Joyce et al., 2009). Large fluxes were also observed north of the SAF along 89°W and between 96°W and 83°W. This suggests that active mixing was occurring during the survey (Sloyan et al., 2010). In the northern and northwestern sectors of the cruise the heat flux is small, and at times positive; deep SAMW mixed layers were observed sporadically in these regions.

The large heat fluxes that contribute to SAMW formation are caused by winds from the south. The winds recorded during the 2005 cruise exhibit considerable variation in direction and magnitude (Figure 3.5), reflecting the many synoptic storms that passed through the SAMW formation region during the cruise; the predominant wind directions are southwesterly and northwesterly. The SAMW formation region is remote from any upstream continental land masses that could produce extreme cold air outbreaks, so the cold polar waters south of the SAF serve as the largest atmospheric heat sink in the region. Winds from the south originate over this relatively cold region, and when
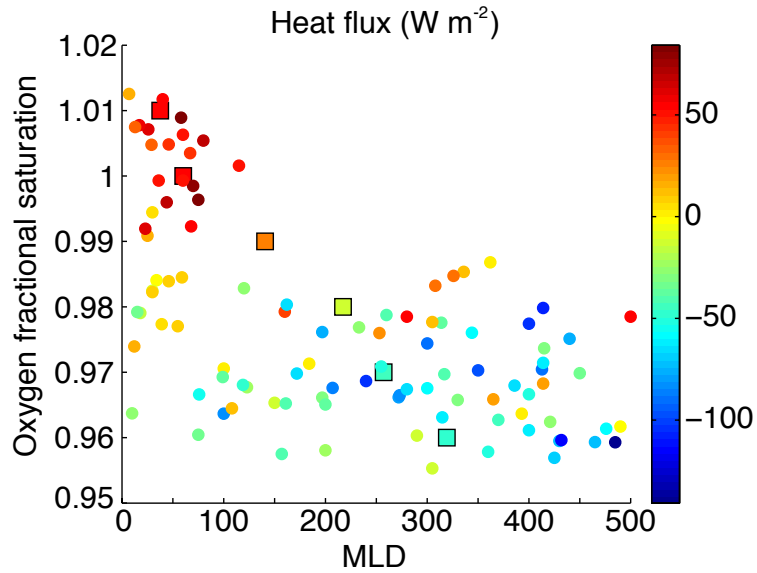
Figure 3.6: Comparison of mixed layer oxygen saturation and MLD for CTD profiles north of the SAF (colored circles). The color corresponds to total synoptic heat flux. The mean heat flux and mean mixed layer depth are calculated for mixed layer oxygen saturation bins centered at 0.96, 0.97, 0.98, 0.99, 1, and, 1.01 (colored squares).

they blow north across the SAF, they encounter warmer water. This creates the air-sea temperature difference that produces large sensible and latent heat fluxes over the SAMW formation region (Figure 3.5).

These heat fluxes contributed to active mixing in the SAMW formation region. The deepest mixed layers tended to have fractional oxygen saturations of 0.96 and corresponded to the largest synoptic heat fluxes at the surface (Figure 3.6). These low fractional oxygen saturations are typical signatures of active mixed layer deepening; as the mixed layer deepens it entrains water at its base that has a lower oxygen fractional saturation, lowering the fractional oxygen saturation of the entire mixed layer. Similarly, low saturations of chlorofluorocarbons were observed in the deep mixed layers on the 2005 austral winter cruise for the same reason (Hartin et al., 2010). The mixed layers with the most vertically uniform oxygen saturations were located immediately near the SAF (Figure 3.2). Away from the front the mixed layer fractional oxygen saturation has a slight vertical gradient, increasing toward the surface. The oxygen distributions suggest that the mixing was most active near the front.

3.5   Air-sea forcing: product comparisons

The cruise IMET heat fluxes described in section 2 are compared to various reanalysis and observation-derived heat flux products. We use fields from NCEP Reanalysis 1 (Kalnay et al., 1996), European Centre for Medium-Range Weather Forecasts (ECMWF) Interim, Japanese Ocean Flux Data sets with Use of Remote Sensing Observations (J-OFURO), Kelly, OAFlux, and the Southern Ocean State Estimate (SOSE). The heat flux products provided by NCEP, ECMWF, J-OFURO, and OAFlux are available online (Table 3.1). The reanalysis products, NCEP and ECMWF, provide flux fields four times and two times daily, respectively; the other products are available once daily. J-OFURO, Kelly, and OAFlux are mostly derived from direct observations. J-OFURO primarily incorporates remote sensing data. The Kelly latent and sensible heat fluxes are computed by Kathryn A. Kelly's group at the University of Washington with the COARE v3.0 algorithm, using QuikSCAT wind speed maps, the NOAA OISST sea surface temperature product (www.ncdc.noaa.gov/oa/climate/research/sst/oi-daily.php), and ECMWF analyses for the remainder of the input variables. Kelly fluxes have 0.5° resolution. OAFluxes are derived from satellite observations, surface observations, and a reanalyzed atmospheric model (Yu et al., 2008). SOSE synthesizes NCEP fluxes and a wide variety of observations in an eddy-permitting model; it outputs, among many other fields, modified NCEP fluxes that are consistent with the in situ observations (Mazloff et al., 2009). Products missing any of the four heat flux terms, wind stress, or precipitation are supplemented with the NCEP fields (Table 3.2).

In general, most of the products' total heat fluxes track the total heat fluxes observed during the 2005 and 2006 cruises fairly well, capturing the high and low heat flux events from both cruises (Figure 3.7) [comparison for the 2006 cruise not shown]. NCEP, ECMWF, and Kelly fluxes most closely match the cruise fluxes, particularly for the 2005 austral winter cruise. All of the heat flux products deviate more from the 2006 austral summer cruise fluxes than they do from the 2005 austral winter cruise fluxes (Table 3.3). J-OFURO and SOSE have the poorest fits to the cruise observations and produce many spurious heat flux events, though SOSE's mean fluxes are similar to the cruise mean. J-OFURO has the largest root mean square differences from the cruise fluxes. OAFlux is biased more than 30 W m^{-2} higher (less ocean heat loss) than the cruise fluxes.

The latent and sensible heat fluxes have roughly the same magnitudes as each

Table 3.2: Forcing fields provided by each flux product. NCEP is used as the default for any missing forcing terms.

Product	Latent	Sensible	Longwave	Shortwave	Momentum	Precipitation
NCEP	NCEP	NCEP	NCEP	NCEP	NCEP	NCEP
ECMWF	ECMWF	ECMWF	ECMWF	ECMWF	ECMWF	ECMWF
Kelly	Kelly	Kelly	NCEP	NCEP	NCEP	NCEP
J-OFURO	J-OFURO	J-OFURO	J-OFURO	J-OFURO	J-OFURO	NCEP
OAFlux	OAFlux	OAFlux	OAFlux	OAFlux	NCEP	NCEP
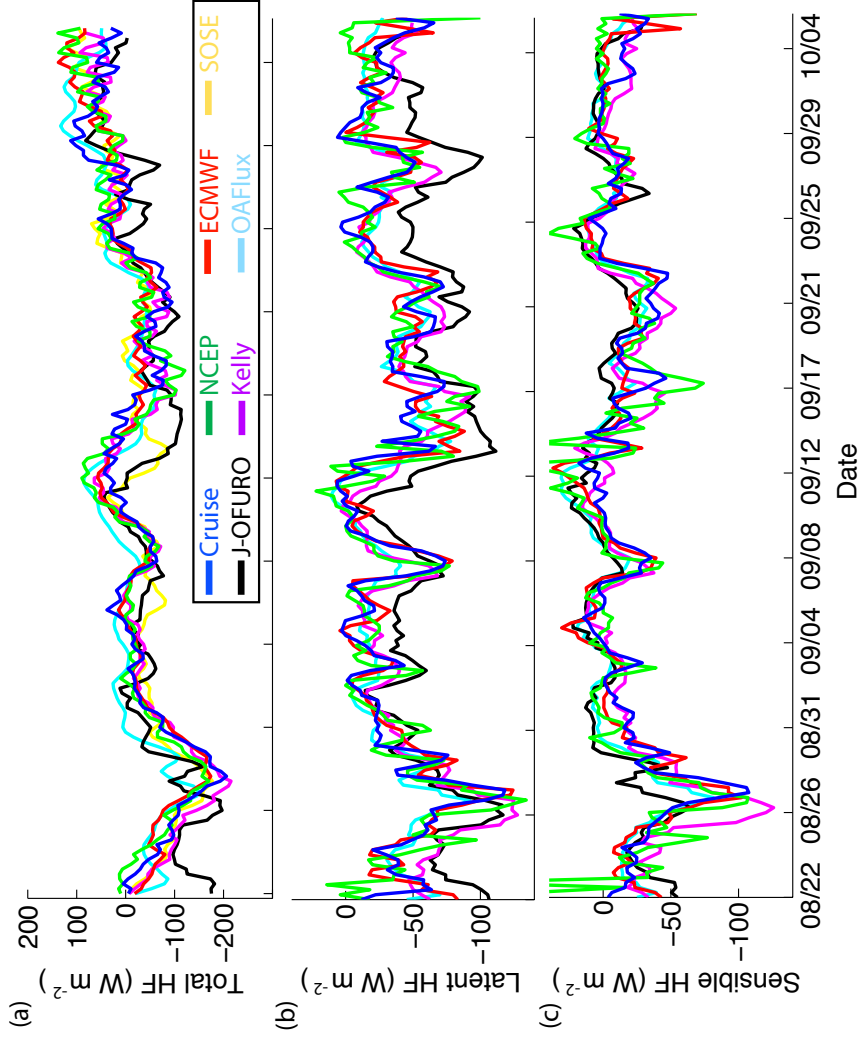
Figure 3.7: Along track values of synoptic (a) total heat flux, (b) sensible heat flux, and (c) latent heat flux for the 2005 winter cruise for: cruise IMET fluxes (blue), NCEP reanalysis (green), ECMWF (red), SOSE (yellow), OAFluxes (cyan), Kelly fluxes (magenta), and Ofuro (black). The cruise IMET latent and sensible heat fluxes are calculated with the COARE algorithm. The cruise total heat flux uses measured IMET shortwave fluxes and NCEP reanalysis for longwave fluxes. The cruise fluxes are six-hour averages smoothed with a 2 day running mean. The flux products are also smoothed with a 2 day running mean.

Table 3.3: Means and root-mean-square differences of along track total heat flux and sensible and latent heat fluxes from the two cruises compared to the various flux products. The flux products are interpolated to the cruise locations and times. The root-mean-square differences are calculated as the difference between the cruise heat flux and the various products' heat fluxes.

Mean	Cruise	NCEP	ECMWF	SOSE	Kelly	J-OFURO	OAFlux
2005 total heat flux	-41	-33	-33	-43	-47	-56	-13
2005 latent+sensible	-52	-52	-51	NA	-65	-63	-40
2006 total heat flux	40	63	61	45	69	51	81
2006 latent+sensible	-51	-47	-43	NA	-39	-40	-31
Root-mean-square differences	Cruise	NCEP	ECMWF	SOSE	Kelly	J-OFURO	OAFlux
2005 total heat flux		30	19	43	27	53	38
2005 latent+sensible		36	20	NA	38	33	24
2006 total heat flux		48	39	46	43	68	43
2006 latent+sensible		46	37	NA	35	36	30
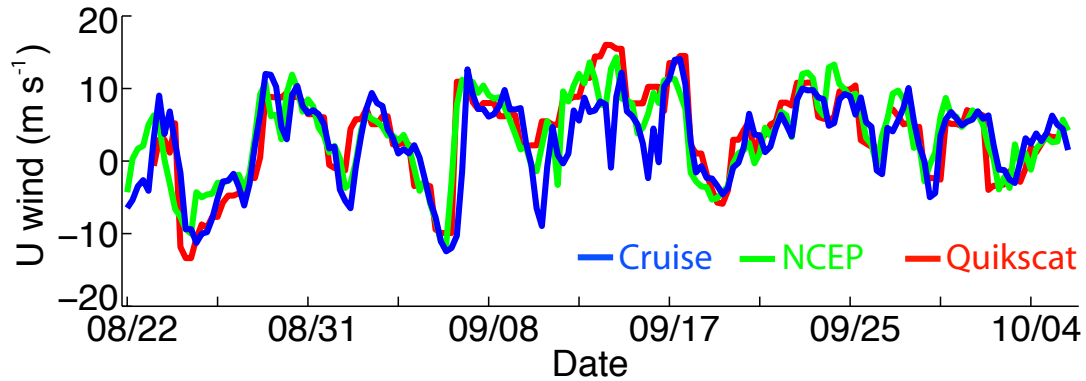
Figure 3.8: Along track wind from the 2005 cruise compared to NCEP and Quikscat winds.

other (Figure 3.7). Surprisingly, the sum of the latent and sensible heat fluxes is the same for both the austral winter and summer cruises (Table 3.3). The northward wind mechanism that produces the enhanced ocean heat fluxes during the winter cruise also works in summer, even though the temperature gradient across the SAF is reduced in summer. During summer the shortwave heat flux component overwhelms the latent and sensible heat fluxes, so the net heat flux is positive.

Besides heat fluxes, air-sea fluxes of momentum and precipitation are also important to SAMW formation. NCEP and QuikSCAT closely track the wind measurements from the 2005 winter cruise (Figure 3.8). NCEP captures the large synoptic storms, on the scale of 5 days, and also shorter scale fluctuations. In the one-dimensional model runs, NCEP wind stress is used as the default wind stress for the flux products that do not provide wind fields (e.g. Kelly and OAFlux). Accurate precipitation measurements are difficult to obtain at sea, especially in high-wind conditions (Yuter and Parker, 2001). ECMWF and NCEP are the only products that provide precipitation. Rather than compare the products' precipitation fields to the cruise measurements, we use our mixed layer modeling results to evaluate the precipitation fields.

3.6 One-dimensional mixed layer modeling with observed forcing

A one-dimensional mixed layer model is used to assess the role of buoyancy forcing and wind mixing in forming deep winter SAMW mixed layers from stratified summer

profiles. Five sets of runs are evolved in the model, each with different sources for the heat, precipitation, and momentum fluxes; the NCEP, ECMWF, Kelly, J-OFURO, and OAFlux forcing fields used in each set of runs are outlined in Table 3.2. Each set of the five model runs is initialized with 100 CTD profiles from the 2006 austral summer cruise. The fluxes are interpolated to each profile location, commence on each profile's collection date, and evolve the profiles for one year. To allow comparison with the 2005 cruise observations and with winter Argo profiles collected in the cruise region, a representative simulated winter mixed layer is calculated at each CTD station as the temporal mean of each model run during the month of August, producing 100 simulated winter mixed layers for each flux product. August was chosen for calculating the mean because the maximum mean Argo MLD occurs in August and the heat flux becomes positive after August. Averaging the simulations over longer winter periods does not substantially alter the results.

We use a simple configuration of the Regional Ocean Modeling System (ROMS) for our one-dimensional mixed layer model (available at: http://www.myroms.org/). The model is initialized with 250 depth levels and a profile depth of 2000 m. The profiles are evolved for one year with a time step of 60 seconds; the fluxes are interpolated to match this time step. ROMS has many possible configurations. We tested 20 different configurations, using different combinations of the KPP mixing scheme of Large et al. (1994), the Kantha and Clayson (1994) stability function, and the Mellor and Yamada (1982) level 2.5 closure scheme, as well as various numerical modules in ROMS, such as the tracer advection schemes. To test the model set-up, each configuration was run for three different initial CTD profiles from the 2006 austral summer cruise: two in the SAMW formation region (station 143 at 76°W and 56.5°S and station 147 at 77°W and 58°S) and one south of the SAF (station 154 at 77°W and 61.5°S). The three profiles were evolved for one year with NCEP forcing corresponding to the CTD locations. Most of the 20 configurations produced remarkably similar winter SAMW mixed layer depths and properties; for each initial profile the configurations' maximum winter MLDs differ by less than 80 m. The chosen configuration is essentially the KPP mixed layer model, which includes diffusive mixing due to shear instability, convective mixing due to shear instability, double-diffusive mixing, with non-local transport activated. Our set-up differs slightly from the standard configuration; we use splines vertical advection because of the high vertical resolution of our simulation. We also conducted test runs with the Price-

Weller-Pinkel mixed layer model (Price et al., 1986), but its simulated SAMW mixed layers were unrealistically shallow.

In terms of MLD, the five forcing products all produce some sort of SAMW, in that they all produce deep mixed layers in the region where SAMW was observed during the 2005 austral winter cruise (Figure 3.9). They all correctly reproduce the band of deep SAMW mixed layers north of the SAF. The band of MLDs is wider to the west, and the mixed layers generally deepen to the east. This mirrors the 2005 austral winter cruise MLDs and the range of Argo MLDs. In the Argo data, which span several winters from 2003 to 2009, the band of deep winter SAMW mixed layers narrows near Drake Passage and has largely the same areal extent as the SAMW observed during the 2005 austral winter cruise. Argo features more numerous and deeper SAMW mixed layers in the cruise's western section. Argo recorded 10 MLDs deeper than 600 m, whereas the deepest MLDS observed during the 2005 austral winter cruise reached 550 m. All of the forcing products except for OAFlux tend to produce deeper SAMW MLDs than were observed during the cruise. NCEP and Kelly produce very similar MLDs to each other because the Kelly model runs use NCEP longwave, shortwave, precipitation, and wind stress fields (Table 3.2).

The observed and simulated SAMW mixed layers differ in a number of ways. ECMWF and J-OFURO produce few deep SAMW MLDs in the cruise's western sections, as does OAFlux. OAFlux produces shallower MLDs throughout the SAMW formation region. It only produces MLDs to depths of approximately 400 m in a very thin band just north of the SAF. ECMWF, J-OFURO, and OAFlux produce more accurate MLDs south of the SAF, whereas NCEP and Kelly's MLDs south of the SAF are more than 100 m deeper than the MLDs observed on the 2005 austral winter cruise. Argo has recorded MLDs to 350 m south of the SAF, so the MLDs produced by NCEP and Kelly are possible.

The temperature-salinity characteristics of the simulated SAMW mixed layers generally match the Argo observations (Figure 3.10). The J-OFURO, NCEP, and Kelly mixed layers overlap the Argo SAMW more than the ECMWF and OAFlux mixed layers. The SAMW mixed layers produced by ECMWF and OAFlux are too fresh; neither product produces simulated SAMW mixed layers with salinities greater than 34.15 psu. None of the simulated SAMWs capture the full range of the Argo SAMW salinities, and in general they tend to reproduce the fresher SAMWs in the cruise region.
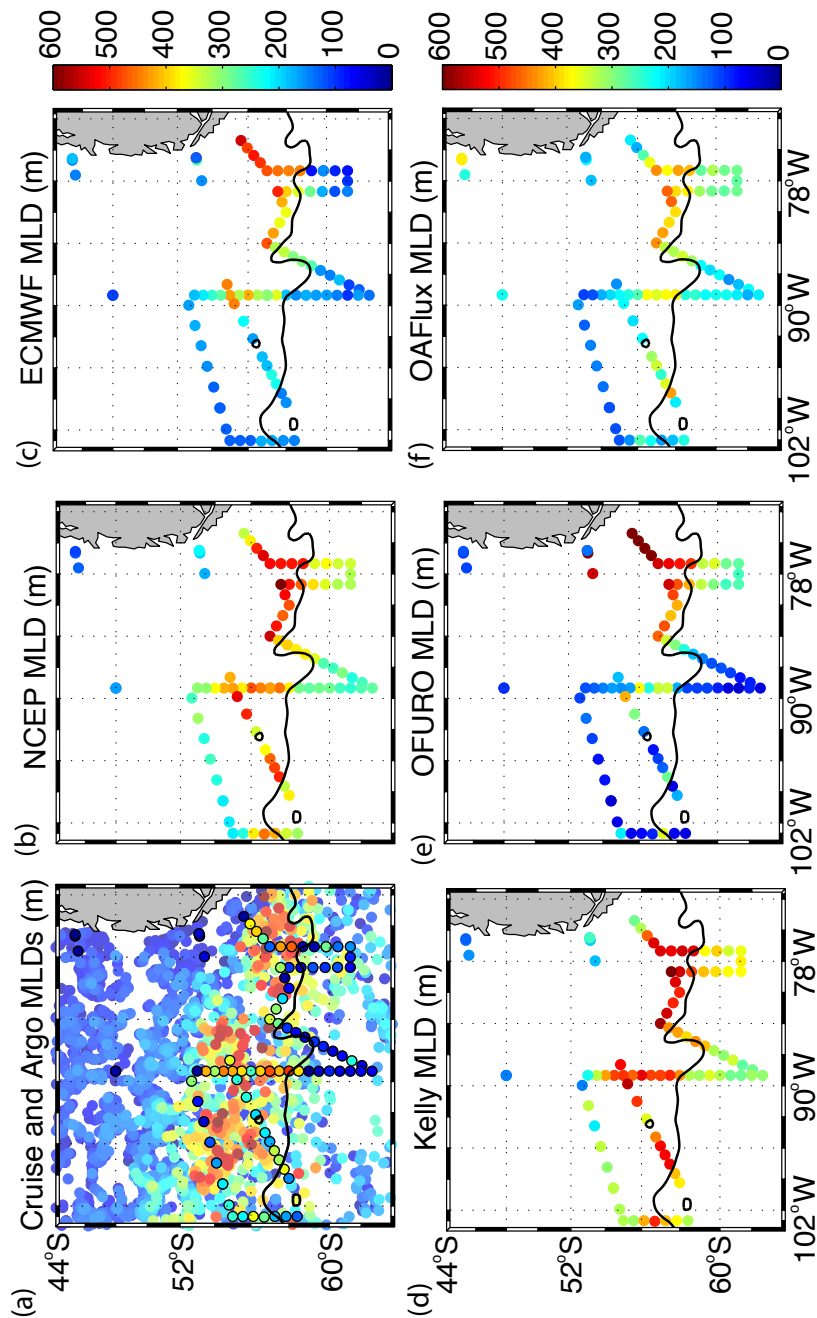
Figure 3.9: MLDs from (a) Argo and (b-f) simulated winter MLDs from ROMS runs initialized with 2006 summer cruise profiles. The simulated runs are forced with (b) NCEP, (c) ECMWF, (d) Kelly, (e) OFURO, and (f) OAFluxes. The MLDs range from 0 meters (blue) to 600 meters (red). In (a), the cruise CTD MLDs are plotted as colored circles with black borders. 2597 winter Argo profiles (collected between July and October from 2003 to 2010) are plotted as colored circles with no borders. The mean AVISO dynamic topography contour that most closely matched the SAF location in hydrography and ADCP data during the 2006 cruise is also plotted (black line). The mean dynamic topography was calculated over the 2006 cruise period.
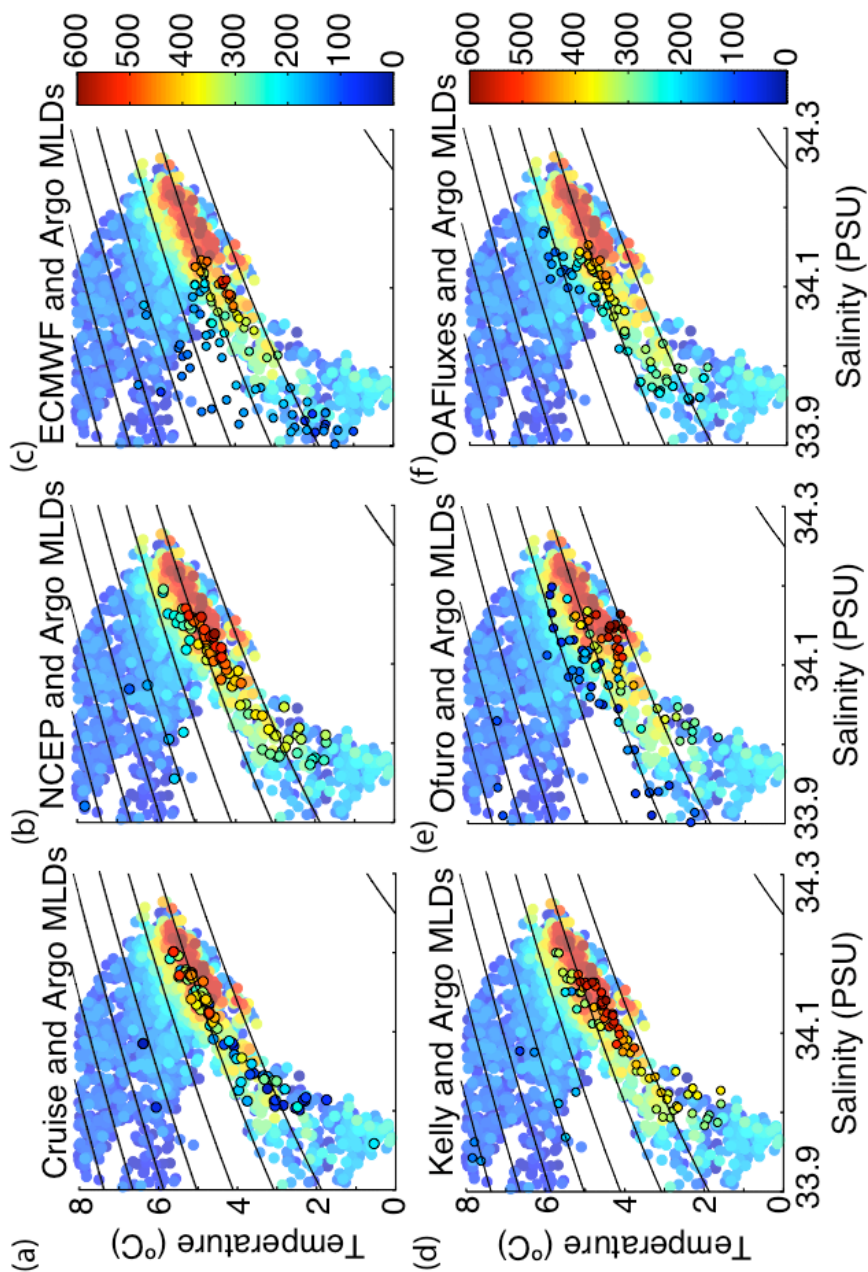
Figure 3.10: Temperature-salinity diagrams from (a) 2005 cruise and (b-f) simulated winter MLDs from ROMS runs initialized with 2006 summer cruise profiles. The simulated runs are forced with (b) NCEP, (c) ECMWF, (d), Kelly, (e) OFURO, and (f) OAFluxes. The cruise and simulated mixed layers are plotted in colored circles with black borders. The mixed layers from 2597 winter Argo profiles (collected between July and October from 2003 to 2010) in the cruise region are plotted as colored circles. The MLDs range from 0 meters (blue) to 600 meters (red). The potential density is contoured at 0.1 kg m^{-3} intervals from 26.5 to 27.1 kg m^{-3}.

The cruise SAMW mixed layers do not have as wide a range of salinities as the Argo SAMW mixed layers.

Figure 3.11 shows a time series of simulated MLDs and forcing fields for three regions from the cruise. The simulated MLDs generally fall within the range of Argo observations. The deepest Argo SAMW MLDs occur in August, whereas the model runs have much longer periods of deep MLDs, most likely because the model restratifies poorly. The deepening in the simulated eastern profiles seems to correspond to a peak in the wind stress forcing in May. By the end of winter the cumulative forcing fluxes for the three groups of profiles are largely the same.

Examining the mean forcing fields for the period from February to September, 2006, illuminates some of these differences in the simulated SAMW mixed layers. This period runs approximately from each profile's collection date during the 2006 austral summer cruise to the following winter.

For heat flux, the NCEP, ECMWF, Kelly, and J-OFURO mean fields are quite similar in the SAMW formation region. The NCEP and ECMWF fluxes in Figure 3.11 (a) are representative of these fields. There is little zonal variation in heat flux in both NCEP and ECMWF, though the fluxes are slightly stronger in the cruise's southeast section, where the deeper MLDs were simulated. J-OFURO features a stronger zonal gradient, with the strongest negative fluxes closer to Chile; these strong fluxes produce unrealistically deep MLDs near Chile (Figure 3.9 (e)). The shallower MLDs produced in the northwestern cruise sections by all of the flux products are due to lower heat loss in these sections. OAFlux produces shallower SAMW MLDs throughout the SAMW formation region because its mean February to September heat fluxes are more than 10 W m^{-2} less negative than the other products. Because the OAFlux mixed layers are shallow, they do not entrain the saltier water beneath, and the mixed layers are too fresh (Figure 3.10 (f)).

The evaporation minus precipitation fields for NCEP and ECMWF are very different (Figure 3.11 (b)). ECMWF's precipitation is much stronger than the precipitation in NCEP. ECMWF's precipitation overwhelms the heat flux in the cruise's western sections, overpowering the heat flux and suppressing mixing. This produces shallow MLDs in the west that are too fresh.

The entire SAMW formation region is characterized by elevated annual mean wind stress relative to regions to the north and south. There is little longitudinal vari-
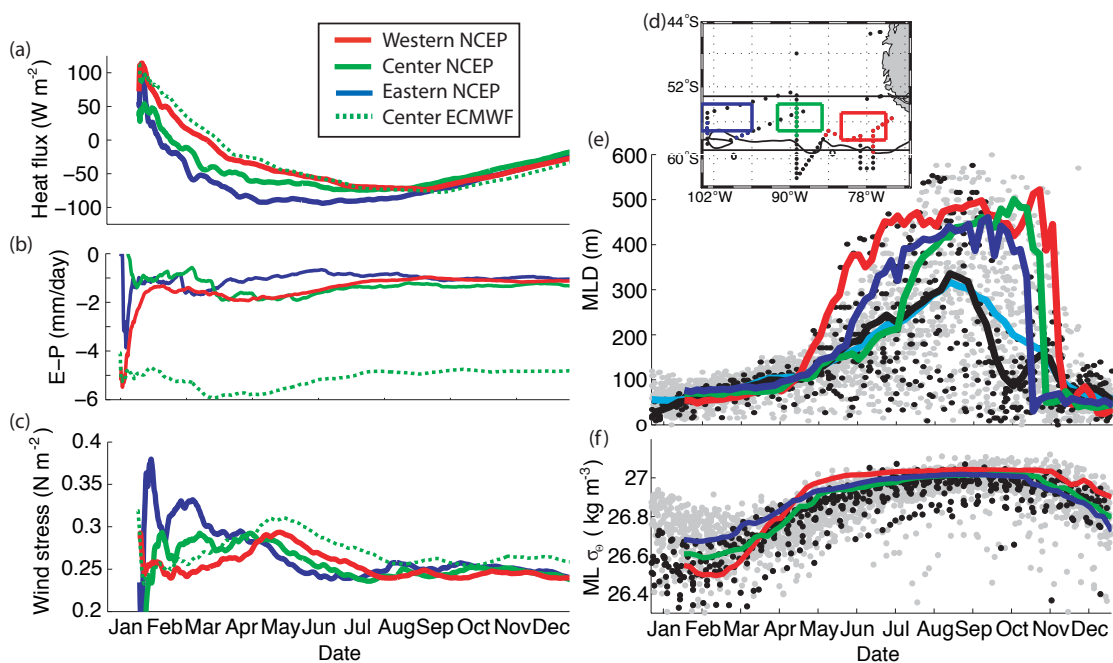
Figure 3.11: Spatial-mean cumulative (a) heat flux, (b) evaporation minus precipitation, (c) wind stress, and mean (e) MLD and (f) mixed layer potential density. The mean cumulative air-sea fluxes in (a-c) were calculated from 2006 NCEP fields (colored lines, corresponding to colored boxes in (d)) and 2006 ECMWF fields (black line, corresponding to red box in (d)). The CTD stations (dots) sampled on both cruises are plotted in (d); the highlighted groups of blue, green, and red CTD stations are used to calculate the mean mixed layer properties in (e) and (f). The mean AVISO dynamic topography contour that most closely matched the SAF location in hydrography and ADCP data is also plotted (black line). In (e) and (f), the mean simulated mixed layer depths and potential densities for the groups of CTD stations are plotted, as well as the Argo values (grey dots) for all profiles collected within the black box in (d). The black dots denote Argo from 2006. In (e), the mean Argo MLD for all years is the cyan line; the mean Argo MLD for 2006 is the black line.
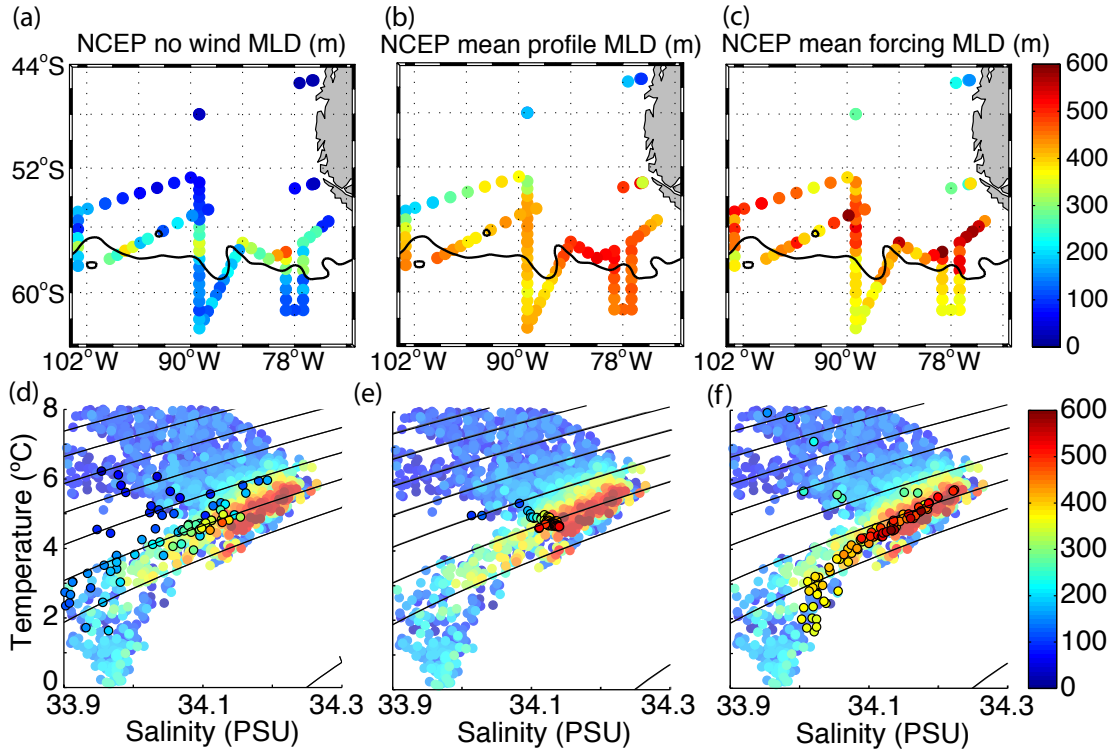
Figure 3.12: MLD maps and temperature-salinity diagrams of simulated winters for three alternative configurations of ROMS run with NCEP forcing: (a,d) no wind, (b,e) mean initial profile (but different forcing), and (c,f) mean forcing (but different initial profiles). The mean profile in (b,e) is derived from seven profiles north of the SAF along 89°W (green profiles in Figure 3.15). In (c,f), the forcing is the mean NCEP forcing in the box spanning 54 to 56°S and 90 to 94°W. In (d), (e), and (f) the simulated winter mixed layers are denoted by circles with black borders. The mixed layers from winter Argo profiles are denoted by circles with no borders. The potential density is contoured at 0.1 kg m^{-3} intervals from 26.5 to 27.1 kg m^{-3}.

ation in wind stress in the SAMW formation region (Figure 3.11 (c)), though all of the fields represent slightly stronger wind stresses in the west. The elevated wind stress in the SAMW formation region most likely helps drive mixing, as was shown in Sloyan et al. (2010). J-OFURO has weaker wind stress than NCEP and ECMWF, resulting in decreased mixing, and hence shallower and fresher MLDs.

3.7 One-dimensional mixed layer modeling with idealized forcing

To further test the importance of mixing driven by heat fluxes and wind stress, we run a series of three test cases with NCEP forcing: (1) with NCEP heat fluxes and precipitation but without wind stress, (2) with standard NCEP forcing but replacing the initial profiles with a mean profile from the SAMW formation region, and (3) with initial profiles from the 2006 austral summer cruise but forced by spatial-mean NCEP fields from the SAMW formation region (Figure 3.12). We use NCEP forcing because it has similar heat fluxes to Kelly and ECMWF, but its evaporation minus precipitation fields allow it to produce SAMW that more closely resembles Argo SAMW observations than ECMWF (Figure 3.10).

In run 1, when driven only with heat fluxes and no direct wind stress, the model poorly reproduces SAMW; it only produces a few shallow SAMW mixed layers in a thin band along the SAF. From this we conclude that wind-driven mixing is essential for forming SAMW mixed layers, at least to the extent that SAMW formation can be explained by one-dimensional mixed layer processes.

Run 2 is initialized with a mean profile. The mean profile is calculated by averaging seven 2006 austral summer CTD profiles collected in the SAMW formation region at CTD depths levels; the profiles are highlighted in green in Figure 3.11 (d). This run illuminates the effect of variable forcing on SAMW. In the cruise's northwestern section, where the NCEP heat flux is smaller, the simulated SAMW mixed layers are shallower than for the cruise's eastern section, where the heat flux is larger. An annual mean heat flux difference of approximately -30 W m^{-2} results in winter SAMW MLDs that differ by 200 m. The western SAMW MLDs in this test case are deeper than the MLDs in Figure 3.9 (b). This test run fails to capture any of the SAMW property variability observed by Argo, as the simulated SAMW properties are all clustered around the initial profile's temperature-salinity properties (Figure 3.12 (e)). The variable forcing is not strong enough to replicate the observed range of SAMW properties. Therefore the initial profile, and any preconditioning processes, are important in determining the final SAMW mixed layer depths and properties.

Likewise, in run 3 we apply mean forcing to all of the actual profiles and the SAMW formation is much more extensive, especially in the cruise's western sections (Figure 3.12 (c)). The mean forcing is calculated as the spatial average of the NCEP fields
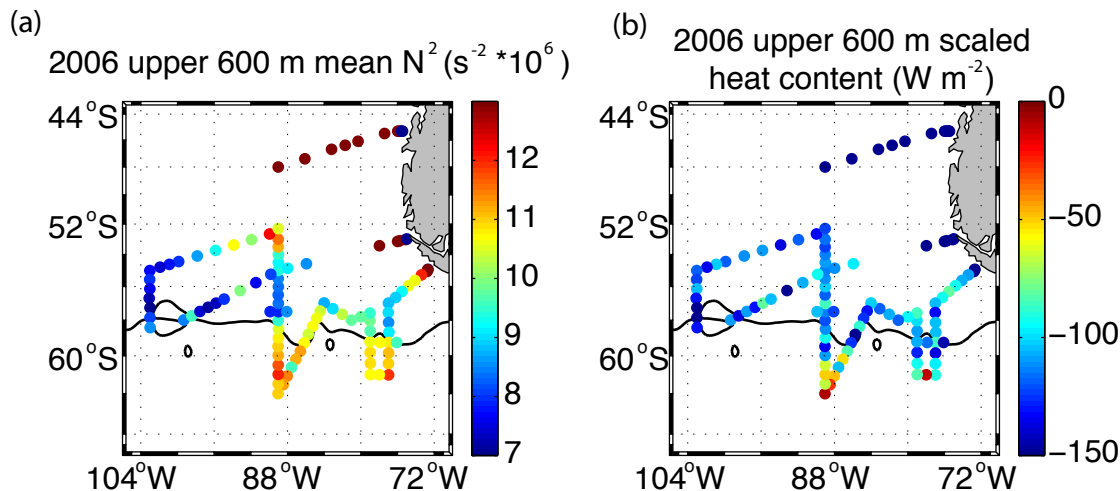
Figure 3.13: Maps of (a) average N^2 and (b) scaled heat content of the upper 600 m for the 2006 austral summer cruise CTD profiles. The heat content is scaled to represent the average heat flux that would homogenize the profile to a depth of 600 m over 200 days. The mean AVISO dynamic topography contour that most closely matched the SAF location in hydrography and ADCP data is also plotted (black line).

in the box spanning 54°S to 56°S and 90°W to 94°W. With this forcing, the simulated SAMW mirrors the full range of SAMW temperature-salinity properties as observed by Argo (Figure 3.12 (f)). Applying mean forcing essentially strengthens the forcing in the cruise's western sections, deepening those mixed layers and filling out the temperature-salinity characteristics of the SAMW. In this way, forcing strength indirectly determines the winter SAMW properties by controlling where and how deeply the profiles mix.

3.8   Importance of preconditioning to SAMW formation

The above analysis shows that air-sea fluxes are important for deepening the SAMW mixed layers. We now look at how the initial summer profile both determines the temperature-salinity characteristics of the final winter SAMW and can also limit the extent of the deepening.

The 2006 austral summer cruise profiles in the SAMW formation region were characterized by low mean stratification in the upper 600 m, generally less than $1\text{x}10^{-5}$ s^{-2} (Figure 3.13 (a)). The lowest stratifications were found in the western section of the cruise, which was slightly unexpected, given that the deepest winter mixed layers
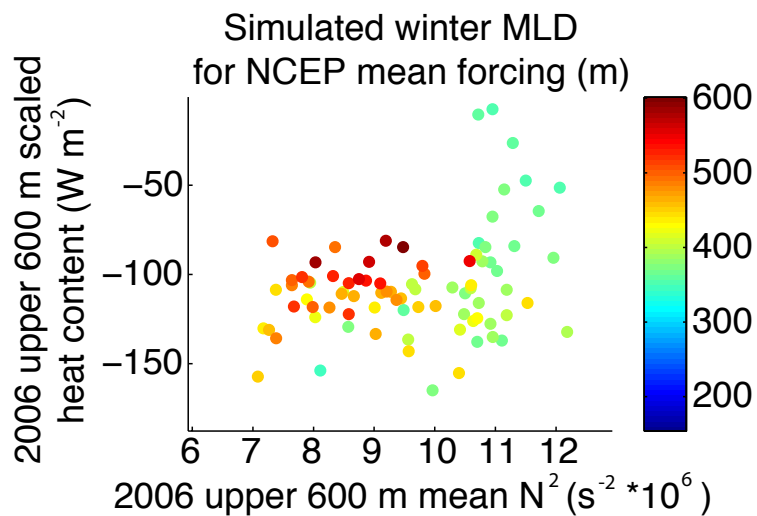
Figure 3.14: Relationship between mean stratification and heat content in the upper 600 m for CTD profiles from the 2006 austral summer cruise. The heat content is scaled to represent the average heat flux that would homogenize the profile to a depth of 600 m over 200 days. The color corresponds to the simulated August (winter) MLD for the mixed layer model run with NCEP spatial-mean forcing applied to all profiles (described in Section 7). The forcing spatial mean is taken over a box spanning 54°S to 56°S and 90°W to 94°W.
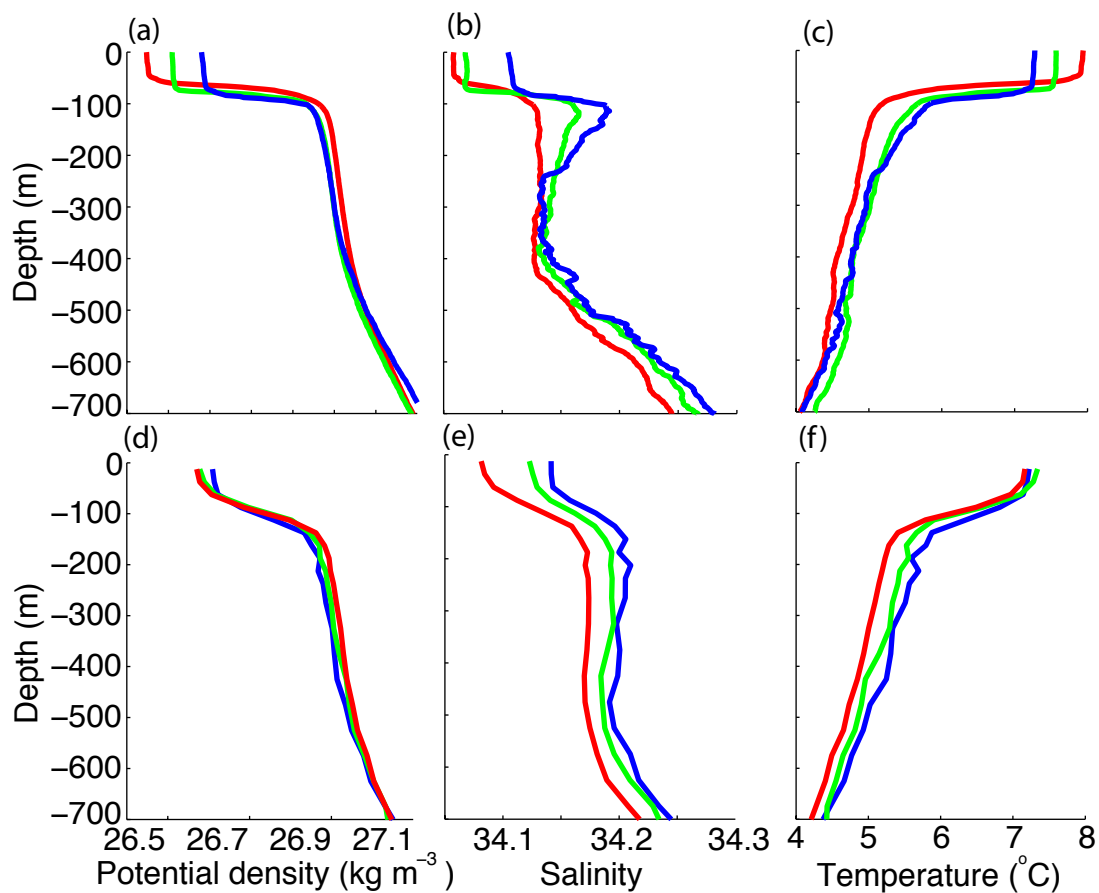
Figure 3.15: Mean (a) potential density, (b) salinity, and (c) temperature profiles for the three groups of CTD profiles from the 2006 austral summer cruise highlighted in Figure 3.11 (a). The red profile is composed of profiles from cruise's eastern sector, near 78°W, green represents profiles collected along 89°W, and blue composed of profiles from the west, near 103°W. These profiles all formed deep simulated SAMW winter mixed layers in the NCEP ROMS run. Similar mean Argo profiles of mean (d) potential density, (e) salinity, and (f) temperature for January, February, and March are calculated for each of the colored boxed regions near each station group in Figure 3.11 (a).

were found in the eastern sections of the 2005 austral winter cruise, as were the deepest simulated winter SAMW mixed layers, even in the case with mean forcing (Figure 3.12 (c)). Summer profiles from the cruise and Argo have high mean stratification in the east because they have very warm, fresh, and shallow mixed layers in the summer (Figure 3.15). Runoff contributes to the summer low surface salinities in profiles near Chile's coast.

The heat content of the summer profiles is also important, as this heat must be removed for the profiles to mix deeply in the winter. To allow an approximate comparison with observed heat fluxes, we scale the heat content to represent the average heat flux that would homogenize the profiles to a depth of 600 m over 200 days. Summer CTD profiles in the eastern SAMW formation region had less heat stored in the upper 600 m than profiles farther to the west (Figure 3.13 (b)). Figure 3.14 confirms that both heat content and stratification are important in determining the final winter MLD. A summer mean stratification in the upper 600 m of less than 1×10^{-5} s^{-2} seems to be a requirement for forming deep SAMW mixed layers. For profiles with mean stratifications less than 1×10^{-5} s^{-2}, a lower summer heat content will result in a deeper winter MLD (Figure 3.14).

This pattern of heat storage carries over into the Argo data. Mean upstream profiles from the cruise and Argo exhibit much more salinity structure in the upper 600 m than downstream profiles (Figure 3.15). Profiles from the west have a subsurface salinity maximum at about 400 m depth, but this feature erodes downstream. This salinity change is accompanied by a downstream decrease in temperature between 100 and 400 m, making downstream profiles denser at depths between 100 and 400 m relative to upstream profiles. This structure promotes the formation of deep mixed layers in the eastern profiles because there is less heat to remove at depth during fall and winter. A low summer heat content alone does not ensure a deep winter mixed layer; the winter forcing must be strong enough to remove the summer mixed layer stratification. In this way, variations in forcing strength do contribute to each winters' expression of the SAMW mixed layers by controlling where and how deeply the SAMW mixes.

Many processes could contribute to the stratification and downstream reduction in heat content. Sloyan et al. (2010) indicate that wind mixing, particularly in summer to early autumn, when heat and precipitation fluxes stabilize the water colum, creates the buoyancy difference between east and west. Cross-frontal transport could also trans-

port polar waters into the SAMW formation region, changing the heat content in the surface layer. Many intrusions in SAMW density classes were observed during the 2006 austral summer cruise. Sallée et al. (2010), in estimating Southern Ocean mass exchange between the surface layer and the interior, find that substantial eddy-induced and Ekman transports of nearly 30 Sv approximately counterbalance in the surface layer. Cold core eddies were observed in the SAMW formation region during the cruises, and these eddies could potentially disperse polar waters in the SAMW formation region, reducing the stratification and heat content.

3.9   Summary

Forty-two SAMW mixed layers deeper than 400 m were observed during the 2005 austral winter cruise. The SAMW was observed north of the SAF, with the densest, coldest, and freshest mixed layers found in the cruise's eastern sections near 77 °W. Undersaturated oxygen values in the mixed layer suggest active mixing. The deep mixed layers were observed concurrently with ocean heat loss at the surface of around -200 W m^{-2}. These heat fluxes were primarily caused by the northward winds of synoptic storm systems crossing the SAF and driving relatively large sensible and latent heat fluxes.

The heat, momentum, and precipitation flux fields of five flux products are used to force a one-dimensional KPP mixed layer model initialized with profiles from the 2006 austral summer cruise. The simulated August (winter) mixed layers generated by all of the forcing products resemble Argo observations of SAMW in the southeast Pacific. Mixing driven by buoyancy loss and wind forcing is strong enough to deepen the SAMW layers; cross-frontal processes are apparently not necessary for deepening the SAMW mixed layers in winter, supporting the findings of Wang and Matear (2001). The simulated SAMW mixed layers evolved by NCEP most closely resembled Argo's SAMW observations. Wind-driven mixing is central to SAMW formation, as model runs forced with only buoyancy forcing produce very shallow mixed layers that do not resemble SAMW, supporting the results of Sloyan et al. (2010). The air-sea fluxes only effect small property changes in SAMW, but forcing strength indirectly influences the winter SAMW properties by controlling how deeply the profiles mix. The stratification and heat content of the initial profiles are important in determining the properties of the SAMW and in the likelihood of deep mixing. Highly stratified profiles with large heat storage are less likely to form deep SAMW mixed layers. In contrast, the summer

profiles just upstream of Drake Passage have less heat stored between 100 and 600 m than profiles from farther upstream, and so, with sufficiently strong winter forcing, form a cold, dense variety of SAMW.

ACKNOWLEDGEMENTS

Chapter 4

Optimum multiparameter analysis of cross-frontal exchange at the Subantarctic Front

4.1 Introduction

Strong westerly winds over the Southern Ocean propel the Antarctic Circumpolar Current (ACC). During winter, deep mixed layers form north of the Subantarctic Front (SAF), the northernmost front of the ACC. McCartney (1977) named these deep winter mixed layers Subantarctic Mode Water (SAMW). SAMW becomes progressively colder, fresher, and denser as it nears Drake Passage from the west (McCartney, 1977; England et al., 1993; Talley, 1996; Hanawa and Talley, 2001). SAMW is characterized by low potential vorticity (PV) and high oxygen content and is important to many global-scale processes. It forms part of the upper limb of the global overturning circulation (Sloyan and Rintoul, 2001), renewing the lower thermocline in the Southern Hemisphere's subtropical gyres (McCartney, 1982). The heat, freshwater, and carbon transports associated with SAMW's global-scale circulation make it relevant to the Earth's climate and to the ocean's global overturning circulation (Keeling and Stephens, 2001; Pahnke and Zahn, 2005).

Many processes contribute to the formation of the deep winter SAMW mixed layers, including air-sea fluxes, wind-driven mixing, and cross-frontal advection in the form of Ekman transport, eddies, and intrusions. Previous studies have shown that

turbulent mixing driven by buoyancy loss and wind forcing is essential for forming the deep SAMW mixed layers (Wang and Matear, 2001; Sloyan et al., 2010; Holte et al., 2010). McCartney (1977) credited the cumulative effects of air-sea fluxes of heat and precipitation with driving the observed eastward freshening and cooling of SAMW from south of Africa to Drake Passage. In Chapter 3, it was shown that air-sea fluxes alone were strong enough to deepen the SAMW mixed layers in the southeastern Pacific but did little to alter the SAMW properties, which were strongly dependent on the stratification and heat content of the initial summer profile. Cross-frontal exchange, in the form of ACC meanders and eddies, Ekman transport, and intrusions, could overcome the strong PV gradient associated with the SAF to contribute to the downstream evolution of SAMW by transporting cold, fresh Antarctic Surface Waters across the ACC.

Eddies, identified as distinct cold or warm core rings or as deviations from a long-term mean, have been shown to transport polar waters across the ACC and to disperse those waters via mechanical mixing. Ansorge et al. (2006) found that eddies were likely to be significant in maintaining local heat budgets in the SAMW formation region north of the SAF; they also argued that the meridional heat and salt fluxes associated with the eddies must be adequately quantified for incorporation into climate models. Eddies have been shown to modify Ekman transport and air-sea fluxes (Sallée et al., 2008) and to influence SAMW property variability (Herraiz-Borreguero and Rintoul, 2010). Morrow et al. (2004) observed that cyclonic eddies southwest of Tasmania penetrated to 1,500 m depth and carried cold, fresh water into the SAMW formation region. Jayne and Marotzke (2002) have shown that the majority of eddy heat transport across the ACC is in the upper 1000 m. Studies investigating the relationship between ACC eddy diffusivities and PV gradients (Marshall et al., 2006) and the mean flow (Shuckburgh et al., 2009) have shown that lower cross-stream PV gradients and lower mean flows generally correspond to higher eddy diffusivities.

Many studies have looked at the importance of cross-frontal intrusions to the SAMW and Antarctic Intermediate Water (AAIW) layers, including Ekman transport. Intrusions are generally viewed as evidence for strong lateral fluxes of heat and salt and generally indicate sub-surface lateral exchange between water masses (Joyce, 1977; Ruddick, 2003). Ekman transport dominates the temporal variability of SAMW properties, as air-sea fluxes alone cannot account for the observed temporal variability of SAMW (Speer et al., 2000; Sloyan and Rintoul, 2001; Rintoul and England, 2002b). Dong et al.

(2008) found that Ekman transport could contribute to SAMW formation in the Indian Ocean. Ito et al. (2010) identified Ekman transport as the primary mechanism for the transport of anthropogenic CO_2 across the ACC. Northward Ekman transport is approximately balanced by southward eddy transport (Karsten and Marshall, 2002; Sallée et al., 2010). Park and Gambéroni (1997), in the Indian Ocean, found that cross-frontal injections of AAIW across the SAF were not continuous in time and space, but occurred impulsively and were associated with meanders and eddies in the ACC.

In this study we use observations from two recent hydrographic cruises and an optimum multiparameter (OMP) analysis (Tomczak and Large, 1989) to evaluate the cumulative exchange, via transport and mixing, across the SAF in the southeast Pacific Ocean. The first cruise, in austral winter (August 23 to October 5, 2005) observed the deep SAMW mixed layers that form north of the SAF; the second cruise, occupying the same cruise track in austral summer (January 30 to March 14, 2006), observed their subsequent restratification.

The 135 and 105 CTD/Rosette/LADCP stations collected on the winter and summer cruises, respectively, were first examined for evidence of cross-frontal exchange. Numerous intrusions crossing the SAF were observed, as well as cold-core eddies in the SAMW formation region. The temperature, salinity, and nutrient datasets were then used to conduct an OMP analysis to estimate the overall effect of the cross-frontal exchange along various isopycnals, rather than focusing on the specific mechanisms. OMP is an inverse method typically used to examine the spreading and mixing of water masses, so it is useful for tracking the exchange of waters from south of the SAF into the SAMW formation region.

The remainder of the chapter is organized as follows: section 2 describes the cruise and remote sensing data used in the analysis; section 3 describes the evidence of cross-frontal exchange; section 4 outlines the OMP method and its application. Section 5 contains the OMP results. Section 6 summarizes the findings and considers the implications for SAMW formation.

4.2   Data

Two hydrographic surveys conducted on R/V Knorr in the southeast Pacific Ocean provide high quality, synoptic observations of the SAF and the SAMW formation region during winter (August 23 to October 5, 2005) and summer (January 30 to March
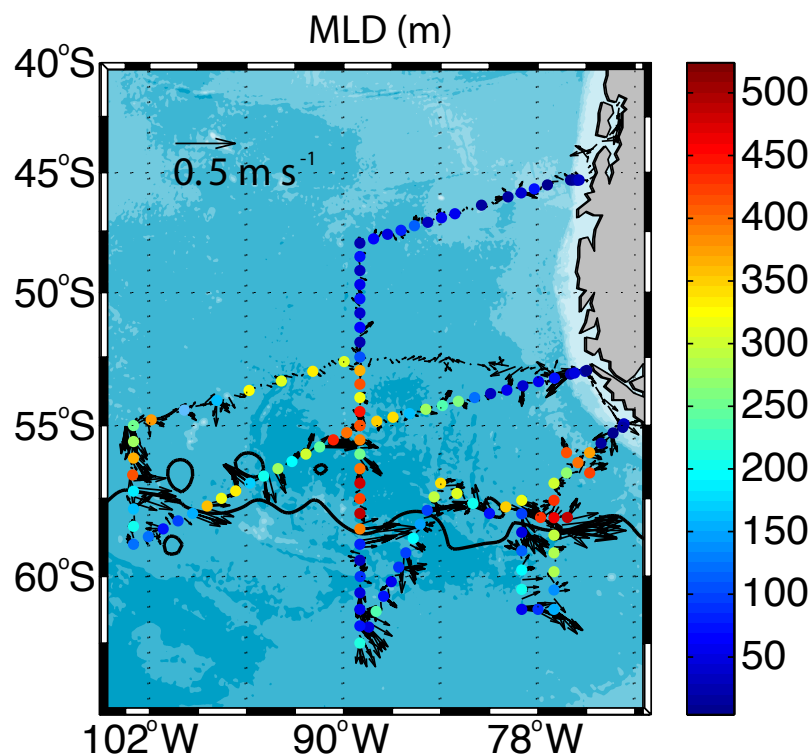
Figure 4.1: Mixed layer depth at CTD stations for the 2005 austral winter cruise extend from 0 m (blue) to 550 m (red). Underway ADCP currents (black arrows) averaged from 100 to 450 m are plotted every half hour along the cruise track. The maximum velocities are approximately 0.5 m s^{-1}. The mean AVISO dynamic topography contour that most closely matched the Subantarctic Front location in hydrography and ADCP data is also plotted (black line). The mean dynamic topography was calculated over the cruise period, August 23 to October 5, 2005. The bathymetry is contoured at 1000 m intervals. The sections plotted in Figure 4.3 were taken along 89°W.

14, 2006). Both cruises departed from Punta Arenas, followed a sawtooth path out to 103°W, and concluded near Puerto Montt, crossing the SAF six times on each cruise (Figure 4.1). CTD station spacing was approximately 50 km. Each cruise included two diamond-patterned intensive surveys, one in the SAMW formation region and another at the SAF. The location of these intensive surveys varied by cruise depending on the position of the SAF. Both cruises can be divided into three regions: (1) the region of shallow mixed layer depths (MLDs) equatorward of the deep SAMW mixed layers (north of 52°S and along Chile's coast); (2) the region of deep SAMW mixed layers north of the SAF (capped in summer); and (3) the region south of the SAF, the Polar Frontal Zone (PFZ), characterized by shallower, colder, and fresher mixed layers relative to the SAMW region. These regions are referred to as the gyre, SAMW, and PFZ regions in the paper.

The 2005 austral winter and 2006 austral summer cruises collected 135 and 105 CTD/rosette/LADCP profiles, respectively, providing full depth profiles of temperature, salinity, oxygen, and velocity. Bottle samples (from a 24 bottle rosette in winter and a 36 bottle rosette in summer) were analyzed for dissolved oxygen, salinity, phosphate, nitrate, and silicate. These data were acquired and processed by Scripps Institution of Oceanography's Ocean Data Facility. Carbon parameters and chlorofluorocarbons were also collected during the winter cruise (Hartin et al., 2010). The lowered acoustic Doppler current profiler (LADCP), a 150 kHz RD Instruments Phase 3 broadband ADCP, provided full depth profiles from 60 m interpolated to a 20 m sampling interval. The velocity data are described in Chereskin et al. (2010).

In addition to the cruise data, remote sensing observations and autonomous floats are used to identify the large-scale conditions in the cruise region. Argo floats, of which the winter cruise deployed thirteen, have continuously sampled the cruise region since 2003, providing greater temporal coverage but reduced horizontal and vertical resolution relative to the cruises. Argo floats generally sample to a depth of 2000 meters and measure temperature, salinity, and pressure at roughly 70 depth levels. Vertical sample spacing for most floats is less than 20 meters to depths of 400 meters, below which the spacing increases to 50 meters. In this study we use 4994 Argo profiles collected in the SAMW region of the cruise. Argo data are available online at http://www.usgodae.org/argo/argo.html. AVISO merged satellite topography, available weekly at 0.25 degree resolution, is used to determine the mean position

of the SAF during the cruises and to identify eddies. AVISO is provided online at http://www.aviso.oceanobs.com. All densities listed in the remainder of the paper are potential densities referenced to the sea surface (σ_θ).

4.3   Evidence of cross-frontal transport

Argo profiles in the SAMW formation region freshen and cool between the 27.0 and 27.3 kg m^{-3} isopycnals from 103°W to 73°W (Figure 4.2). SAMW mixed layers in the southeast Pacific attain their maximum winter potential density of approximately 27.05 kg m^{-3} just upstream of Drake Passage, near 75°W. Therefore, much of the freshening and cooling observed by Argo is well beneath the mixed layer and hence is not due to local air-sea fluxes of heat and freshwater. Likewise, the 27.1, 27.2, and 27.3 kg m^{-3} isopycnals are beneath most of the wind-driven turbulent mixing identified by Sloyan et al. (2010), which is primarily concentrated in the upper 600 m. One possible mechanism for this along-front evolution of properties in the SAMW region is the cross-frontal exchange of cool, fresh polar waters.

Waters from the PFZ, however, do not flow freely across the SAF. Sections along 89°W from the 2005 austral winter and 2006 austral summer cruises reveal a clear separation between waters in the SAMW region and polar waters south of the SAF (Figure 4.3). Both the PV structure of the SAF and kinematic effects of the ACC inhibit cross-frontal exchange. Bower et al. (1985), in a study of the Gulf Stream, found that above 1800 m cross-frontal mixing was primarily limited by the PV gradient. Similarly, Beal et al. (2006) found that a high cross-stream gradient of PV was the dominant mechanism for water mass separation near the surface in the Agulhas Current. These current systems differ from the ACC observations in this study, in that they often exceed 1 m s^{-1}.

Kinematic effects can also limit cross-frontal exchange above a current's "steering level," the depth at which the current speed is equal to the phase speed of meanders in the current (Owens, 1984; Beal et al., 2006; Abernathey et al., 2010). Abernathey et al. (2010) calculated a phase speed of $\sim$2 cm s^{-1} and a "steering level" of 2000 m for the ACC. Following the approach of Abernathey et al. (2010), we construct a Hovmöller diagram of sea surface height in the study region to estimate the meander phase speed of the ACC (not shown). The observed phase speed of $\sim$2.8 cm s^{-1} corresponds to a "steering level" of approximately 1500 to 2000 m; thus, kinematic effects could also limit
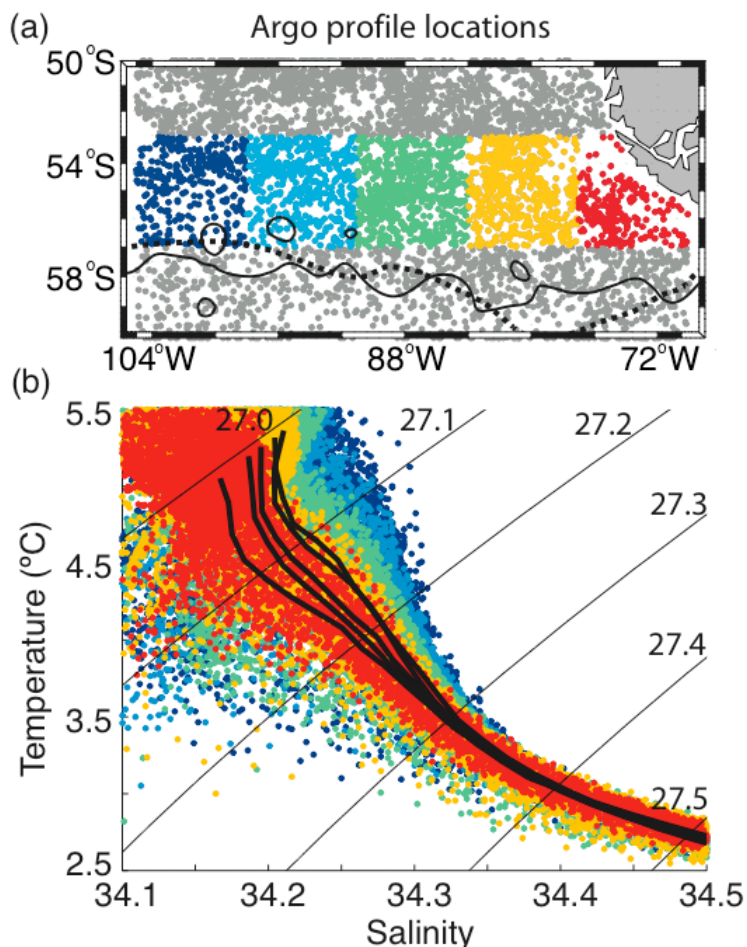
Figure 4.2: (a) Map of 4994 Argo profiles collected between January 2003 and February 2010. The profiles collected between 53 and 57°S are binned into five longitude groups; the bins, of 7° width, are centered at 73°W (red), 80°W (orange), 87°W (green), 94°W (light blue), and 101°W (dark blue). The mean AVISO dynamic topography contour that most closely matched the Subantarctic Front location during the 2005 austral winter cruise in hydrography and ADCP data is also plotted (black line). The mean dynamic topography was calculated over the cruise period, August 23 to October 5, 2005. The SAF defined by Orsi et al. (1995) is marked by the dashed black line. The latitude range of the binned profiles is generally north of the SAF and in the SAMW formation region. The temperature-salinity diagram of the binned profiles is plotted in (b), where color again corresponds to each profile's longitude bin. The mean temperature and salinity values for each longitude bin are also plotted (black lines). The mean profiles cool and freshen to the east. Potential density is contoured at 0.1 kg m^{-3} intervals from 27.0 to 27.5 kg m^{-3}.
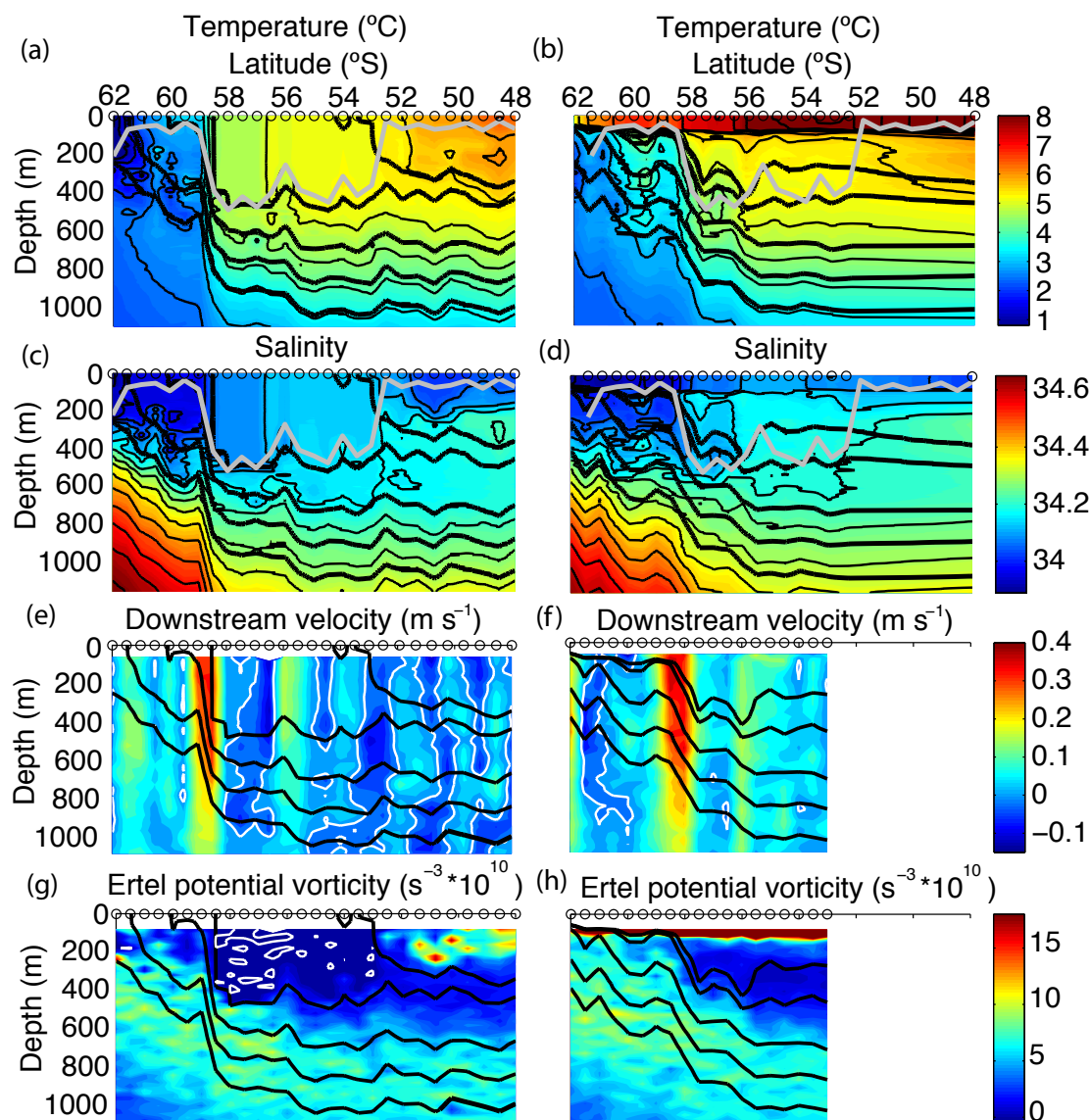
Figure 4.3: Sections of (a,b) potential temperature, (c,d) salinity, (e,f) downstream velocity, and (g,h) Ertel potential vorticity along 89°W from the 2005 austral winter cruise (left column) and the 2006 austral summer cruise (right column). Potential density (bold black lines) is contoured for the 27.0, 27.02, 27.1, 27.2, and 27.3 kg m^{-3} isopycnals. The 2005 cruise MLD (grey line) is plotted for (a,b,c, and d); it is shifted 0.6° for the summer sections to match the location of the Subantarctic Front. White contours in (e,f,g, and h) denote velocities and Ertel potential vorticities that are less than zero. The CTD station locations are denoted by circles at the surface. The LADCP was removed from the rosette for northerly stations during the summer cruise, hence the data gap.
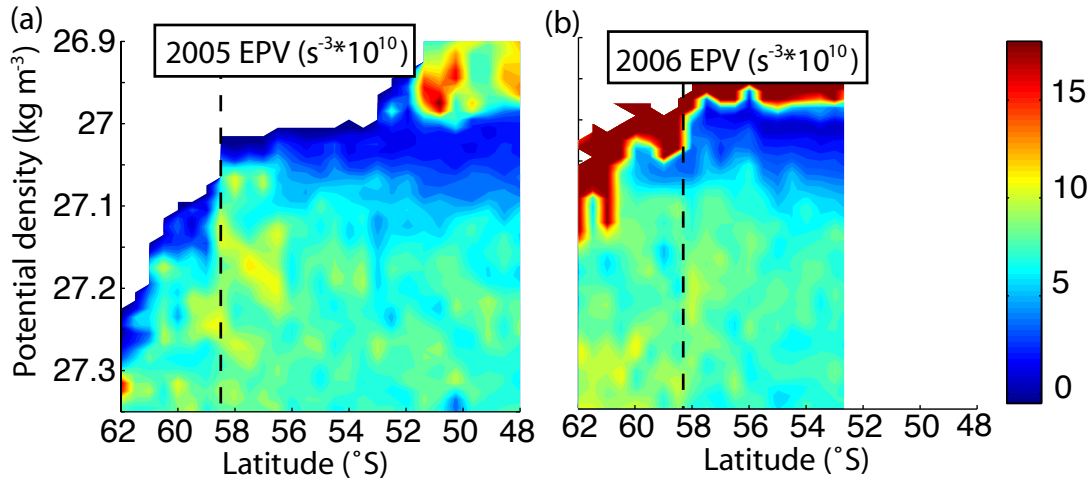
Figure 4.4: Ertel potential vorticity contoured against density and latitude for sections along 89°W from the (a) 2005 and (b) 2006 cruises. The location of the Subantarctic Front during each section is marked by the dashed line.

cross-frontal exchange at SAMW densities.

To examine how the PV structure of the SAF might limit cross-frontal exchange, we calculate the 2-D Ertel potential vorticity (EPV) following Beal et al. (2006). EPV includes terms for the horizontal and vertical velocity shears that, because of the sloping isopycnals within the SAF, can significantly contribute to the vorticity normal to the isopycnals (Beal et al., 2006; Joyce et al., 2009). The cruise sections are first rotated into a cross- and along-front coordinate system; the origin is located at the maximum vertically-averaged current and oriented so that the cross-front direction is normal to the maximum current vector. The density profiles are smoothed with a 20 m running mean and sub-sampled to match the LADCP sampling. The EPV is then calculated using

$$EPV = \frac{g}{\rho}\left[f\frac{\partial\rho}{\partial z} + \left(\frac{\partial v}{\partial x}\frac{\partial\rho}{\partial z} - \frac{\partial v}{\partial z}\frac{\partial\rho}{\partial x}\right)\right], \tag{4.1}$$

where g is the acceleration due to gravity, ρ is the potential density, f is the Coriolis parameter, z is the vertical coordinate (positive upwards), x is the cross-front coordinate and v is the along-front velocity. The first term on the right-hand-side is the planetary vorticity term. The second and third terms are related to the horizontal and vertical shears, respectively. An analysis of the terms of the EPV reveals that in this region of the SAF the planetary term dominates the shear terms.

During the 2005 austral winter cruise, a strong EPV gradient was observed along 89°W between the 27.05 and 27.175 kg m^{-3} isopycnals and is hypothesized to limit
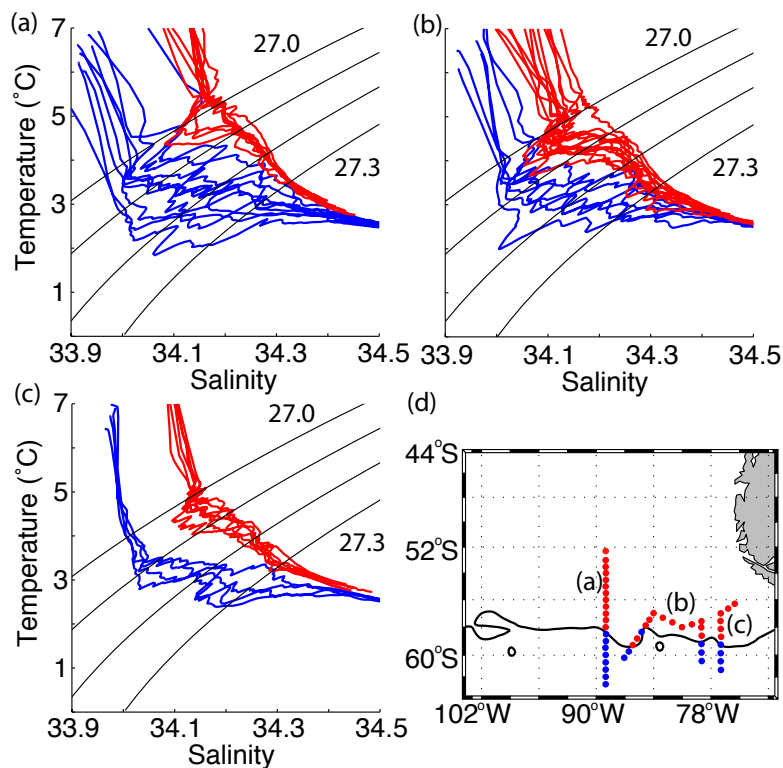
Figure 4.5: Temperature-salinity diagrams for 3 regions from the 2006 austral summer cruise; (a) 89°W, (b) zig-zag centered at 83°W, and (c) 77°W. The profile locations for each region are shown in (d). Red corresponds to profiles in the SAMW formation region and blue corresponds to profiles in the PFZ. Potential density (black lines) is contoured in (a), (b), and (c) at 0.1 kg m^{-3} intervals from 27.0 to 27.3 kg m^{-3}.

exchange across the SAF (Figure 4.4 (a)). The density break between the SAMW mixed layers and the waters south of the SAF is also clearly visible. The 2006 austral summer cruise EPV is notable for a small EPV gradient across the SAF between the 27.04 and 27.08 kg m^{-3} isopycnals, perhaps a pathway for cross-frontal exchange at the base of the SAMW mixed layers (Figure 4.4). The small EPV gradients beneath the 27.3 kg m^{-3} isopycnal, the proximity to the "steering level," as well as the convergence of Argo temperature-salinity relationships at this density in Figure 4.2, suggest that cross-frontal transport and mixing is not limited at densities greater than 27.3 kg m^{-3}. The EPV barrier took a similar form along 77°W and only extended to densities of 27.05 kg m^{-3} along 103°W.

Numerous specific instances of cross-frontal exchange were observed during the cruises. Rather than cataloging all of the intrusions, we present a few examples represen-
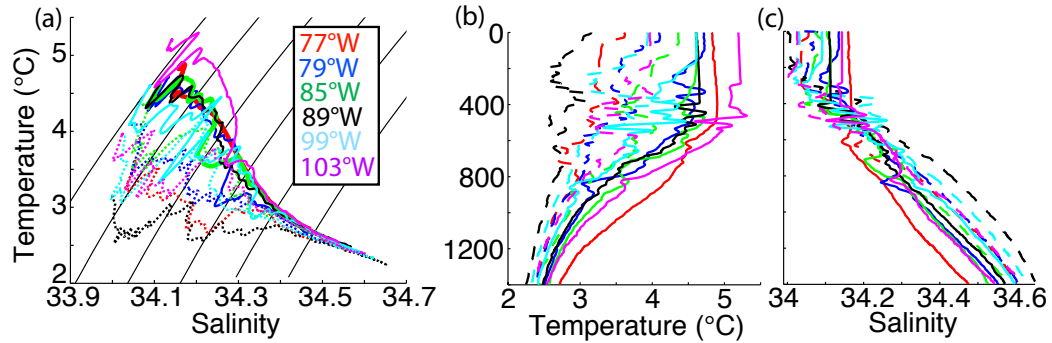
Figure 4.6: (a) Temperature-salinity diagram and (b,c) profiles from paired stations spanning the SAF from all of the front crossings during the 2005 austral winter cruise. Dashed profiles are from south of the SAF core. Potential density is contoured in (a) at 0.1 kg m^{-3} intervals from 27.0 to 27.5 kg m^{-3}.

tative of both cruises. The temperature and salinity sections along 89°W from the 2006 austral summer cruise reveal a large intrusion in the SAMW formation region just north of the SAF (Figure 4.3 (b,d)). This relatively fresh and cold feature impinged on capped SAMW layers, and corresponds to the minimum cross-frontal EPV gradient in Figure 4.4 (b). The temperature-salinity characteristics of the large intrusion along 89°W, as well as other intrusions from the 2006 austral summer cruise, are shown in Figure 4.5. The largest intrusions were observed at the base of the SAMW layers, between the 27.0 and 27.1 kg m^{-3} isopycnals. The intrusion observed along 89°W seems to extend to 77°W, as similar intruding structures were observed in downstream SAF crossings, particularly along the entire section that parallels the SAF (Figure 4.5 (b)). A similar structure was observed in the same region during the 2005 austral winter cruise, visible in the temperature and salinity profiles from 79°W in Figure 4.6. Chereskin et al. (2010) found that SAF meanders in the Southeast Pacific are quasi-stationary, maintaining their position relative to the deep SAMW mixed layers on seasonal time scales, which could allow for the formation of such large features.

Many intrusions were observed at the six frontal crossings during the 2005 austral winter cruise, particularly in the layers immediately below the SAMW mixed layers, between the 27.0 and 27.1 kg m^{-3} isopycnals (Figure 4.6). Fewer intrusions into the SAMW mixed layers were observed during the 2005 austral winter cruise, most likely because any intrusions would be quickly incorporated into the SAMW by convection-driven turbulent mixing in the mixed layer.

The salinity of the shallow summer mixed layer in the SAMW formation region also suggests the importance of cross-frontal exchange in the form of Ekman transport (Figure 4.3). The highest summer mixed layer salinities along 89°W are at 55°S and are approximately 0.05 fresher than the capped SAMW. Farther south in the SAMW formation region, the shallow summer mixed layer freshens, increasing the salinity difference between the capped SAMW and the summer mixed layer to 0.1. This pattern suggests that surface waters from south of the SAF could penetrate to nearly 3° north of the SAF during summer. In winter, this freshwater would be mixed into the deep SAMW mixed layers.

Besides intrusions and Ekman cross-frontal exchange, a cold core eddy was observed in the SAMW formation region at approximately 96°W and 56°S during the 2005 austral winter cruise. The eddy's cyclonic rotation was captured by the LADCP (Figure 4.1). The eddy's mixed layer was 0.3°C cooler and 0.03 fresher than the surrounding SAMW mixed layers, and more than 150 m shallower. As the eddy decays, the polar water that it is transporting will be dispersed into the SAMW formation region.

From these observations, it appears as if intrusions frequently overcome the SAF's PV barrier to transport PFZ water into the SAMW formation region. Many of these intrusions are near the maximum densities of the winter SAMW mixed layers. Cross-frontal exchange via eddies and Ekman transport was also observed. The cumulative cross-frontal exchange driven by these mechanisms is difficult to quantify.

4.4   Optimum multiparameter analysis: method and set-up

We employ an optimum multiparameter (OMP) analysis to examine the cumulative effect of cross-frontal transport and mixing on waters in the SAMW formation region. OMP, originally developed by Tomczak and Large (1989), is an inverse method for calculating the relative contributions of various user-defined source waters to a water sample. We use a MATLAB OMP package provided online by Johannes Karstensen at http://www.ldeo.columbia.edu/~jkarsten/omp_std/. OMP has been used to assess water mass mixing in the thermocline in the Eastern Indian Ocean (Tomczak and Large, 1989) and the Atlantic Ocean (Poole and Tomczak, 1999), to examine shelf waters in the Ross Sea (Budillon et al., 2003), and to look at water masses in Southern Drake Passage (Frants et al., 2008). Klein and Tomczak (1994) used OMP to study the diapycnal mixing of North and South Atlantic Central Water.

OMP analysis is implemented by solving an overdetermined system of linear equations, written as

$$\mathbf{Gx} - \mathbf{d} = \mathbf{r}, \tag{4.2}$$

where $\mathbf{G}$ is a matrix defining the source water parameters (in our case the temperature, salinity, silicate, nitrate, phosphate, and oxygen levels of the source waters), $\mathbf{d}$ is the vector of observed parameters for all of the cruise CTD stations, $\mathbf{x}$ is the solution vector giving the relative contribution of each source water at each CTD station, and $\mathbf{r}$ is the residual. Mass is added as an additional constraint; it is set to 1 for the source waters and the CTD stations and is unitless. The mass balance residual is then used to gauge the uncertainty of the result. Mass residuals less than or equal to 0.05 are generally considered acceptable (Tomczak and Large, 1989; Poole and Tomczak, 1999; Budillon et al., 2003). Standard OMP analysis assumes that the source water parameters defined in $\mathbf{G}$ are conserved, which is acceptable if the study region is small and the source waters are fairly close together (Leffanue and Tomczak, 2004). Including the Redfield ratio (Redfield et al., 1963), which accounts for the consumption of nutrients and oxygen, allows OMP analysis to be expanded to basin scales, as in Poole and Tomczak (1999). As our analysis is much smaller than basin-scale, we do not include a Redfield constraint.

A weight matrix, $\mathbf{W}$, accounts for each parameter's varying ability to distinguish the source waters in each water sample. For example, if the nitrate distribution in all of the water samples is largely random, it should not be given much weight in the OMP analysis. The weights can also be interpreted as accounting for differences in parameter data quality. Weights are calculated for each parameter following Tomczak and Large (1989),

$$W_j = \frac{\sigma_j^2}{\delta_{jmax}}, \tag{4.3}$$

where j indexes the parameter and δ_{jmax} is the largest source water variance for parameter j; σ_j^2 is described below. First, the variance, δ_j, is calculated for each source water. Neighboring profiles similar to the source, as judged from the temperature-salinity diagram, are assembled for each source water; the variance of each source water group is then calculated, and the largest variance is used as δ_{jmax}. The source water groups used in this study are illustrated in Figure 4.7. For smaller variances the source water parameter is representative of nearby profiles, whereas higher variances signal that there is considerable parameter variability near the source water, and that it might therefore
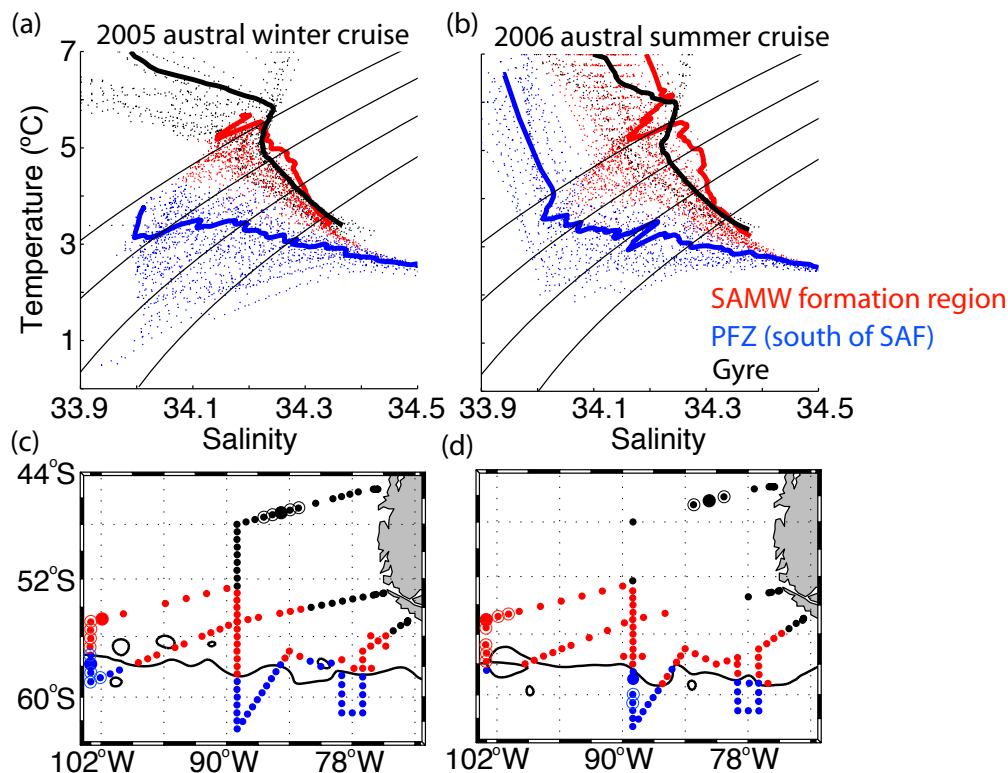
Figure 4.7: (a,b) Temperature-salinity diagrams and (c,d) maps of 2005 austral winter and 2006 austral summer cruise CTD profiles. The profiles and their locations are colored by region. Each cruise is divided into three regions, as described in section 2: SAMW region (red), PFZ (blue), and gyre region (black). In summer, the SAMW mixed layers are capped by a shallow mixed layer. The source water stations used in the OMP analysis for each cruise are denoted by bold profiles in (a,b) and large dots in (c,d). Profiles used to calculate the OMP weights and in the sensitivity analysis are marked by open circles. In (a,b), the potential density is contoured at 0.1 kg m^{-3} intervals from 27.0 to 27.3 kg m^{-3} intervals. In (c,d), the mean AVISO dynamic topography contour that most closely matched the SAF location in hydrography and ADCP data during each cruise is also plotted (black line). The mean dynamic topography was calculated over each cruise period.

be an unreliable parameter. Lastly, σ_j is calculated as

$$\sigma_j = \sqrt{1/n \sum_{i=0}^{n}(G_{ij} - \bar{G}_j)^2}, \qquad (4.4)$$

where G_{ij} is an element of $\mathbf{G}$ (parameter j, source water i) and $\bar{G}_j$ is the mean value of parameter j for the source waters. There are n source waters. Traditionally, σ_j is interpreted as a measure of how useful parameter j is at resolving the source waters; if the source waters have very different values of parameter j, then it will be a useful parameter for tracking the source waters in each of the water samples, and correspondingly have a large σ_j and weight.

Our source water selection is guided by the necessity of needing an upstream profile representative of the western SAMW region and a profile in the PFZ south of the SAF to represent the water crossing the front. We add a third source water, a profile representing subtropical gyre water, to help the OMP analysis resolve samples collected north of the SAMW formation region. The PFZ possesses the widest range of temperature-salinity profiles (Figure 4.7). In general, profiles from the PFZ cool and freshen to the east and to the south. Proximity to the SAF is important, as profiles close to the SAF are probably most representative of the water crossing the SAF. For the 2005 cruise we select a PFZ source water profile from 103°W, the westernmost section of the cruise. The 2006 austral summer cruise barely crossed the SAF at 103°W, so we use a profile from 89°W. Upstream profiles in the SAMW region, near 103°W, exhibit salinity maximums centered on the 27.1 kg m^{-3} isopycnal, a feature that has eroded by 89°W. Profiles with these subsurface salinity maxima are selected as the SAMW region source waters, as these features form extremes on the temperature-salinity diagrams. The subtropical gyre region was characterized by two groups of profiles on both cruises. One group, fresher between the 27.0 and 27.3 kg m^{-3} isopycnals, was observed closer to Chile's coast; the other was observed on the sections north of 52°S. The gyre source water is chosen from the northern section, as this is more likely representative of the gyre; the fresher branch could be the result of mixing with water from the PFZ or SAMW region.

Numerous source water stations were tested, all of which produced similar results. A final combination of stations was selected based on its reliable mass balance residuals. The stations used for the 2005 OMP analysis are located at 102°W and 54.5°S (SAMW), 103°W and 58°S (PFZ), and 85°W and 47°S (subtropical gyre). For the 2006 analysis, the stations are located at 103°W and 55°S (SAMW), 89°W and 58°S (PFZ), and 82°W

Table 4.1: Definitions of source waters used in the OMP analyses. Nutrients are given in mmol/kg.

Source water	Temperature (°C)	Salinity	Oxygen (mmol/L)	Nitrate	Silicate	Phosphate	PV$*10^{10}$ (s^{-3})
2005 27.1 - 27.2 σ_θ							
Upstream SAMW	4.43	34.27	221	29.2	24.4	2.0	8.18
PFZ	3.22	34.07	276	27.5	17.5	1.9	7.94
Gyre	4.44	34.26	222	29.6	22.6	2.0	5.89
2005 27.2 - 27.3							
Upstream SAMW	3.85	34.31	208	31.1	34.1	2.1	6.92
PFZ	3.22	34.23	230	31.2	32.0	2.1	8.08
Gyre	3.84	34.32	200	32.2	35.0	2.2	7.07
2006 27.0 - 27.1							
Upstream SAMW	4.81	34.16	270	24.8	12.1	1.7	5.53
PFZ	3.67	34.03	295	24.9	11.6	1.8	6.05
Gyre	5.29	34.23	262	24.4	10.5	1.7	3.00
2006 27.1 - 27.2							
Upstream SAMW	4.36	34.26	223	29.4	25.6	2.0	8.22
PFZ	3.28	34.12	263	28.5	22.3	2.0	6.65
Gyre	4.52	34.25	227	28.8	22.0	2.0	6.90
2006 27.2 - 27.3							
Upstream SAMW	3.72	34.30	210	31.5	35.5	2.2	7.65
PFZ	3.20	34.22	233	30.8	32.3	2.1	7.93
Gyre	3.92	34.30	203	31.7	34.2	2.2	6.86

Table 4.2: Weights used in the OMP analyses.

Parameter	2005 27.1-27.2	2005 27.2-27.3	2006 27.0-27.1	2006 27.1-27.2	2006 27.2-27.3
Temperature	59.6	34.3	44.7	55.0	12.4
Salinity	39.3	47.5	73.7	32.4	11.1
Oxygen	14.0	51.1	12.8	25.8	15.5
Nitrate	15.7	10.1	3.0	2.9	2.8
Silicate	10.5	8.0	3.0	7.2	2.5
Phosphate	1.7	5.3	4.8	2.1	2.0

and 46°S (subtropical gyre). The locations and profiles of the source waters are shown in Figure 4.7.

The OMP analysis is conducted for two primary isopycnal ranges: 27.1 - 27.2 kg m^{-3} and 27.2 - 27.3 kg m^{-3}. Isopycnals in these ranges display the greatest downstream change in temperature and salinity characteristics (Figure 4.2) and are outside the direct influence of air-sea fluxes. An OMP analysis is also run for the 27.0 - 27.1 kg m^{-3} isopycnal range for the 2006 austral summer cruise. These lighter isopycnals outcrop during winter, particularly south of the SAF, but provide a sense of the transport closer to the winter mixed layer. Cruise bottle data is averaged within each isopycnal range. All of the OMP runs use temperature, salinity, oxygen, silicate, nitrate, and phosphate as parameters. An additional set of five repeat runs includes PV as a parameter. The PV is calculated using only the planetary term, fN^2, as an analysis of the terms in Equation (4.1) reveals that this term dominates the EPV. The EPV terms related to the vertical shear of horizontal velocity only marginally contribute to the EPV because there is relatively little vertical velocity shear in the upper 1000 m in this section of the ACC, particularly compared to Joyce et al. (2009)'s observations of the Gulf Stream. The parameter values for all of the OMP runs are shown in Table 4.1; the weights are shown in Table 4.2. The weights are similar to weights used by Budillon et al. (2003) and Frants et al. (2008). The weights for phosphate and nitrate are small because these parameters displayed little variation between source waters. The PV and mass balance weights are arbitrary; as other studies have done, we employ the temperature weight for mass and PV.

Following Poole and Tomczak (1999) and Hinrichsen and Tomczak (1993), a sensitivity analysis is conducted to determine the robustness of the results to variations of the source water parameters. The source water parameters are defined in **G**. For the sensitivity analysis, the OMP analysis is repeated with a simulated **G** composed of parameters generated randomly from normal distributions with the same means and variances as the original source water parameters. The means and variances of the source water parameters are calculated for the same groups of source water profiles used to determine δ_j. **G** is randomly generated fifty times for each of the five isopycnal ranges, and run through the analysis to produce simulated OMP runs. The root-mean-square (RMS) error of each station is calculated by taking the standard deviation of the difference between the SAF water content of the standard and simulated OMP runs.

The RMS error is then spatially averaged over all of the cruise stations.

4.5   Optimum multiparameter analysis: results

The OMP analysis reveals that the fractional content of PFZ water in the SAMW formation region increases in the along-front direction between the 27.1 and 27.3 kg m^{-3} isopycnals (Figure 4.8). Profiles from the cruises' eastern sections, near 77°W, exhibit greater fractional contents of PFZ water than upstream profiles. This is most evident in the 27.1 - 27.2 kg m^{-3} isopycnal range for both cruises. The 2006 27.2 - 27.3 kg m^{-3} PFZ water fractional contents are noisier than for the other ranges, but follow the same pattern within 4° latitude of the SAF. Profiles at or immediately south of the SAF have high concentrations of PFZ water, as they should. Profiles farther south in the PFZ have unrealistically large mass balance residuals, as the source waters were not defined to resolve these profiles.

PFZ water fractional content essentially doubles along-front in the SAMW formation region, increasing from approximately 0.1 near 100°W to 0.2 near 77°W (Figure 4.9). The 27.1 - 27.2 kg m^{-3} isopycnal range exhibits the largest along-front increase in PFZ water fractional content, increasing by 0.15 in both cases. The PFZ water fractional content of the 2006 27.2 - 27.3 kg m^{-3} isopycnal range increases by 0.15 between the first two longitude bins, but decreases in the easternmost bin. Water samples from 2005 in the SAMW region between 27.2 and 27.3 kg m^{-3} exhibit the smallest along-front increase in PFZ water fractional content, 0.075.

Adding PV as a parameter does not substantially alter the results (Figure 4.9). Including PV improves the 2006 27.2 - 27.3 kg m^{-3} isopycnal OMP result; with PV, we find an along-front monotonic increase in PFZ water content. With PV, both of the 2006 isopycnal ranges exhibit along-front PFZ water fractional content increases of 0.15. They start with smaller PFZ water contents, and exhibit more of an increase in the final longitude bin. The along-front increase in PFZ water fractional content remains at 0.075 for the 2005 27.2 - 27.3 kg m^{-3} isopycnal range. The along-front change in PFZ water content is only 0.1 for the 2005 27.1 - 27.2 kg m^{-3} isopycnal run, most likely because there is such a strong PV gradient across the SAF in this range during the winter cruise.

The OMP results for the 2006 27.0 - 27.1 kg m^{-3} isopycnal range also reveal an along-front increase in the fractional content of PFZ water in the SAMW formation region, mirroring the results of the denser isopycnals (Figure 4.10). This run also demon-
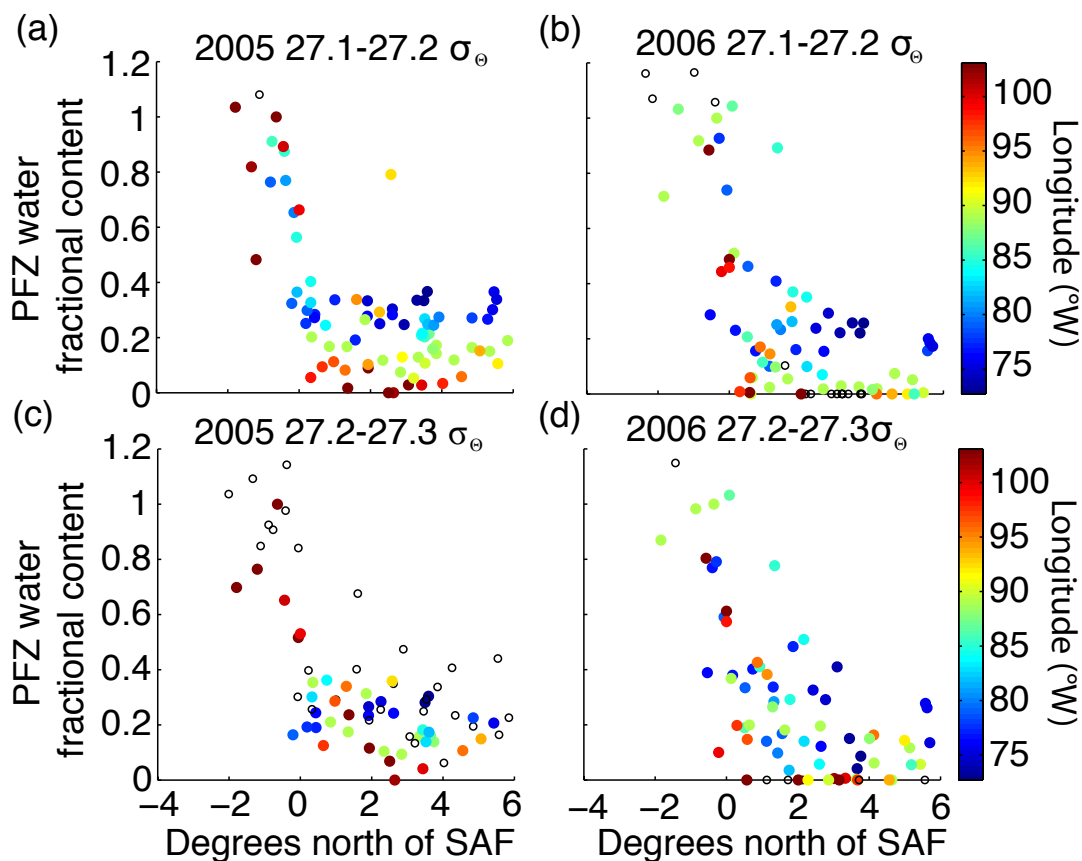
Figure 4.8: OMP-derived fractional content of PFZ water for the 2005 austral winter (a,c) and 2006 austral summer (b,d) cruises performed in two potential density ranges, 27.1 - 27.2 kg m^{-3} and 27.2 - 27.3 kg m^{-3}. These OMP runs did not include PV as a parameter. The fractional content of PFZ water is plotted against distance from the SAF, which is calculated by interpolating the SAF latitudes observed in hydrography and ADCP data to the profile longitudes (nearest two crossings). Color corresponds to profile longitude, from 103°W (red) to 73°W (blue). Stations with mass residuals greater than 0.05% are denoted by black circles.

Figure 4.9: Mean PFZ water fractional content for the OMP runs averaged into zonal bins for (a) standard OMP analysis and (b) OMP analysis that includes PV as a parameter. The OMP runs are performed for two potential density ranges for the 2005 austral winter cruise: 27.1 to 27.2 kg m^{-3} (green) and 27.2 to 27.3 kg m^{-3} (orange). The same isopycnals are used for the 2006 austral summer cruise (27.1 to 27.2 kg m^{-3} (red) and 27.2 to 27.3 kg m^{-3} (blue)). For each run, all of the stations within 6° of the front are averaged into bins from 103° to 90°W, 90° to 83°W, and 83° to 75°W. Each profile's distance from the SAF is calculated by interpolating the SAF latitudes observed in hydrography and ADCP to the profile longitudes.
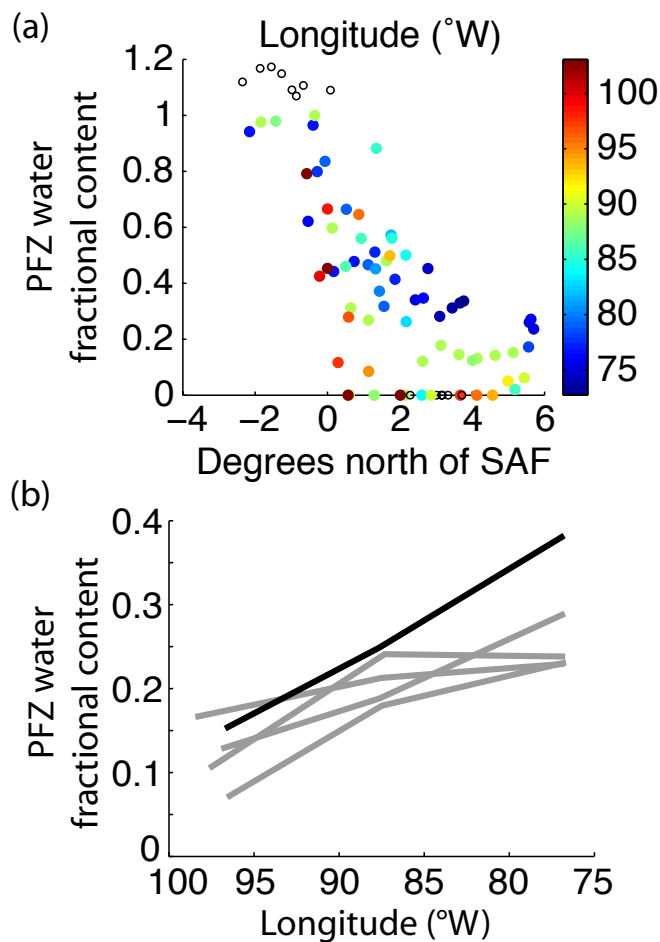
Figure 4.10: (a) Fractional content of PFZ water for the 2006 austral summer cruise performed in the potential density range 27.0 - 27.1 kg m^{-3}. The fractional content is plotted against distance from the SAF, which is calculated by interpolating the SAF latitudes observed in hydrography and ADCP data to the profile longitudes. Color corresponds to profile longitude, from 103°W (red) to 73°W (blue). Stations with mass residuals greater than 0.05% are denoted by black circles. In (b), the mean values of fr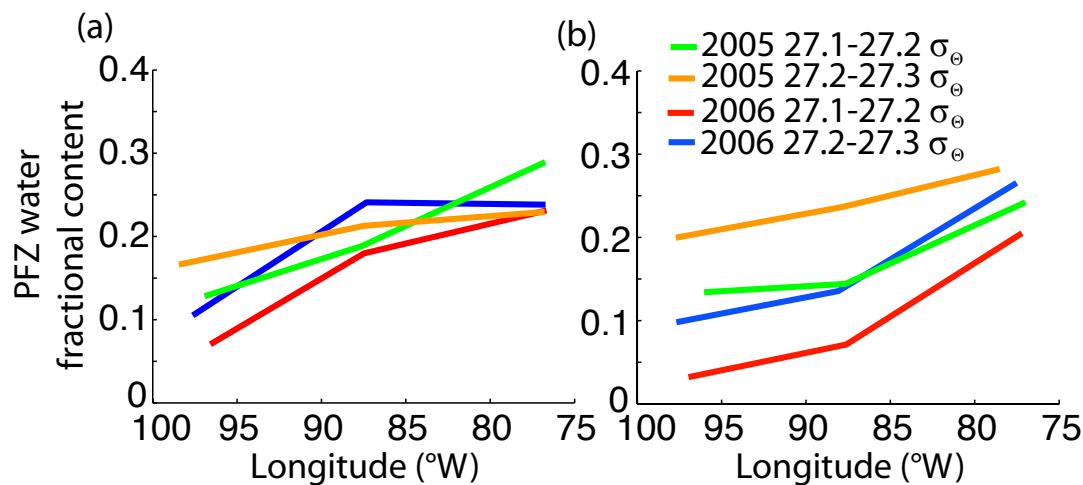actional content of PFZ water for the 2006 potential density range 27.0 to 27.1 kg m^{-3} (black) are averaged in zonal bins as in Figure 4.9. The mean values for the other density ranges are plotted in grey.

Table 4.3: Mean root mean square (RMS) error of fractional PFZ water content for 50 simulations where the parameters of all three source waters are varied according to their respective means and variances. The mean is calculated over all CTD stations.

2005 27.1-27.2	2005 27.2-27.3	2006 27.0-27.1	2006 27.1-27.2	2006 27.2-27.3
3.7%	5.9%	5.8%	4.6%	5.9%

strates PFZ water content as a function of latitude, with the largest PFZ water contents found closest to the SAF and decreasing farther north. This shallow run exhibits a greater final mean PFZ water content at 77°W than any of the other runs (Figure 4.10).

The results of the sensitivity analysis are displayed in Table 4.3. Varying the source water parameters produces RMS errors of PFZ water fractional concentrations of up to 6% in the SAMW region, suggesting that the results are robust to source water parameter variations. The result is not due to a fortuitous selection of source waters, but rather would hold if we selected any of the nearby stations as source waters.

4.6   Discussion

Argo profiles in the SAMW formation region north of the SAF in the southeast Pacific Ocean exhibit an along-front evolution, becoming fresher and cooler to the east between the 27.0 and 27.3 kg m^{-3} isopycnals (Figure 4.2). The along-front evolution cannot be produced by simple downstream vertical mixing, as this would only erode the salinity minimum feature at approximately 27.1 kg m^{-3}, not maintain it downstream. Likewise, the densest SAMW winter mixed layers in this region reach 27.05 kg m^{-3}, so much of this range is outside the influence of local surface forcing. In this study, cross-frontal exchange is considered as a possible mechanism that could produce this along-front evolution. Cross-frontal exchange, both mixing and transport, can be accomplished by many processes, including meanders in the SAF, intrusions, eddies, frontal convergence, and current shear.

However, the steep isopycnals and EPV structure of the SAF generally act to limit exchange in the upper ocean, as evidenced by the clear separation of waters north and south of the SAF. Two cruises in the southeast Pacific Ocean in 2005 and 2006 were designed to sample the SAMW formation region north of the SAF and the colder, polar waters to the south. Cruise observations reveal that, above the 27.4 kg m^{-3} isopycnal, the SAF effectively separates water masses on either side. Analysis of the EPV structure

shows that it acts as a barrier to exchange above the 27.2 kg m^{-3} isopycnal, at a depth of roughly 800 m north of the SAF.

Even with an EPV barrier, numerous instances of cross-frontal exchange were observed during both cruises. Large intruding structures with longitudinal dimensions of approximately 15° were observed (Figure 4.5). Numerous intrusions were observed at the base of the winter SAMW mixed layers (Figure 4.6). A cold-core eddy was observed in the SAMW formation region. Beal et al. (2006) found that cross-frontal mixing events in the Agulhas were primarily driven by mesoscale features, such as meanders and shear-edge eddies, even though kinematic steering and PV gradients inhibited cross-frontal mixing near the surface.

With such a multitude of mechanisms for cross-frontal exchange, we utilize an OMP analysis to estimate the fractional content of waters from south of the SAF in the SAMW formation region. The OMP analysis does not distinguish between mixing and cross-frontal transport, but instead provides an estimate of the cumulative effect of cross-frontal exchange in the SAMW formation region. The OMP analysis reveals an along-front increase in PFZ water fractional content in the SAMW formation region at isopycnals between 27.0 and 27.3 kg m^{-3}. The fractional content of PFZ water increases along-front by approximately 0.1 for every 15° of longitude, even when PV is included as a parameter (Figure 4.9). The cross-frontal exchange diagnosed by the OMP analysis represents the cumulative cross-frontal exchange integrated over many seasons. For this reason, the OMP results at individual CTD stations cannot be tied to specific cross-frontal exchange features observed during the cruises.

What are the implications for SAMW if this pattern of cross-frontal transport carries to the surface? We conduct a simple bulk calculation with SAMW mixed layer properties from the 2005 austral winter cruise to determine if the OMP-diagnosed cross-frontal exchange could account for the observed along-stream evolution of SAMW. The similarity of the OMP results at all subsurface isopycnal levels tested here, including 27.0 - 27.1 kg m^{-3}, gives us confidence that similar transport might occur near the mixed layer. The calculation is initialized with SAMW winter mixed layers collected on the 2005 cruise along 103°W. The OMP results show that as the profile moves downstream, its PFZ water fractional content increases by approximately 0.1 every 15° of longitude (Figures 4.9 and 4.10). The initial mixed layer temperature and salinity are therefore adjusted downstream, mixing a 0.1 fraction of PFZ water into the mixed layer. The PFZ
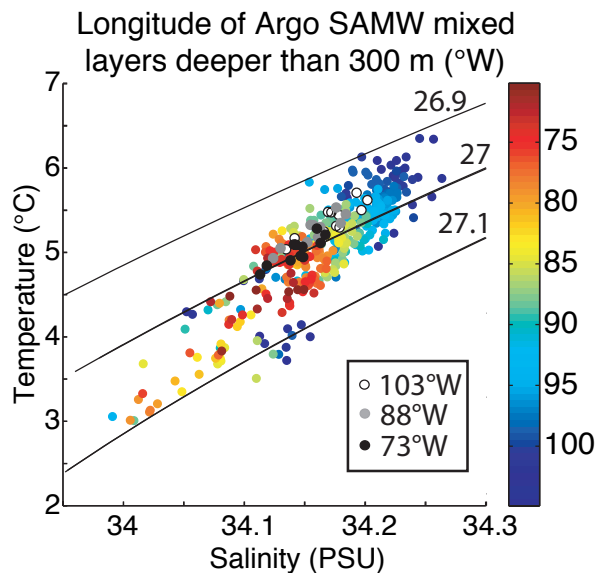
Figure 4.11: Mixed layer temperature-salinity diagram for Argo profiles collected in the cruise region with MLDs deeper than 300 m; the color corresponds to the profile longitude. Plotted over the Argo data are the results of a simple bulk calculation. The bulk calculation is initialized with mixed layers from the 2005 austral winter cruise section along 103°W (open circles). The mixed layers are evolved with bulk cross-frontal fluxes that increase the fractional content of PFZ water by 0.1. The PFZ water is represented by the mean of the first three mixed layers south of the SAF along 103°W. This mixed layer is further evolved by cross-frontal exchange that increases the PFZ water fractional content by an additional 0.1. Here the PFZ water is represented by the mean of the first three mixed layers south of the SAF along 89°W. The evolved downstream mixed layers are plotted in grey (88°W) and black (73°W). Potential density (black lines) is contoured at 0.1 kg m^{-3} intervals from 26.9 to 27.1 kg m^{-3}. The Argo MLDs are calculated following Holte and Talley (2009).

water is defined by the mean of the first three mixed layers immediately south of the SAF. This evolution is performed for two iterations, corresponding to an along-front movement of approximately 30°, until the mixed layer should approximate the profiles observed in the cruise's eastern sections near 73°W. Figure 4.11 shows that cross-frontal exchange could cause the downstream evolution of SAMW mixed layer properties observed by Argo; the mixed layers in the simple bulk calculation mirror the along-front freshening and cooling of the SAMW mixed layers observed by Argo.

This result is consistent with Holte et al. (2010), which found that air-sea fluxes were necessary for forming the deep SAMW mixed layers, but did little to change their properties; cross-frontal exchange offers a viable mechanism for explaining the along-

front evolution of SAMW properties. Sallée et al. (2006) found that Ekman transport of cold and fresh water from the south was consistent with the loss of salt and heat in the SAMW mixed layers. Studies looking at the temporal variability of SAMW have long-cited Ekman transport as a prime source of variability (Rintoul and England, 2002b). Naveira Garabato et al. (2009) found that the Ekman transport of Antarctic surface waters from the south contributed significantly to SAMW freshening and cooling from 1990 to 2005. Our findings contrast with McCartney (1977), which hypothesized that the cumulative effects of heat loss and precipitation modified the SAMW along the ACC path.

The trend in cross-frontal exchange diagnosed by the OMP analysis cannot be maintained around the entire ACC. If it held along the entire ACC path, a water sample circumnavigating Antartica would retain only 2% of its original SAMW region water, the remainder having been replaced by PFZ water. Our analysis uses one upstream source of PFZ water, whereas in reality the water crossing the front also changes downstream, becoming fresher and cooler (not shown). With fresher and cooler source waters, the OMP analysis would require a smaller fractional content of SAF water in the SAMW formation region. Besides variation in the properties of the PFZ water crossing the SAF, the strength of the intrusions, Ekman transport, and eddies driving the exchange also vary along the SAF. Ansorge et al. (2006) and Sallée et al. (2006) have shown that eddy shedding is strongly dependent on bottom bathymetry. Shuckburgh et al. (2009) found that eddy diffusivity in the ACC is suppressed by strong mean flow. An improved understanding of the mechanisms controlling SAMW's properties, including cross-frontal exchange, will help scientists to interpret observations of SAMW's temporal and spatial variability.

ACKNOWLEDGEMENTS

Chapter 4, in full, is a reprint with minor modifications of the article "Optimum multiparameter analysis of cross-frontal exchange at the Subantarctic Front," to be submitted for publication. The dissertation author was the first author and primary researcher with contributions from co-authors Lynne Talley, Teresa Chereskin, and Bernadette Sloyan.

Chapter 5

Conclusion

Many processes contribute to Subantarctic Mode Water (SAMW) formation: gyre inflow; cross-frontal advection in the form of Ekman transport, eddies, and intrusions; heat and freshwater fluxes at the air-sea interface and at the base of the mixed layer; and mixing. This thesis primarily uses observational data from Argo and two cruises to investigate the contributions of one-dimensional buoyancy forcing and cross-frontal exchange to SAMW formation in the southeast Pacific Ocean.

Chapter 2 describes a new algorithm for finding the mixed layer depth (MLD) of individual Argo profiles and its application to profiles from the southeast Pacific Ocean. The algorithm fits straight lines to the mixed layer and thermocline, searches for subsurface property anomalies, and incorporates threshold and gradient methods to assemble a suite of possible MLD estimates. It then searches for patterns in the suite to select a final MLD. The algorithm is tested with Argo profiles from the southeast Pacific Ocean, a region of SAMW formation where winter mixed layers reach 500 m. The algorithm is compared to threshold methods that use de Boyer Montégut et al. (2004)'s criteria and to gradient methods. We find that the temperature and density algorithms tend to find shallower MLDs than their threshold counterparts. The temperature algorithm MLDs nearly matches the density algorithm MLDs. In the study region, the temperature algorithm offers a marked improvement over a temperature threshold method using the criterion of de Boyer Montégut et al. (2004); the temperature threshold method frequently overestimates winter MLDs by nearly 200 dbar for profiles in which the temperature algorithm successfully identifies temperature anomalies at the base of the mixed layer. The temperature algorithm is preferred over the temperature gradient method be-

cause of the gradient method's tendency to find anomalously deep MLDs. The density gradient method also produces many anomalous MLDs. The density algorithm reveals that the deepest MLDs in the southeast Pacific Ocean routinely reach 500 m and occur in August and September at the northern edge of the Antarctic Circumpolar Current. This is not a groundbreaking interpretation of SAMW formation. Rather, it serves as validation of the algorithm's ability to accurately identify the MLD. In ongoing work, the algorithm is being used to construct a global climatology of mixed layer properties from more than 530,000 quality-controlled Argo profiles. The climatology's enhanced representation of global mixed layer depths and the seasonal cycle should improve calculations of the mixed layer heat and CO_2 budgets, and aid in studies of other processes related to the mixed layer.

Chapter 3 examines the importance of air-sea fluxes of heat and momentum to SAMW formation. It first catalogues and describes the deep SAMW mixed layers observed during the 2005 austral winter cruise. Forty-two SAMW mixed layers deeper than 300 m were observed north of the Subantarctic Front (SAF), with the densest, coldest, and freshest mixed layers found in the cruise's eastern sections near 77°W. The cruise fluxes are then used to evaluate five flux products. The products' heat, momentum, and precipitation flux fields are used to force a one-dimensional KPP mixed layer model initialized with profiles from the 2006 austral summer cruise. The simulated August (winter) mixed layers generated by all of the forcing products resemble Argo observations of SAMW in the southeast Pacific Ocean. From this we conclude that mixing driven by buoyancy loss and wind forcing is strong enough to deepen the SAMW layers; cross-frontal processes are apparently not necessary for deepening the SAMW mixed layers in winter. The simulated SAMW mixed layers evolved by NCEP most closely resembled Argo's SAMW observations. Wind-driven mixing is central to SAMW formation, as model runs forced with only buoyancy forcing produce very shallow mixed layers that do not resemble SAMW, supporting the results of Sloyan et al. (2010). The air-sea fluxes only effect small property changes in SAMW, but forcing strength indirectly influences the winter SAMW properties by controlling how deeply the profiles mix. The stratification and heat content of the initial profiles are important in determining the properties of the SAMW and the likelihood of deep mixing. Highly stratified profiles with large heat storage are less likely to form deep SAMW mixed layers. In contrast, the summer profiles just upstream of Drake Passage have less heat stored between 100

and 600 m than profiles from farther upstream, and so, with sufficiently strong winter forcing, form a cold, dense variety of SAMW.

In chapter 4, cross-frontal exchange is considered as a possible mechanism for the along-front freshening and cooling of profiles north of SAF between the 27.0 and 27.3 kg m^{-3} isopycnals. This isopycnal range is generally below the mixed layer, and so is not locally forced by air-sea fluxes or wind-driven mixing. The goal of this study was to tie cross-frontal exchange to the along-front evolution of upper ocean heat content and SAMW properties documented in chapter 3. Many instances of cross-frontal exchange were observed during the cruises. Numerous sub-surface intrusions penetrated north of the SAF, even though the potential vorticity (PV) structure of the SAF often acted as a barrier to exchange. Cold-core eddies were observed in the SAMW formation region, and the low salinity of the mixed layer during the 2006 austral summer cruise, especially near the SAF, is hypothesized to be due to Ekman transport. An optimum multiparameter (OMP) analysis is used to estimate the cumulative cross-frontal exchange. The OMP analysis reveals an along-front increase in Polar Frontal Zone (PFZ) water fractional content in the region north of the SAF at isopycnals between 27.0 and 27.3 kg m^{-3}. The fractional content of PFZ water north of the SAF increases by approximately 0.1 for every 15° of longitude. Retaining potential vorticity as a parameter in the OMP analysis does not substantially alter the results. A simple bulk calculation reveals that this magnitude of cross-frontal exchange could cause the downstream evolution of SAMW mixed layer properties observed by Argo; the mixed layers in the simple bulk calculation mirror the along-front freshening and cooling of the SAMW mixed layers observed by Argo. This result is consistent with chapter 3, which found that air-sea fluxes were necessary for forming the deep SAMW mixed layers, but did little to change their properties.

References

Abernathey, R., Marshall, J., Mazloff, M., and Shuckburgh, E., 2010: Enhancement of Mesoscale Eddy Stirring at Steering Levels in the Southern Ocean. *Journal of Physical Oceanography*, **40**, 170–+. doi:10.1175/2009JPO4201.1.

Albérola, C., Millot, C., Send, U., Mertens, C., and Fuda, J.-L., 1996: Comparison of XCTD/CTD data. *Deep-Sea Research I*, **43**, 859–876.

Ansorge, I. J., Lutjeharms, J. R. E., Swart, N. C., and Durgadoo, J. V., 2006: Observational evidence for a cross frontal heat pump in the Southern Ocean. *Geophysical Research Letters*, **33**, 19601–+. doi:10.1029/2006GL026174.

Antonov, J. A., Locarnini, R. A., Boyer, T. P., Garcia, H. E., and Mishonov, A., 2006: World Ocean Atlas 2005, Vol. 2: Salinity. In *NOAA Atlas NESDIS 62*, editor S. Levitus. U.S. Government Printing Office, Washington, D.C. Climatology obtained at: http://www.nodc.noaa.gov/OC5/WOA05/woa05data.html.

Banks, H. T., Wood, R. A., Gregory, J. M., Johns, T. C., and Jones, G. S., 2000: Are observed decadal changes in Intermediate Water masses a signature of anthropogenic climate change? *Geophys. Res. Lett.*, **27**, 2961–2964. doi:10.1029/2000GL011601.

Beal, L. M., Chereskin, T. K., Lenn, Y. D., and Elipot, S., 2006: The Sources and Mixing Characteristics of the Agulhas Current. *Journal of Physical Oceanography*, **36**, 2060–+. doi:10.1175/JPO2964.1.

Bower, A. S., Rossby, H. T., and Lillibridge, J. L., 1985: The Gulf Stream – Barrier or Blender? *Journal of Physical Oceanography*, **15**, 24–32.

Brainerd, K. E., and Gregg, M. C., 1995: Surface mixed and mixing layer depths. *Deep-sea Research Part I-oceanographic Research Papers*, **42**, 1521–1543.

Bryden, H. L., McDonagh, E. L., and King, B. A., 2003: Changes in Ocean Water Mass Properties: Oscillations or Trends? *Science*, **300**, 2086–2089. doi:10.1126/science.1083980.

Budillon, G., Pacciaroni, M., Cozzi, S., Rivaro, P., Catalano, G., Ianni, C., and Cantoni, C., 2003: An optimum multiparameter mixing analysis of the shelf waters in the Ross Sea. *Antarctic Science*, **15**, 105–118.

Chen, D., Busalacchi, A. J., and Rothstein, L. M., 1994: The roles of vertical mixing, solar-radiation, and wind stress in a model simulation of the sea-surface temperature seasonal cycle in the tropical Pacific Ocean. *J. Geophysical Research-oceans*, **99**, 20345–20359.

Chereskin, T. K., and Roemmich, D., 1991: A comparison of measured and wind-derived Ekman transport at 11 ° N in the Atlantic Ocean. *J. Phys. Oceanography*, **21**, 869–878.

Chereskin, T. K., Talley, L. D., and Sloyan, B. M., 2010: Nonlinear vorticity balance of the Subantarctic Front in the southeast Pacific. *Journal of Geophysical Research (Oceans)*, **115**, 6026–+. doi:10.1029/2009JC005611.

Chu, P., Wang, Q., and Bourke, R., 1999: A Geometric Model for the Beaufort/Chukchi Sea Thermohaline Structure. *Journal of Atmospheric and Oceanic Technology*, **16**, 613–632.

de Boyer Montégut, C., Madec, G., Fischer, A. S., Lazar, A., and Iudicone, D., 2004: Mixed layer depth over the global ocean: An examination of profile data and a profile-based climatology. *J. Geophysical Research-oceans*, **109**. Climatology obtained at http://www.lodyc.jussieu.fr/ cdblod/mld.html.

Deacon, G. E. R., 1937: The Hydrology of the Southern Ocean. *Discovery Rep.*, **XV**, 1–124.

Dong, S., Sprintall, J., Gille, S. T., and Talley, L., 2008: Southern Ocean mixed-layer depth from Argo float profiles. *Journal of Geophysical Research (Oceans)*, **113**, 6013–+. doi:10.1029/2006JC004051.

England, M. H., Godfrey, J. S., Hirst, A. C., and Tomczak, M., 1993: The mechanism for Antarctic Intermediate Water renewal in a world ocean model. *J. Phys. Oceanography*, **23**, 1553–1560.

Fairall, C. W., Bradley, E. F., Hare, J. E., Grachev, A. A., and Edson, J. B., 2003: Bulk parameterization of air-sea fluxes: Updates and verification for the COARE algorithm. *J. Climate*, **16**, 571–591.

Frants, M., Gille, S., Hewes, C., Holm-Hansen, O., Kahru, M., Lombrozo, A., Measures, C., Mitchell, B. G., Wang, H., and Zhou, M., 2008: Optimal Multiparameter Analysis of Source Water Distributions in the Southern Drake Passage. Submitted to *Journal of Geophysical Research*.

Gille, S. T., 2002: Warming of the Southern Ocean Since the 1950s. *Science*, **295**, 1275–1278.

Hanawa, K., and Talley, L. D., 2001: Mode waters. In *Ocean Circulation and Climate*, editors G. Siedler, J. Church, and J. Gould, 373–386. Academic Press.

Hartin, C., Fine, R., Sloyan, B., Talley, L., and Happell, J., 2010: Formation Rates of Subantarctic Mode Water and Antarctic Intermediate Water in the Southeast Pacific. In preparation.

Herraiz-Borreguero, L., and Rintoul, S. R., 2010: Subantarctic Mode Water variability influenced by mesoscale eddies south of Tasmania. *Journal of Geophysical Research (Oceans)*, **115**, 4004–+. doi:10.1029/2008JC005146.

Hinrichsen, H., and Tomczak, M., 1993: Optimum multiparameter analysis of the water mass structure in the western North Atlantic ocean. *Journal of Geophysical Research*, **98**, 10155–10170. doi:10.1029/93JC00180.

Holte, J., and Talley, L., 2009: A New Algorithm for Finding Mixed Layer Depths with Applications to Argo Data and Subantarctic Mode Water Formation*. *Journal of Atmospheric and Oceanic Technology*, **26**, 1920–+. doi:10.1175/2009JTECHO543.1.

Holte, J., Talley, L. D., Chereskin, T. K., and Sloyan, B. M., 2010: The role of air-sea fluxes in Subantarctic Mode Water formation. In preparation.

Ito, T., Woloszyn, M., and Mazloff, M., 2010: Anthropogenic carbon dioxide transport in the Southern Ocean driven by Ekman flow. *Nature*, **463**, 80–83. doi:10.1038/nature08687.

Jayne, S. R., and Marotzke, J., 2002: The Oceanic Eddy Heat Transport. *Journal of Physical Oceanography*, **32**, 3328–3345. doi:10.1175/1520-0485(2002)032¡3328:TOEHT¿2.0.CO;2.

Joyce, T. M., 1977: A Note on the Lateral Mixing of Water Masses. *J. Phys. Oceanography*, **7**, 626–629.

Joyce, T. M., Thomas, L. N., and Bahr, F., 2009: Wintertime observations of Subtropical Mode Water formation within the Gulf Stream. *Geophys. Res. Lett.*, **36**, 2607–+. doi:10.1029/2008GL035918.

Kalnay, E., Kanamitsu, M., Kistler, R., Collins, W., Deaven, D., Gandin, L., Iredell, M., Saha, S., White, G., Woollen, J., Zhu, Y., Leetmaa, A., Reynolds, B., Chelliah, M., Ebisuzaki, W., Higgins, W., Janowiak, J., Mo, K. C., Ropelewski, C., Wang, J., Jenne, R., and Joseph, D., 1996: The NCEP/NCAR 40-Year Reanalysis Project. *Bulletin of the American Meteorological Society*, **77**, 437–472.

Kantha, L., and Clayson, C., 1994: Numerical Models of Oceans and Oceanic Processes. In *International Geophysics Series*, volume 66, 940 pp. Academic Press, San Diego.

Kara, A. B., Rochford, P. A., and Hurlburt, H. E., 2000: An optimal definition for ocean mixed layer depth. *J. Geophysical Research-oceans*, **105**, 16803–16821.

Kara, A. B., Rochford, P. A., and Hurlburt, H. E., 2003: Mixed layer depth variability over the global ocean. *J. Geophysical Research-oceans*, **108**. Climatology obtained at http://www7320.nrlssc.navy.mil/nmld/nmld.html+.

Karsten, R., and Marshall, J., 2002: Constructing The Residual Circulation of The Acc From Observations. *J. Phys. Oceanography*, **32**, 3315–3327.

Keeling, R. F., and Stephens, B. B., 2001: Antarctic sea ice and the control of Pleistocene climate instability. *Paleoceanography*, **16**, 112–131. doi:10.1029/2000PA000529.

Kelly, K. A., Dickinson, S., and Yu, Z., 1999: NSCAT tropical wind stress maps: Implications for improving ocean modeling. *J. Geophys. Res.*, **104**, 11291–11310. doi: 10.1029/1998JC900036.

Klein, B., and Tomczak, M., 1994: Identification of diapycnal mixing through optimum multiparameter analysis. 2. Evidence for unidirectional diapycnal mixing in the front between North and South Atlantic Central Water. *Journal of Geophysical Research*, **99**, 25275–25280. doi:10.1029/94JC01948.

Large, W. G., McWilliams, J. C., and Doney, S. C., 1994: Oceanic vertical mixing: a review and a model with a nonlocal boundary layer parameterization. *Reviews of Geophysics*, **32**, 363–404. doi:10.1029/94RG01872.

Lavender, K. L., Davis, R. E., and Owens, W. B., 2002: Observations of open-ocean deep convection in the Labrador Sea from subsurface floats. *J. Phys. Oceanography*, **32**, 511–526.

Leffanue, H., and Tomczak, M., 2004: Using OMP analysis to observe temporal variability in water mass distribution. *Journal of Marine Systems*, **48**, 3–14. doi: 10.1016/j.jmarsys.2003.07.004.

Levitus, S., and Boyer, T., 1994: World Ocean Atlas 1994 Volume 3: Salinity. In *NOAA Atlas NESDIS 3*. U.S. Department of Commerce, Washington, D.C. Climatology obtained at http://ingrid.ldgo.columbia.edu/SOURCES/.LEVITUS94/.MONTHLY/.Zmix/.

Lorbacher, K., Dommenget, D., Niiler, P., and Köhl, A., 2006: Ocean mixed layer depth: A subsurface proxy of ocean-atmosphere variability. *Journal of Geophysical Research (Oceans)*, **111**, 7010–+. doi:10.129/2003JC002157.

Lukas, R., and Lindstrom, E., 1991: The mixed layer of the western equatorial Pacific Ocean. *J. Geophys. Res.*, **96**, 3343–3358.

Marshall, J., and Schott, F., 1999: Open-ocean convection: Observations, theory, and models. *Reviews of Geophysics*, **37**, 1–64. doi:10.1029/98RG02739.

Marshall, J., Shuckburgh, E., Jones, H., and Hill, C., 2006: Estimates and Implications of Surface Eddy Diffusivity in the Southern Ocean Derived from Tracer Transport. *Journal of Physical Oceanography*, **36**, 1806–+. doi:10.1175/JPO2949.1.

Mazloff, M., Heimbach, P., and Wunsch, C., 2009: An eddy-permitting Southern Ocean state estimate. Submitted to *Journal of Oceanography*.

McCartney, M. S., 1977: Subantarctic mode water. In *A Voyage of Discovery: George Deacon 70th Anniversary Volume*, editor M. V. Angel, 103–119. Pergamon.

McCartney, M. S., 1982: The subtropical recirculation of mode waters. *J. Mar. Res.*, **24**, 427–464.

Mellor, G. L., and Yamada, T., 1982: Development of a turbulence closure model for geophysical fluid problems. *Reviews of Geophysics and Space Physics*, **20**, 851–875. doi:10.1029/RG020i004p00851.

Monterey, G., and Levitus, S., 1997: Seasonal Variability of Mixed Layer Depth for the World Ocean. Technical Report NOAA Atlas NESDIS 14, Natl. Oceanic and Atmos. Admin., Silver Spring, MD.

Morrow, R., Donguy, J., Chaigneau, A., and Rintoul, S., 2004: Cold-core anomalies at the subantarctic front, south of Tasmania. *Deep Sea Research Part I: Oceanographic Research*, **51**, 1417–1440. doi:10.1016/S0967-0637(04)00142-6.

Naveira Garabato, A. C., Jullion, L., Stevens, D. P., Heywood, K. J., and King, B. A., 2009: Variability of subantarctic mode water and antarctic intermediate water in the drake passage during the late-twentieth and early-twenty-first centuries. *Journal of Climate*, **22**(13), 3661–3688.

Noh, Y., Jang, C. J., Yamagata, T., Chu, P. C., and Kim, C. H., 2002: Simulation of more realistic upper-ocean processes from an OGCM with a new ocean mixed layer model. *J. Phys. Oceanography*, **32**, 1284–1307.

Ohlmann, J. C., Siegel, D. A., and Gautier, C., 1996: Ocean mixed layer radiant heating and solar penetration: A global analysis. *J. Climate*, **9**, 2265–2280.

Oka, E., Talley, L. D., and Suga, T., 2006: Temporal variability of winter mixed layer in the mid- to high-latitude North Pacific. Submitted to *Journal of Oceanography*.

Orsi, A. H., Whitworth, T., and Nowlin, W. D., 1995: On the meridional extent and fronts of the Antarctic Circumpolar Current. *Deep-sea Research Part I-oceanographic Research Papers*, **42**, 641–673.

Owens, W. B., 1984: A Synoptic and Statistical Description of the Gulf Stream and Subtropical Gyre Using SOFAR Floats. *Journal of Physical Oceanography*, **14**, 104–113. doi:10.1175/1520-0485(1984)014¡0104:ASASDO¿2.0.CO;2.

Pahnke, K., and Zahn, R., 2005: Millennial-Scale Antarctic Intermediate Water Variability over the past 340,000 Years as Recorded by Benthic Foraminiferal δ13C in the Mid-Depth Southwest Pacific. *AGU Spring Meeting Abstracts*, A4+.

Park, Y., and Gambéroni, L., 1997: Cross-frontal exchange of Antarctic Intermediate Water and Antarctic Bottom Water in the Crozet Basin. *Deep Sea Research Part II: Topical Studies in Oceanography*, **44**, 963–986. doi:10.1016/S0967-0645(97)00004-0.

Poole, R., and Tomczak, M., 1999: Optimum multiparameter analysis of the water mass structure in the Atlantic Ocean thermocline. *Deep Sea Research I*, **46**, 1895–1921.

Price, J. F., Weller, R. A., and Pinkel, R., 1986: Diurnal cycling: Observations and models of the upper ocean response to diurnal heating, cooling, and wind mixing. *J. Geophys. Res.*, **91**, 8411–8427.

Redfield, A., Ketchum, B. H., and Richards, F. A., 1963: The influence of organisms on the composition of sea-water. In *The Sea: Ideas and Observations on Progress in the Study of the Seas*, editor M. N. Hill, 26–77. Springer-Verlag Berlin Heidelberg, London.

Rintoul, S., and England, M., 2002a: Ekman Transport Dominates Local Air-Sea Fluxes in Driving Variability of Subantarctic Mode Water. *J. Phys. Oceanography*, **32**, 1380–1321.

Rintoul, S., and England, M., 2002b: Ekman Transport Dominates Local Air-Sea Fluxes in Driving Variability of Subantarctic Mode Water. *J. Phys. Oceanography*, **32**, 1380–1321.

Roemmich, D., Freeland., H., Kim, K., King, B., Molinari, R., Owens, W. B., Riser, S., Send, U., and Troan, P. Y. L., 2001: Argo: the global array of profiling floats. In *Observing the Oceans in the 21st Century*, editors K. J. Koblinksy, and N. R. Smith, 604. GODAE Project Office and Bureau of Meteorology, Melbourne.

Ruddick, B., 2003: Oceanic thermohaline intrusions: observations. *Progress in Oceanography*, **56**, 499–527. doi:10.1016/S0079-6611(03)00028-4.

Sabine, C. L., Feely, R. A., Key, R. M., Bullister, J. L., Millero, F. J., Lee, K., Peng, T. H., Tilbrook, B., Ono, T., and Wong, C. S., 2002: Distribution of anthropogenic CO2 in the Pacific ocean. *Global Biogeochemical Cycles*, **16**.

Sallée, J.-B., Morrow, R., and Speer, K., 2008: Eddy heat diffusion and Subantarctic Mode Water formation. *Geophys. Res. Lett.*, **35**, 5607–+. doi:10.1029/2007GL032827.

Sallée, J.-B., Speer, K., Rintoul, S., and Wijffels, S., 2010: Southern Ocean Thermocline Ventilation. *Journal of Physical Oceanography*, **40**, 509–+. doi:10.1175/2009JPO4291.1.

Sallée, J.-B., Wienders, N., Speer, K., and Morrow, R., 2006: Formation of subantarctic mode water in the southeastern Indian Ocean. *Ocean Dynamics*, **56**, 525–542. doi:10.1007/s10236-005-0054-x.

Sathiyamoorthy, S., and Moore, G. W. K., 2002: Buoyancy Flux at Ocean Station Bravo. *J. Phys. Oceanography*, **32**, 458–474.

Shuckburgh, E., Jones, H., Marshall, J., and Hill, C., 2009: Understanding the Regional Variability of Eddy Diffusivity in the Pacific Sector of the Southern Ocean. *Journal of Physical Oceanography*, **39**, 2011–+. doi:10.1175/2009JPO4115.1.

Sloyan, B. M., and Rintoul, S., 2001: Circulation, Renewal, and Modification of Antarctic Mode and Intermediate Water. *J. Phys. Oceanography*, **31**, 1005–1030.

Sloyan, B. M., Talley, L. D., Chereskin, T. K., Fine, R., and Holte, J., 2010: Antarctic Intermediate Water and Subantarctic Mode Water Formation in the southeast Pacific: the role of turbulent mixing. *Journal of Physical Oceanography*, **40**, 1558–1574.

Speer, K., Rintoul, S., and Sloyan, B. M., 2000: The Diabatic Deacon Cell. *J. Phys. Oceanography*, **30**, 3212–3222.

Sprintall, J., and Roemmich, D., 1999: Characterizing the structure of the surface layer in the Pacific ocean. *J. Geophysical Research-oceans*, **104**, 23297–23311.

Sprintall, J., and Tomczak, M., 1992: Evidence of the Barrier Layer in the Surface Layer of the Tropics. *J. Geophys. Res.*, **97**, 7305–7316.

Talley, L. D., 1996: Antarctic Intermediate Water in the South Atlantic. In *The South Atlantic: Present and Past Circulation*, editors G. Wefer, W. Berger, G. Siedler, and D. Webb, 219–238. Springer-Verlag Berlin Heidelberg, Germany.

Talley, L. D., 1999: Some aspects of ocean heat transport by the shallow, intermediate and deep overturning circulations. In *Mechanisms of Global Climate Change at Millennial Time Scales*, volume 112 of *Geophys. Monogr.*, 1–22. Amer. Geophys. Union.

Thomson, R. E., and Fine, I. V., 2003: Estimating mixed layer depth from oceanic profile data. *J. Atmospheric Oceanic Technology*, **20**, 319–329.

Tomczak, M., and Large, D. G. B., 1989: Optimum multiparameter analysis of mixing in the thermocline of the Eastern Indian Ocean. *J. Geophys. Res.*, **94**, 16141–16149. doi:10.1029/JC094iC11p16141.

Tsuchiya, M., and Talley, L. D., 1998: A Pacific hydrographic section at 88°W: Water-property distribution. *J. Geophys. Res.*, **103**, 12899–12918. doi:10.1029/97JC03415.

Wang, X., and Matear, R. J., 2001: Modeling the upper ocean dynamics in the Subantarctic and Polar Frontal Zones in the Australian sector of the Southern Ocean. *J. Geophys. Res.*, **106**, 31511–31524. doi:10.1029/2000JC000357.

Wong, A. P. S., Bindoff, N. L., and Church, J. A., 2001: Freshwater and Heat Changes in the North and South Pacific Oceans between the 1960s and 1985-94. *Journal of Climate*, **14**, 1613–1633. doi:10.1175/1520-0442(2001)014¡1613:FAHCIT¿2.0.CO;2.

Yu, L., Jin, X., and Weller, R. A., 2008: Multidecade Global Flux Datasets from the Objectively Analyzed Air-sea Fluxes (OAFlux) Project: Latent and sensible heat fluxes, ocean evaporation, and related surface meteorological variables. Technical Report OAFlux Project Technical Report, Woods Hole Oceanographic Institution, Woods Hole. Massachusetts.

Yuter, S. E., and Parker, W. S., 2001: Rainfall Measurement on Ship Revisited: The 1997 PACS TEPPS Cruise. *Journal of Applied Meteorology*, **40**, 1003–1018.